University of Texas at Arlington

MavMatrix

2023

High Magnification Surface Topography based Digital Image Correlation (DIC) for Identifying Damage Accumulation and Crack Growth in Polycrystalline Nickel

Arash Valiollahi

Follow this and additional works at: https://mavmatrix.uta.edu/mechaerospace_dissertations

Part of the Aerospace Engineering Commons, and the Mechanical Engineering Commons

High Magnification Surface Topography based Digital Image Correlation (DIC) for Identifying Damage Accumulation and Crack Growth in Polycrystalline Nickel

By

Arash Valiollahi

Presented to the Faculty of the Graduate School of
The University of Texas at Arlington in Partial Fulfillment
of the Requirements for the Degree of

DOCTOR OF PHILOSOPHY

THE UNIVERSITY OF TEXAS AT ARLINGTON

August 2023

Acknowledgement

I would like to express my heartfelt gratitude to the incredible individuals who have supported me wholeheartedly throughout my doctoral program.

First and foremost, I am deeply thankful to my advisor, Prof. Haiying Huang. Her unwavering support, continuous guidance, and invaluable mentorship have been instrumental in shaping my research and helping me navigate the challenges of my academic journey.

I am immensely grateful to my best friend and beloved wife, Farzaneh, for her unwavering support and presence during the ups and downs of this journey and being my biggest source of strength during overwhelming times.

I would like to thank my dear friend, Dr. Jalal Fathi Sola for his invaluable insights and shared experiences from his own PhD work in the same field and for being such a great friend in life.

I would like to extend my appreciation to the committee members, Dr. Ashfaq Adnan, Dr. Bo P Wang, Dr. Robert Taylor, and Dr. Narges Shayesteh. Their valuable feedback, suggestions, and insights have significantly contributed to improving the quality of this research.

Lastly, I would like to express my gratitude to the University of Texas at Arlington for providing me with the opportunity to pursue my PhD.

Abstract

High Magnification Surface Topography based Digital Image Correlation (DIC) for Identifying Damage Accumulation and Crack Growth in Polycrystalline Nickel

Arash Valiollahi

The University of Texas at Arlington, 2023

Supervising Professor: Haiying Huang

Damage index parameters that have been formulated to identify damage localization in plastically deformed materials typically require all six stress or strain components. Recently, simulations through Crystal Plasticity Finite Element Method (CPFEM) have been widely used to extract damage initiation parameters. However, these models are rarely verified due to the challenges in measuring the out-of-plane deformation/strain experimentally. A damage index combining the effective plastic strain and surface roughness change is investigated for identifying damage accumulation sites and predicting crack propagation path in polycrystalline pure Nickel. A novel Digital Image Correlation (DIC) technique is developed to measure both in-plane and out-of-plane deformation from surface topography images acquired using optical interferometry. A simple technique that creates random, micro size reflective speckles for sub-grain strain calculation is demonstrated. Damage accumulation sites detected by the effective strain, surface roughness change, and the combined damage index are assessed in terms of damage localization and localization consistency. The combined damage index provides an enhanced damage localization and localization consistency compared to effective plastic strain or surface roughness damage index alone. The detected damage accumulation sites were correlated with grain orientations that favor "sunken" out-of-plane deformations and large misorientations among neighboring grains.

The proposed combined damage index is then used to predict the future propagation path of microstructurally small crack (MSC) in a fatigue sample. Effective plastic strain, surface roughness and combined damage index maps were constructed during the crack arresting period. The crack future propagation path was then predicted by two approaches based on 'highest intensity' and 'confidence threshold'. The predicted path by the three damage indices was compared to the actual crack path. The combined damage index provided a more accurate, consistent, and confident prediction of sharp turns in crack tortuous path. Finally, A 2D Finite Element Model (FEM) is generated to verify the strain calculation approach based on theoretical strain-displacement equations. The verified strain-displacement equation can be later used to calculate the out-of-plane strain components based on surface height difference. However, the small height difference in a highly polished sample leads to large errors in out-of-plane strain calculation. Thus, a threshold value for minimum height difference between two points should be defined for error reduction in out-of-plane shear strain calculation. At the end of this study, a methodology for estimating this threshold value through FE analysis is suggested for future studies.

Table of Contents

Table of Figures

Chapter 1. Introduction

Fatigue is the primary mode of failure for numerous engineering structures. Over the course of history, there have been many instances of catastrophic fractures in man-made machines and structures, resulting in significant loss of life. To account for uncertainties, safety factors are incorporated into the design of structures. However, the growing demand for smaller, lighter structures and increased service life necessitates optimization of the design process. This requires a deeper understanding of crack formation and growth behavior to enhance the accuracy of predicted fatigue life. Fatigue life can be divided into three stages: crack incubation or nucleation, where cyclic hardening or softening occurs; crack initiation, characterized by the formation of small measurable cracks; and crack propagation. By the time a measurable crack appears, a significant portion of the fatigue life has already been consumed [1–3]. The process of damage initiation is closely tied to plastic deformation, which also influences early crack propagation. A better understanding of damage initiation and early growth can lead to improved predictions of fatigue life, early detection and prevention of cracks, and enhanced safety in mechanical and aerospace structures. However, identifying the exact location and timing of damage initiation remains a significant challenge. Damage initiation in polycrystalline metals is strongly influenced by local microstructural factors, including grain orientation, neighboring grain characteristics, the presence of defects or particles, and grain size [4–8]. Despite extensive studies conducted over the past century, accurately predicting damage initiation locations and timing remains unconclusive. Additionally, the behavior of small cracks, which are influenced by microstructure and do not adhere to conventional laws such as the Paris law, is notoriously difficult to predict. Consequently,

it is crucial to define a fatigue damage parameter capable of reliably predicting crack behavior prior to initiation and during the early growth stage.

1.1 Mechanism of damage formation and Fatigue Indicator Parameters (FIPs)

When metals undergo cyclic loading and reach the critical resolved shear stress on a slip system, dislocations move along the slip direction, resulting in the formation of slip steps. However, during reverse loading, the slip does not fully recover, leading to cyclic slip irreversibility [9, 10]. This process continues with additional cyclic loading, causing surface roughening and strain localization, eventually giving rise to persistent slip bands (PSBs). The formation of PSBs and strain localization serve as precursors to crack initiation. Once a crack is initiated, its propagation is influenced by microstructural features during stage I crack propagation, leading to multiple arrests and releases in the crack path and oscillation in crack growth rate. As the crack length and Stress Intensity Factor (SIF) increase, the crack becomes less dependent on microstructure and grows perpendicular to the loading direction in a zigzag-shaped path during stage II crack propagation. To predict damage initiation in cyclically loaded polycrystalline materials, fatigue indicator parameters (FIPs) such as cyclic slip irreversibility [10], critical accumulated slip [11], resolved shear stress [12–14], maximum cyclic plastic shear strain [15–18], energy dissipation during crystallographic slip [6, 19–23] and effective plastic strain have been proposed. Previous studies defined a critical irreversibility value as a necessary condition for crack initiation, but it was found to be insufficient. Alternatively, some researchers attempted to predict crack initiation time based on the accumulated energy in the slip bands. Others have investigated effective plastic strain and cyclic shear strain to study the formation and propagation of microcracks. Nonetheless, an accurate evaluation of these FIPs requires all six stress/strain components. However, the out-of-plane shear strain components are difficult to measure experimentally. As such, Computational

approaches based on the Crystal Plasticity Finite Element Method (CPFEM) have been used to study the driving mechanism of crack propagation [24–27]. However, due to simplifications, assumptions, lack of knowledge of the microstructure underneath the surface, and insufficient computation capacity, they are rarely verified experimentally and therefore inaccurate in practice.

1.2 Effect of Microstructure

Recent advancements in characterization tools have enabled extensive investigations into materials subjected to cyclic loading, revealing insights into crack initiation, early crack growth, and the influence of microstructural factors. Studies utilizing SEM and Electron Backscatter Diffraction (EBSD) on polycrystalline FCC metals have demonstrated the significant role of grain orientation and grain boundary configuration in crack initiation and short crack growth [28–31]. When neighboring grains exhibit low misorientation, slip bands can migrate between them without significant dislocation pile-up at the grain boundary, allowing cracks to initiate and propagate along these slip bands [22, 32–34]. Conversely, higher misorientation between adjacent grains presents a stronger barrier to crack growth, with observed deceleration and acceleration near the grain boundary [31]. 3D X-ray tomography has provided detailed information about the microstructure's impact on crack paths at the surface and in the bulk material [35–39]. Additionally, Digital Image Correlation (DIC) has revealed strain heterogeneity across grains due to misorientation, shedding light on crack initiation and growth mechanisms [40–43]. Although 2D DIC studies have offered valuable insights into strain heterogeneity, they are limited in providing quantitative information about surface height changes, which are important indicators of shear and plastic deformation.

1.3 Surface Morphology

Cyclic slip irreversibility is widely recognized as a critical factor for crack initiation, particularly on the surface. Studies have demonstrated that surface and bulk cyclic slip irreversibility manifest as fatigue damage on the surface [10]. Consequently, investigating irreversibility on the surface is essential for studying damage initiation and early crack growth. Surface profiling techniques have been developed to provide quantitative measurements of surface topography, unlike SEM and 2D DIC methods. Atomic Force Microscopy (AFM) has shown that measuring extrusion height allows for the quantification of strain irreversibility [44–46]. However, AFM studies are limited to small areas and within grains, overlooking intergranular crack initiations. Recently, optical measurement techniques such as Scanning White Light Interferometry (SWLI), scanning laser confocal microscopy (SLCM), and two-step phase-shifting interferometry have gained popularity due to their simplicity and high temporal and spatial resolution. Unlike AFM, these non-contact optical techniques utilize light interference to measure surface topography across a wide height range, enabling the measurement of out-of-plane movement. Studies employing these techniques have revealed that the largest surface displacements occur at triple points and grain boundaries, with grain movement playing a dominant role in surface roughness [47, 48]. Using two-step phase-shifting interferometry, the fatigue process zone (FPZ) can be calculated from surface topography measurements [49]. Surface texture analysis has been established as a reliable method for determining crack initiation time, with studies exploring fractal dimensions and suggesting their potential as an early warning indicator for impending damage [38, 39, 40]. Optical profiling has also been utilized to quantify surface roughness parameters, with observations of abrupt changes at specific cycles that correlate with crack initiation time. SWLI studies have demonstrated the effectiveness of surface profile analysis in analyzing crack initiation behavior [52]. However, some

4

studies lacked temporal resolution [51, 52] or were not verified with SEM observations [50, 51]. Overall, investigations into surface topography changes during cyclic loading have shown that surface topography analysis can effectively quantify plastic deformation and strain irreversibility. Recently, using high resolution SWLI technique, a full-filed surface roughness damage index was proposed to identify crack initiation site and predicting crack propagation path [53, 54]. However, these studied were merely focused on out-of-plane deformation, i.e., surface roughness change, without considering in-plane strain.

1.4 Strain

Surface topography change induced by plastic deformation and formation of slip bands causes stress concentration and strain accumulation which facilitates crack initiation. As such, numerous experimental works on driving mechanisms of MSC nucleation and growth in ductile fatigue have been focusing on plastic deformation and strain localization [11, 34, 53–55]. Recent research has extensively investigated the accumulation and localization of strain at the grain scale using a technique called High Resolution Digital Image Correlation (HR-DIC) [5, 41, 62, 63, 42, 43, 56–61]. HR-DIC has been widely employed in numerous studies to examine the distribution of strain within grains and its relationship with the microstructure. However, due to the limited spatial resolution of optical microscopes, which is restricted to half the wavelength of the illumination light, these studies primarily focused on relatively large grain sizes. To achieve sub-grain strain resolution for smaller grains, researchers have utilized a DIC technique based on Scanning Electron Microscopy (SEM) [16, 64–71]. By employing these Optical microscope or SEM based DIC techniques, scientists were able to investigate various correlations, including fatigue crack initiation and growth with strain localization [72–74], Schmid factor [70, 75], grain orientation [65, 71, 76], slip transfer [16, 42, 66, 77], and the presence of voids [78]. However, some of these

correlations were merely qualitative, suggesting potential sites for fatigue damage development [36, 66, 79], while others offered quantitative evaluations only after crack initiation or propagation [22, 69, 80, 81]. Moreover, the temporal resolution of these analyses was relatively low, with large intervals between data collection and processing, compared to the fatigue life of the material. Importantly, these studies were limited to 2D measurements, only capturing in-plane strains and neglecting out-of-plane plastic deformation. To overcome these limitations, researchers have employed 3D volumetric DIC and stereovision DIC, which enable measurement of both in-plane and out-of-plane deformations on the sample surface [5, 57, 68, 82, 83]. These methods involve the synchronization and calibration of two cameras at a specific angle relative to the specimen surface. Stereovision DIC has been successfully utilized to study strain heterogeneity and accumulation at the grain level under monotonic and cyclic loading conditions. However, for high-magnification measurements with a very narrow field of view, the camera lenses need to be positioned extremely close to the sample surface, determined by the focal plane. In many cases, placing two lenses in such close proximity may not be practical, thereby limiting the use of high-magnification lenses. Consequently, sub-grain studies using stereovision DIC have focused on large single or oligo crystals to examine strain variations within grains using low-magnification lenses. Additionally, these techniques might not provide adequate vertical resolution to capture changes in surface roughness induced by plasticity, which can be on the order of tens of nanometers [53, 54].

To the best of our knowledge, there is no study that investigates both in-plane and out-of-plane deformation with sub-grain resolution for identifying damage initiation and predicting crack initiation in polycrystalline ductile material with small grains. Here we propose a novel surface

topography based DIC technique to study the damage initiation and predicting crack propagation path in Pure Nickel.

Chapter 2. Combining effective plastic strain and surface roughness change for identifying damage accumulation sites in a tensile sample

2.1 Introduction

Damage initiation in ductile materials is associated with accumulation and migration of dislocations [84], resulting in surface topography changes [85, 86] and the formation of plastic intrusions and extrusions known as slip bands [87–89]. Consequently, these out-of-plane features cause stress concentrations that lead to crack initiation [9, 90, 91]. While the progression of material damage from dislocation accumulation/migration, to surface topography changes, to crack initiation has been validated experimentally [92–98], the underlying mechanics for such a damage development process is still unknown at this point [9]. Various parameters have been proposed as the damage index for identifying early material damage development, including the effective plastic strain [24, 27, 99–101], the resolved shear stress [12–14], the stored energy density [19–21] and the energy dissipation during crystallographic slip [6, 23, 102], just to name a few. These parameters require the knowledge of all six stress or strain components, including the out-of-plane stress/strain components that are difficult to measure experimentally. Therefore, past studies relied on simulated stress/strain values obtained from Crystal Plasticity Finite Element Method (CPFEM). However, CPFEM cannot simulate the entire microstructure faithfully, due to limited computation capacity, imperfect constitutive laws, and the lack of knowledge on the crystallographic features underneath the surface. As a result, the simulation models are rarely verified by experiment and thus inaccurate in practice [103]. While X-ray Computer Tomography (XCT) and High Energy Diffraction Microscopy (HEDM) enable true 3D characterization of

material crystallographic structures [104–109], correlating the experiment and simulation remains an unsolved research problem that is under active research [9].

Since the out-of-plane strain components are difficult to measure using conventional non-destructive techniques, damage indices calculated solely from the in-plane strain components, measured using Digital Image Correlation (DIC) techniques, are proposed as an alternative [43, 56]. For conventional DIC analysis, random sized patterns are applied on the sample surface which is imaged before and after deformation using a digital camera. Dividing the digital images into small subsets and using the subsets in the un-deformed image as the reference, a subset in the deformed image whose intensity variation matches closely with the reference subset is identified. This correlation process is accomplished by applying a certain feature detection and optimization algorithm. The local deformation and thus strain can then be calculated from the location of the matching subsets. While DIC using high magnification optical microscopes has been applied to study grain scale strain distribution [5, 41, 43, 56, 60–62, 110], the spatial resolution of the optical method is limited to one half of the wavelength of the illumination light used [111]. To measure strain localization with a high sub-grain resolution, DIC techniques based on Scanning Electron Microscopy (SEM) have been employed. Using this technique, researchers were able to investigate the correlation between crack initiation and Schmid factor [70, 112], grain orientation [65, 71, 76], strain localization [72–74], and presence of voids [78]. Since these optical or SEM DIC studies were carried out in two-dimensions (2D), they can only measure the in-plane deformations. The out-of-plane deformation, which is associated with the surface topography changes, cannot be measured using 2D DIC techniques.

A more sophisticated DIC technique, i.e., the stereovision DIC or three dimensional DIC (3D-DIC), can measure the in-plane and out of plane deformations at the surface. Setting two cameras

in a certain angle and applying a precise calibration, a stereovision DIC enables measuring the out-of-plane deformation and thus all the surface strain components [113]. This technique has been employed to investigate the correlation between the microstructure and strain heterogeneity/accumulation under monotonic and cyclic loading [5, 82, 83, 110]. To achieve a high magnification and sub-grain resolution, however, the camera lenses need to be very close to the specimen. In some cases, accommodating two cameras in an extremely tight space and synchronizing them may not be feasible. The distance limitation between the lens and the sample surface restricts the use of high magnification lenses. As a result, a high-resolution sub-grain strain analysis cannot be attained. In addition, plasticity induced surface roughness changes can be very small, in the orders of tens of nanometers. The stereovision DIC may not have the needed vertical resolution for studying nanometer scale surface roughness changes. To the best knowledge of the authors, detailed studies of surface topography changes of plastically deformed samples with small grains using the stereovision DIC has not been reported.

Both the 2D and 3D DIC need a speckle patten, i.e., a pattern with randomly distributed small-size features (a.k.a. speckles), on the sample for image correlation. The randomness, size, density, and distribution of the speckles can strongly influence the accuracy and resolution of the DIC measurements. Speckle pattern creation using color and dust spraying, chemical etching, rough polishing, grid, or micro stamping have been widely used. However, the speckles produced by these techniques often have large sizes and low density. Thus, these techniques are more suitable for samples with large grain size (>1 mm) [5, 82, 83, 110]. To achieve higher magnifications, Focused Ion Beam (FIB) [114], sputter coating [115], gold remodeling [76, 116], particle deposition using compressed air [41], and Electron Beam Lithography [60] have been used to create speckles. While these techniques successfully create speckles as small as a few hundred

10

nanometers, the fabrication procedures are quite complicated. Many of them need a clean room and thus could be expensive to produce [116, 117]. In addition, some of these techniques might also produce scratches or periodic pattern in some areas [114], which may confuse the DIC algorithm. More importantly, the speckles created using these techniques are typically nonreflective and thus cannot be used for optical interferometry-based DIC. Due to these limitations, implementing DIC techniques for measuring both in-plane and out of plane displacements to study plastic deformations within small grains is challenging. Another challenge of applying DIC for plasticity studies is that conventional DIC measures the deformations based on matching the gray scale variation in subsets between a pair of images As a result, the correlation process is limited by the predefined subset size or subset spacing. Tracking a highly distorted subset, due to large strains, is very difficult [118–121]. Besides, the resolution loss induced by deformation and strain averaging in the subset might miss small strain heterogeneities, which are important for the study of localized plasticity.

In addition to the DIC based techniques, surface topography characterization tools, such as Atomic Forced Microscopy (AFM) and Scanning White Light Interferometry (SWLI), were used to measure the out-of-plane displacement, including extrusion height [45, 122, 123], surface roughness change [50–52], and out-of-plane grain movement [124]. Some of these studies defined a global damage index based on the out-of-plane displacements over large areas using statistical parameters and thus overlooked the microstructural details [50, 52]. Others focused on observing the out-of-plane displacements in selected regions where slip bands have initiated and attempted to decipher the mechanism that drives crack development [45, 122, 123]. For both cases, the damage index is not defined over the entire region of interest and thus they are not suitable for identifying damage localization sites. Recently, Sola et al. [53, 54] proposed a full field surface

11

roughness damage index to predict fatigue crack initiation site and future propagation path of microstructurally small cracks (MSCs). They utilized SWLI surface topography images to calculate the surface roughness change at microstructure level. However, these studies were merely concerned with the out-of-plane displacements without considering the in-plane strain components. To the best of our knowledge, a damage index that considers both the in-plane and out-of-plane deformations has not been reported.

In this chapter, a combined damage index that accounts for both the effective plastic strain and the surface roughness change is proposed. Comparing with the damage index calculated from either the effective plastic strain or the surface roughness change, the combined damage index leads to earlier and more consistent identification of damage localization sites. To calculate the in-plane strain components from the surface topography images, a novel technique that produces minute, random, high density, and reflective speckles is introduced. This reflective speckle pattern enables us to calculate the in-plane strains and out-of-plane deformation by comparing undeformed and deformed SWLI surface topography images. A pointwise DIC algorithm was developed to detect the key points based on the grayscale variation within the entire image instead of a subset. As such, large strains, that are difficult to be measured using subset-based DIC, can be measured accurately.

2.2 Experiment procedure and sample preparation

The equipment used for this study is the same as that described in [53, 54]. Briefly, a BOSE Electroforce mechanical testing machine, integrated with a Bruker NPFLEX SWLI surface profiler, with a maximum load capacity of 3000 N was employed to apply the static tensile load. Surface profiling of the sample surface was carried out using the Vertical Scanning Interferometer (VSI) mode of the SWLI surface profiler having a sub-nanometer vertical resolution. A 50X

magnification lens with a 0.55X zoom was used, resulting in a resolution of 0.366 μm in the lateral direction.

A sub-sized nickel tensile specimen with 99.5% purity was designed according to American Society for Testing and Materials (ASTM) E8, Standard Test Methods for Tension Testing of Metallic Materials. The grain size of the selected material was measured to be around 50 μm and the EBSD inspection showed a random grain size and orientation confirming that the material was isotropic. The stress-strain curve obtained from a tensile test on a similar sample is shown in Figure 1(a). The yield stress of the sample was measured to be 211 MPa, indicated by the dark blue bullet point in the inset. Since the mechanical test fixture had a maximum load capacity of 3000 N, the test sample, as shown in Figure 1(b), was designed to have a cross-section of 3 x1.57mm2, resulting in a yield load of 1000 N. Previous tests also revealed that localized surface roughness changes start to emerge at 70% of the yield load. Applying a safe margin, the first load step was set at 50% of the yield load, i.e., at 500 N. The load was increased from 500 N to 900 N with intervals of 100 N. Near the nominal yield load , i.e., from 900 N to 1000 N, the load increment was reduced to 50 N. After the yield point, the loading increment was further decreased to 25 N. After each load increment, the sample was unloaded to acquire the surface topography images. The dash maroon lines shown in the inset of Figure 1(a) mark the stress levels at which the sample was unloaded. After taking the SWLI images, the sample was reloaded to reach to next step of loading. The sample surface was patterned with speckle patterns, as described below.
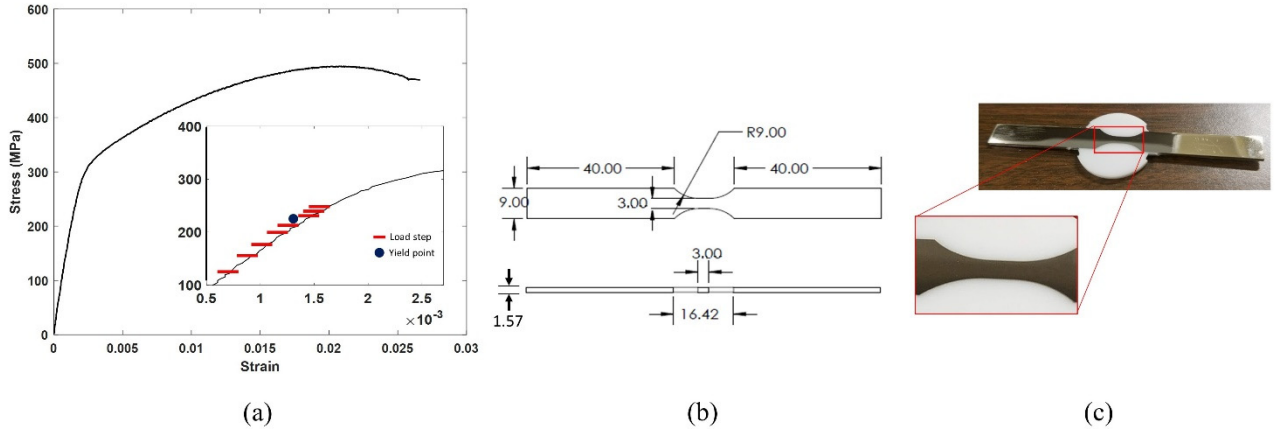
Fig. 1 (a) measured stress-strain curve of the material. the blue dot in the inset marks the yield point while the loading-unloading steps are marked by maroon lines. (b) schematic of the tensile sample and its dimensions and (c) machined sample in a resin mold prepared for polishing.

The back side of the sample was first polished with conventional sandpapers with grit sizes down to P400 in Federation of European Producers of Abrasives (FEPA) standard. To overcome the problem of edge rounding during polishing [53], a mixture was made using Buehler Epokwick Epoxy resin by mixing 15g of resin and 3g of hardener. The sample was placed in a mold and the mixture was poured to cover the cross-section (see **Error! Reference source not found.**(c)). The surface was then manually polished using sandpapers down to a grit size of FPEA P1500 followed by two steps of micro polishing with alumina powder of sizes 1 µm and 0.3 µm, respectively. At the end of micro polishing, the surface roughness at the gage section of the sample was measured to be 16 nm. Next, the sample was released from the resin and its surface was electro-polished. Finally, the sample surface was etched using ASTM E407-25 solution to reveal the grain boundaries.

A 0.5 mm by 0.5 mm area at the center of the gauge section was selected as the region of interest (ROI). Four fiducial marks were created at 0.1 mm distances from the four corners of ROI using Vickers micro indenter to mark the location of ROI on the sample, as shown in Fig. 2(a). The size of the fiducial marks was measured to be around 30 µm. According to ASTM E384, Standard Test

14

Method for Micro-indentation Hardness of Materials, an area roughly 3 times the size of indentation mark might be plastically deformed by the indenter. Thus, the fiducial marks will not introduce any plastic deformations to the ROI. Using a 50X magnification lens with a 0.55X zoom, 63 single SWLI images with a 50% overlap were taken to cover the entire ROI. A 50% overlap was chosen to prevent data loss and ensure the identification of correlation points during image processing, even at high loads. The stitched surface topography image of the ROI, after chemical etching, is shown in Fig. 2(b). Due to etching, the average surface roughness increased from 16 nm to 135 nm. The region that was analyzed in detail in this study is marked by the black box in Fig. 2(b) and its corresponded EBSD map is depicted in Fig. 2(c).

For DIC analysis, the speckle size should be around 3-5 times of the pixel size [125]. Since the pixel size in the current experiment is 0.366 μm, the speckle size should be around 1-2 μm. For this purpose, alumina powder with an average size of 0.3 μm was used to create the speckle. First, 0.5 g of alumina powder was mixed with 5.5 g of water in a stirrer. To improve adhesion of the speckles to the sample surface, 0.5 g of polyvinyl epoxy, a clear adhesive which dissolves in water without leaving any marks on the surface after drying, was added to the solution, and stirred for 30 minutes at 100°C. After applying the mixture to the sample surface using a polishing pad, the sample surface was washed thoroughly to remove excessive mixture particles from the surface and dried in the air. This procedure creates a very thin layer of speckle pattern on the surface, as shown in Fig. 3(a). Two successive enlarged views of the speckled region are shown in Fig. 3(b) and Fig. 3(c). The average speckle size along the lateral direction, measured using an optical microscope, is roughly 1.5 μm with high density and random distribution across the surface that enables the sub-grain strain analysis. Fig. **3**(d) illustrates the height variation along the width of the ROI before and after applying the speckles. The two deep troughs at the right and left correspond to the fiducial

15

marks. The thickness of the speckle layer was determined from the differences of the two surface profiles to an average value of 180 nm.

(a) (b) (c)
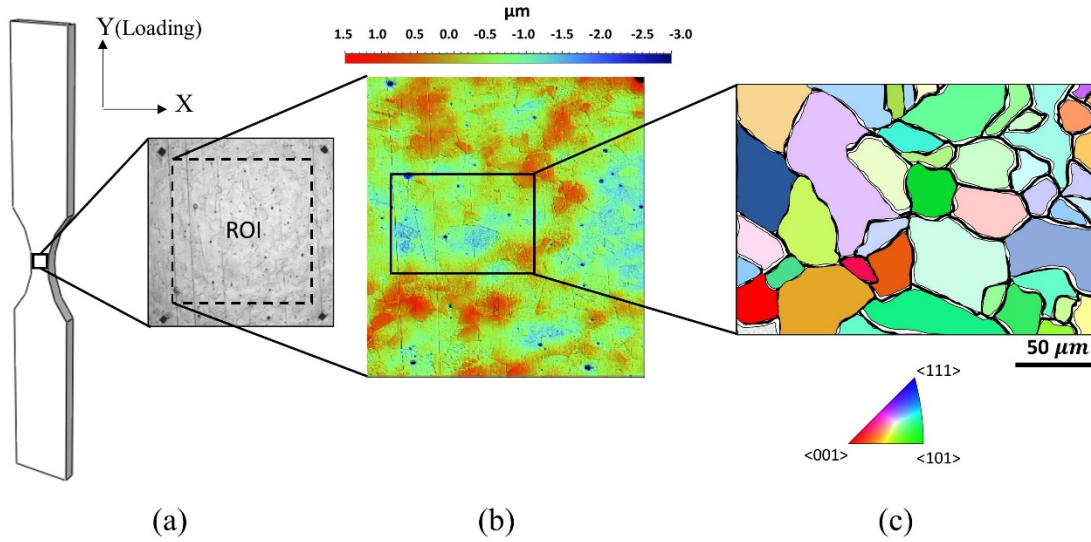
Fig. 2 (a) Region of interest (ROI) and the fiducial marks on the sample gage section, (b) SWLI surface topography image of the entire ROI. The black box marks the region selected by this study. (c) EBSD map showing the grain distribution in a selected region with crystallographic orientation.
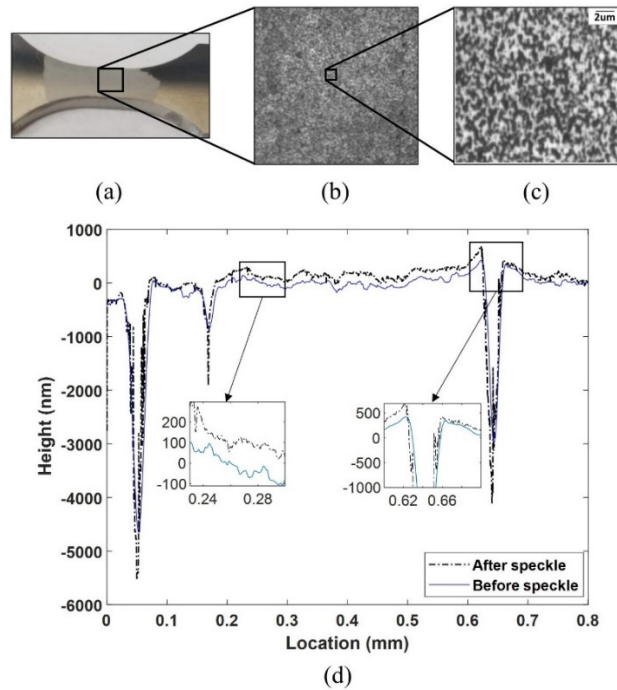
Fig. 3 (a) Speckle layer on the gage section of the sample, (b) magnified view of the ROI with speckle distribution, (c) further magnification to show the size and random distribution of speckles within a small region inside the ROI and, (d) surface height variation along a transverse line connecting two fiducial marks before and after applying the speckle pattern

16

2.3 Image processing

The surface topography images of the tensile sample were processed to extract the 2D strain components using DIC. Stitching errors in the form of vertical and horizontal bands were observed in our previous study [70]. As such, DIC strain calculations were based on single images instead of the stitched image.

First, the acquired surface topography images were compiled to detect and filter the outliers and missing data. Outliers are data points with inaccurate representation of surface height, appearing as singularities having extremely large or small height values compared to their local surface height variation. Missing data are simply a result of no reflection sensed by the optical sensor. The outliers and missing data were replaced with interpolated values based on their immediate surrounding. Although the number of outliers and missing data varies per image per loading step, the average number of filtered points is about 0.85% of the total data population. After removing the outliers and missing data, the surface topography images were converted to grayscale by linearly mapping the surface height values between 0 and 255, where 0 corresponds to the minimum and 255 to the maximum height. The key points of the image, i.e., distinctive features that are invariant in rotation, scale, and distortion to a great degree, were then identified based on gray intensity of their surrounding using various key point descriptors, employing the Speeded Up Robust Features (SURF) and Binary Robust Invariant Scalable Key-points (BRISK) algorithms. These key points correspond to either speckles or inherent surface topography features such as dip, ridge, scratch, gain boundary intersections, etc. The key points that match between the two images of different loads are called "correlation" points. Thus, the present approach is a "pointwise" DIC technique.

Prior to applying the image correlation algorithm, an image enhancement procedure was also adopted to improve the quantity and uniformity of the key points. The grayscale image of the selected region shown in Fig. 1 (c), before image enhancement, is shown in Fig. 4(a). The key points detected from Fig. 4(a) are displayed in Fig. 4(b). The center of the green circles indicates the key points. Conspicuously, the quantity and density of the detected key points is insufficient as some regions barely contain any key point. To improve the detection of the key points, a 2D Fast Fourier Transform (2D-FFT) is first applied to the grayscale raw image. The transformed image is then filtered using a Gaussian high pass filter in the frequency domain and converted back to the spatial domain using inverse FFT. Finally, to further improve the image intensity and contrast, Contrast-Limited Adaptive Histogram Equalization (CLAHE) was also applied to the image. The grayscale image after the enhancement procedure is shown in Fig. 4(c) and the detected key points are illustrated in Fig. 4(d). Clearly, the image enhancement significantly improved the quantity, distribution, and coverage of the detected key points.

Before deformation and strain analysis, the noise-floor of the DIC algorithm was established. Multiple regions across the ROI were selected and, for each region, a set of 20 images were captured in static state, i.e., no load or motion was applied. In this case, any nonzero strain is considered noise. The local noise was determined in each image and its standard deviation, σ, was averaged over 20 images to achieve $\bar{\sigma}$. Three times the averaged standard deviation, i.e., $3\bar{\sigma}$, for each calculated quantity of interest (QOI), i.e., deformation or strain, is considered as the threshold for noise-floor of that QOI [126, 127]. To minimize the noise, the parameters of FFT, CLAHE, local contrast and key point descriptors were adjusted after rigid body correction. The displacement noise-floor was found to be below 0.005 pix and strain noise was about 28 $\mu m/m$. To reduce the effect of noise on the strain distribution, a Gaussian smoothing kernel with standard

18

deviation of $6\bar{\sigma}$, was applied, followed by another Gaussian smoothing with 10 point moving average.
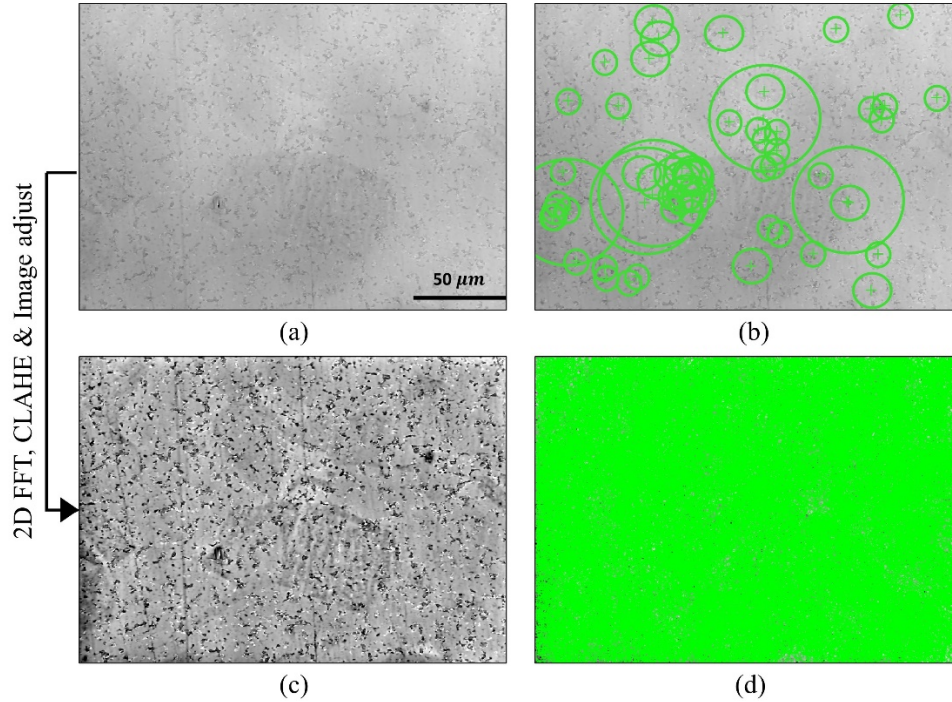
Fig. 4 (a) Gray scale image for a region inside the ROI and (b) its corresponded registration points, indicated by green circles, before image enhancement. (c) The gray scale image of the same region after image enhancement and (d) the improved registration points covering the entire area.

2.4 In-plane strain measurement

2.4.1 validation with commercial DIC software

Calculating the in-plane 2D strain components using the present method was first validated by processing the same image using a commercial DIC package, "GOM Correlate" and comparing the results obtained using both methods. The subset size and step size in GOM software was set at 39×39 and 3 pixels, respectively. The contours of the vertical deformation v in a region at 900 N, obtained using the present method and the GOM software, show qualitative agreements, as shown in Fig. 5(a) and (b). For a more in-depth quantitative comparison, the variations of the deformation along the horizontal centroidal axis of the image are compared in Fig. 5(c). Since the

19

GOM correlate software applies a subset based DIC analysis with averaging while the current method is a point-wise image correlation, the displacement profile obtained with the GOM software appears as a smoothed curve of the profile obtained using the present method.

(a)   (b)   (d)   (e)

(c)   (f)
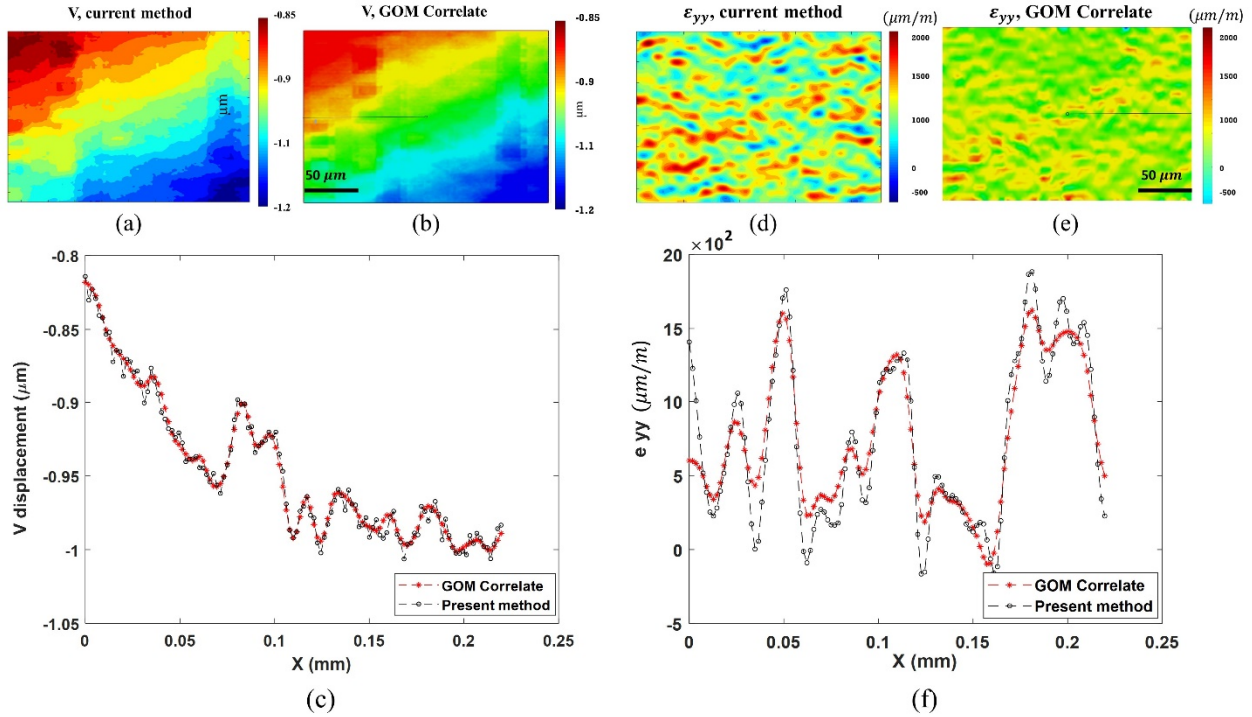
Fig. 5 Comparison of deformation and strain distribution evaluated by two DIC approach in a region inside ROI. Vertical deformation contour obtained by (a) present method, (b) GOM correlate and (c) variation of deformation along horizontal centroidal axis for both methods. ε_{yy} strain obtained from (d) present method (e) GOM correlate and (f) strain variation along the horizontal centroidal axis for both methods

The contour of the normal strain ε_{yy} calculated from the displacement v, using the two methods, are shown in Fig. 5(d) and (e), respectively. The variation of strain along the same horizontal centroidal axis is plotted in Fig. 5(f). Again, the strain profile produced by the GOM correlation appears as a smoothed version of that produced by the present method. The agreements between the two methods validate the accuracy of the proposed technique for in-plane strain calculation.

The distribution of the three in-plane strain components within a selected region inside the ROI, acquired at 500 N, 900 N, 1000 N and 1075 N, are displayed in Fig. 6. At 500 N, the strain

20

distribution is relatively uniform without much localization. However, at higher loads, specifically from the yield point (1000 N) onward, a pattern of strain accumulation is evidently observed. Since the sample was loaded along the Y direction, the intensity and extent of the strain accumulation is more severe in ε_{yy}. At 1075 N, the average global strain applied was 1500 $\mu m/m$ while the local strain can be up to 8500 $\mu m/m$.
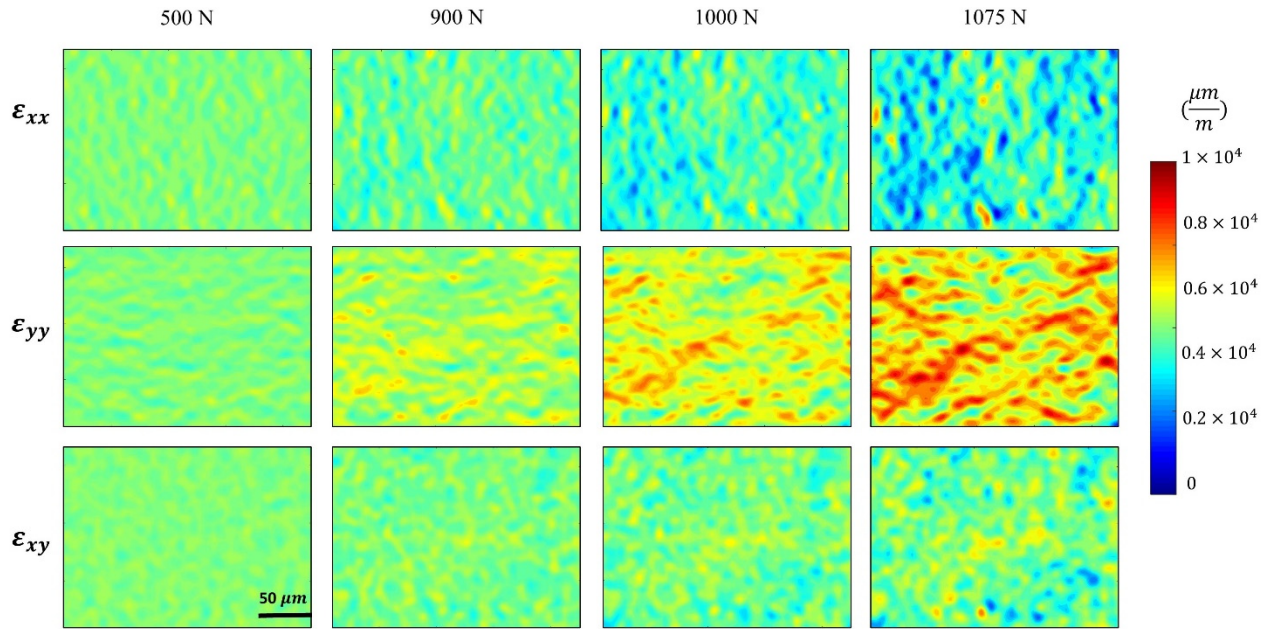
Fig. 6 In-plane strain components ε_{xx}, ε_{yy} and ε_{xy} at different loading levels. The unified color bar shows the intensity of strain accumulation. The difference in strain accumulation intensity at the end of the experiment is apparent for different strain components

2.4.2 Effective plastic strain

The effective plastic strain, a scalar quantity that has been investigated in numerous studies as the damage index in ductile materials [43, 56, 58, 63], is calculated as

$$\varepsilon_{eff} = \sqrt{\frac{2}{3}\left(\varepsilon_{i,j} \times \varepsilon_{i,j}\right)}. \qquad\qquad 2.1$$

In addition to the in-plane strain components obtained from DIC, the out-of-plane normal strain ε_{zz} was calculated from the in-plane normal strains assuming the plane stress condition and plastic

incompressibility, i.e., $\varepsilon_{zz} = -(\varepsilon_{yy} + \varepsilon_{xx})$. The out-of-plane shear strains, ε_{yz} and ε_{xz} were assumed to be zero, following the same practice in [43, 56, 58, 63]. Fig. **7** depicts the effective plastic strain distribution. Similar to the individual strain components, the localization of the effective strain accumulation pattern is first observed at 900 N and noticeably intensifies after the yield point. Comparing Fig. 6 and Fig. 7 reveals that the effective plastic strain is clearly dominated by the ε_{yy} component. Overlaying the grain map on the effective plastic strain contour reveals that the strain accumulation takes place within some of the grains and might be extended to the neighbor grains or pile up at one side of the grain boundary. Visually, there appears to be more than a dozen "hot spots" at 1075 N, as shown in Fig. 7. It is unlikely all these "hot spots" will eventually lead to crack nucleation. Therefore, the effective plastic strain may not be a "good" indication of material damage.
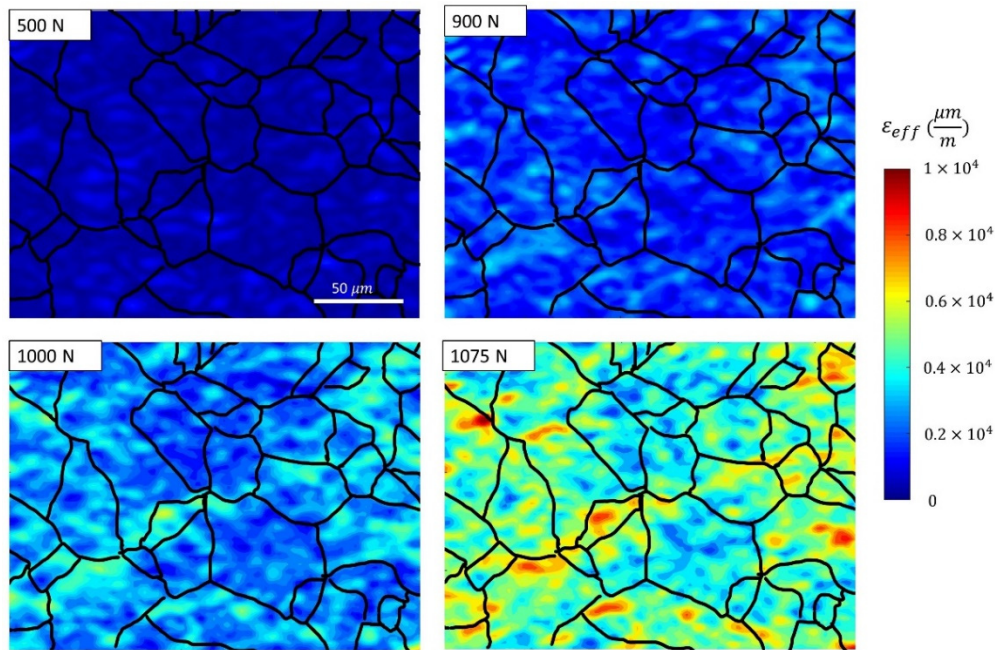
Fig. 7 Effective plastic strain distribution overlaid on the grain boundary map at 500 N, 900 N, 1000 N and 1075 N. Microstructure effect on intragranular strain localization is evidently observed within, across or along the grain boundaries.

2.5 Combined effective strain-surface roughness damage index

For damage index calculation, the image of the analyzed region is divided into 40 subsets, resulting in 75×75 pixels in each subset. Note that the subset for damage index calculation is different from the subset for strain calculation using conventional DIC, in which, the subsets are predefined areas used in the correlation process to identify the matching subsets. However, the subset for damage index calculation in this study is a region enclosing a certain number of correlation points with their strain values identified using the proposed pointwise DIC technique. Thus, these subsets are used for statistical evaluations, i.e., strain averaging and mean surface height, to construct the damage index map. Ideally, the subset size for damage index calculation should be as small as possible for finer resolution of damage identification. On the other hand, the subset size should be large enough to capture the out of plane movement of the grains and contain sufficient correlation points for reliable strain and surface roughness evaluation. Considering the grain size varying between 10 to 120 μm, our evaluation suggests that a 75×75 pixel subset is a good tradeoff between these considerations. The resolution of the damage index, determined by the size of the subset, is therefore 27 μm along the lateral direction. For each subset, the effective plastic strain damage index, D_ε, is defined as

$$D_\varepsilon = \frac{\overline{\varepsilon_{eff}}}{\max{(\overline{\varepsilon_{eff}})}}, \qquad\qquad 2.2$$

in which $\overline{\varepsilon_{eff}}$ is the effective strain, calculated using eq 2.1, averaged over all 75x75 pixels in one subset. For each subset, the damage index is normalized with respect to the maximum effective strain, $max(\overline{\varepsilon_{eff}})$ of all 40 subsets. Its value is therefore between 0 and 1, with 1 representing the

highest damage index at each loading level. Similarly, the surface roughness damage index D_{Ra} is defined as

$$D_{Ra} = \frac{R_a}{max(R_a)}, \qquad\qquad\qquad 2.3$$

in which R_a denotes the arithmetic average surface roughness in a subset, which is calculated after subtracting the surface height of the deformed image from the undeformed reference image, i.e., the image taken before starting the test. Again, $max(R_a)$ is the maximum R_a of all 40 subsets. Finally, the combined effective strain-surface roughness damage index is defined as the multiplication of these two damage indices, i.e.,

$$D_{com} = D_\varepsilon \times D_{Ra}, \qquad\qquad\qquad 2.4$$

The combined strain-roughness damage index map at 500 N, 900 N, 1000 N and 1075 N are displayed in Fig. 8(a). To compare these three damage indices, their performances in identifying the damage localization sites are analyzed in terms of damage localization and localization consistency. Damage localization happens when the intensity of the damage index at a few subsets (i.e., the critical subsets) is substantially higher than the rest of the subsets. For example, subsets 9, 27, 28 and 33 show a significantly higher intensity at 1000 N and 1075 N. Damage localization can be better assessed by plotting the damage index of each subset versus the applied loads, as shown in Fig. 8(b). For visualization, the intensity plots of the four critical subsets, i.e., subsets 9, 27, 28 and 33 are indicated as bold solid lines while the other subsets are plotted in dashed lines with their visibility being slightly suppressed to avoid interfering with tracking the four critical subsets. The intensity of subset 9 at 900 N, and subsets 27, 28 and 33 at 950 N, start diverging from the rest of the subsets, whose damage indices are decreasing. After 950 N, subset 9 shows the highest intensity followed by subsets 28, 27 and 33. The average intensity of these subsets is

substantially higher than the other subsets. For example, after the yield point, i.e., at 1000 N, the intensity of the other subsets falls between 0.2 to 0.6 and falling while the intensities of the four critical subsets are greater than 0.7 and rising, indicating that damage is localized at these four subsets. Localization consistency means once the localization takes place, a critical subset maintains a substantially higher damage index in subsequent loads. After 950 N, as the load increases, the critical subsets further diverge from the descending subsets, indicating a consistent damage localization. Despite some fluctuations in the damage indices, we can confidently conclude that subsets 9, 28, 33, and 27 are the damage accumulation sites at 1000 N.

(a)   (b)
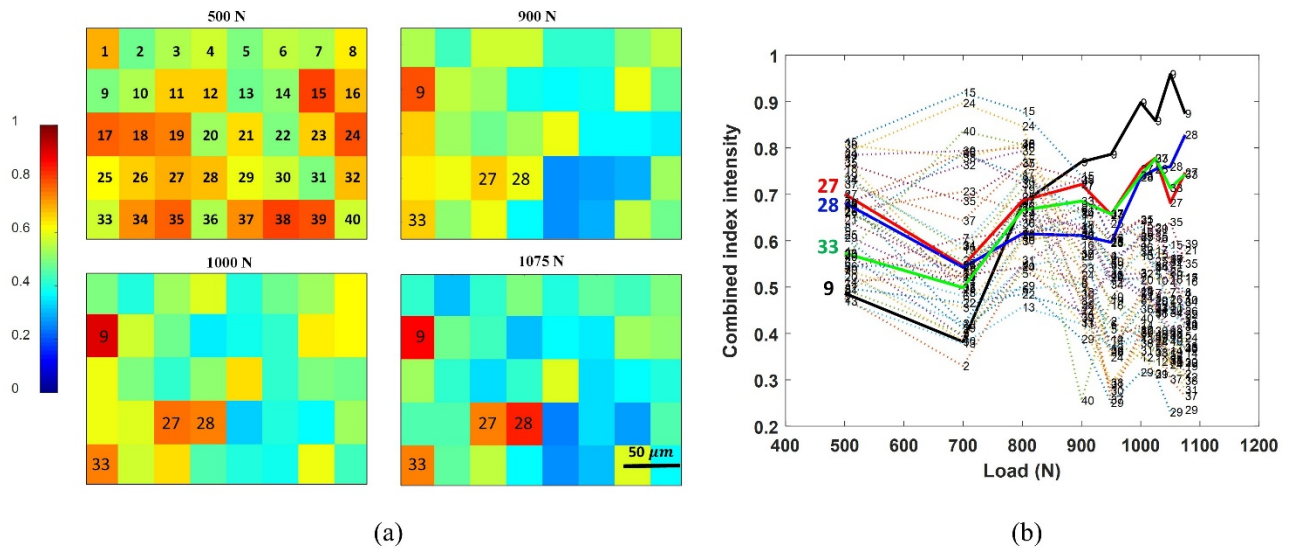
Fig. 8 (a) Combined damage index map at 500 N, 900 N, 1000 N and 1075 N. (b) Intensity variation of each subset at different load levels. The subset number is used as the marker of the plots for reference

For comparison, the effective strain and surface roughness damage indices are plotted separately versus the applied loads and are illustrated in Fig. 9(a) and (b), respectively. For D_ε, a slight localization is observed around 950 N, at which the intensity of subset 26 is higher than the rest of the subsets. However, the divergence is not maintained in subsequent loads. As the load increases, several other subsets also have comparable damage indices as that of subset 26. Furthermore, the damage index in all subsets is above 0.6 but none of the subsets has a substantially

higher damage index than the others. In other words, the localization of the effective strain damage index reduced with the increasing load. As a result, we cannot confidently identify the critical subsets based on D_ε. Among the four critical subsets identified by D_{com}, D_ε of subset 9 only advances to the top until after 1025 N and subset 28 has an average D_ε. Thus, the effective strain index shows a low degree of localization, i.e., the damage indices of the critical subsets are not substantially higher than those of the other subsets, and a poor consistency in identifying damage accumulation sites. The localization, as evaluated by D_{Ra}, is slightly improved. The intensity of subsets 9 and 28 starts to diverge from the rest of the subsets at 900 N and 950 N, respectively. Even though the intensity of subset 9 drops at the final load, its average intensity, along with subset 28, remain substantially higher than the other subsets. Thus, D_{Ra} is more consistent in identifying the critical subsets than D_ε. On the other hand, subsets 27 and 33, identified by D_{com} as the critical subsets, have D_{Ra} that do not diverge from those of the other subsets. Between 900 N and 1000 N, subsets 4 and 21 had higher D_{Ra} than these two subsets. At 1025 N, a second tier of subsets that have a relatively large D_{Ra}, including subsets 27, 33, 4, 21, and 39, starts to emerge. Their damage indices are very close to each other but follow a decreasing trend. It is therefore difficult to decide whether these second-tier subsets are critical subsets or not. Comparing to D_{com}, the localization and consistency of subsets 9 and 28 are comparable but the second-tier subsets have a lower degree of localization and poor consistency. Subset 27 and 33 would not be classified as critical subsets based on D_{Ra} alone. Due to their relatively large D_ε, however, they are identified as the critical subsets by D_{com}.
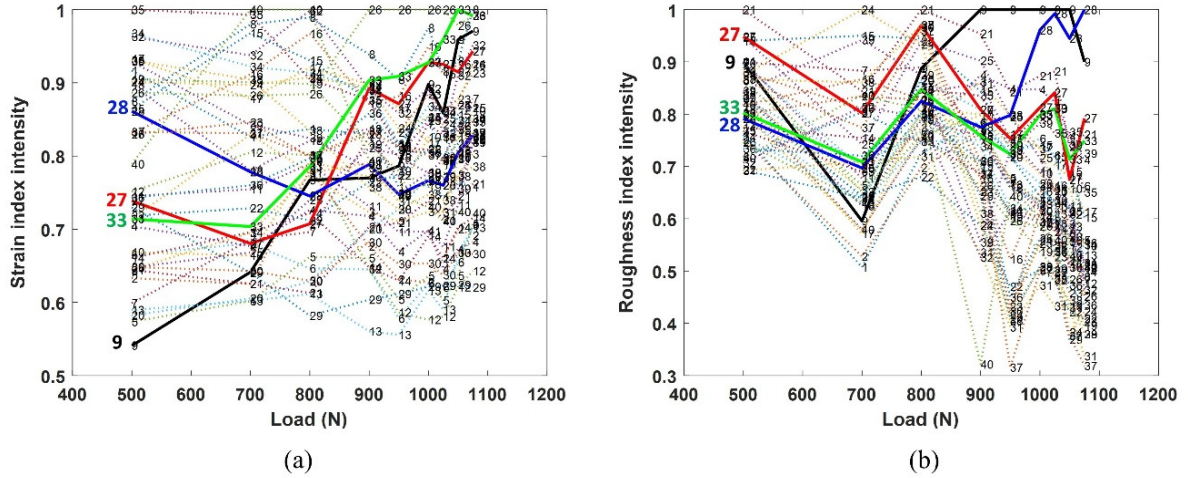
Fig. 9 Evolution of (a) the effective strain index and (b) surface roughness damage index with the applied load

To investigate the correlation between the damage accumulation site and the microstructure, the grain boundary map is overlaid on the combined damage index map in Fig. 10(a). Since the microstructure is closely related to the surface topography changes, the surface topography image acquired at 1075 N is shown in Fig. 10(b) and its 3D view is shown in Fig. 10(c) for better visual perception. In Fig. 10(c) the areas in blue have "sunken" grains and the areas in red have "risen" grains [128]. The only exception is a big grain to the right of subset 28, which is originally depressed after etching. The critical subsets identified by D_{com} and the second-tier subset identified by D_{Ra} are marked with two tags. The first tag shows the subset number, and the second tag indicates the associated damage index highlighted in either red or yellow. A red tag means the subset is identified as a critical subset by the respective damage index while a yellow tag means the subset is identified as the second-tier subset by D_{Ra}. Among these 7 subsets, subsets 9 and 28 are identified as the critical subsets by both D_{com} and D_{Ra}, subsets 27 and 33 are identified as the critical subset by D_{com} but only as the second-tier subset by D_{Ra}. Three of the four critical subsets identified by D_{com}, i.e., subsets 9, 28, and 33, are dominated by a "sunken' grain. Subset 27 encompasses a few grains, with one of them being "sunken". In addition, one of the grains covered by subset 27 has clearly visible slip bands, the grain covered by subset 9 has slightly visible slip

27

bands, and subsets 28 and 33 do not have any slip bands. Therefore, the critical subsets do not necessarily have to have slip bands. Subsets 33 and 27 are only classified as the second-tier subsets by D_{Ra}. They, therefore, must have relatively large D_ε values to be identified by D_{com} as the critical subsets. Two of the three remaining second-tier subsets, i.e., subsets 4 and 39, are dominated by "risen" grains. Subset 21 covers a "risen" grain and the originally depressed grain, which could have risen but does appear to be so because of its original depression. Referring to Fig. 9(a), all these three subsets have below average D_ε.
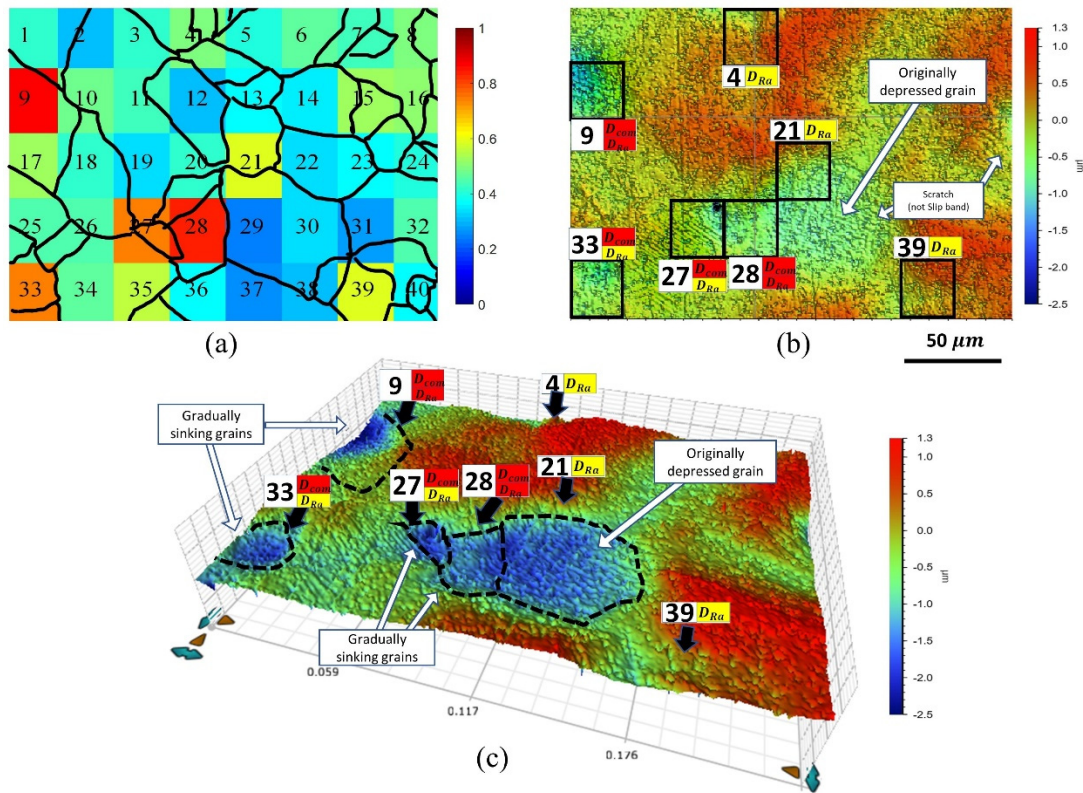
Fig. 10 (a) Combined damage index map with grain boundaries, (b) 2D view of the surface profile at 1075 N, and (c) 3D view of the surface profile with a better visual representation of damage initiation spots

The grains covered by these 7 subsets and their immediate neighbors are indicated by a unique number and shown in Fig. 11(a). The dashed squares mark the locations of the subsets: subsets 9 and 28 are in red, subsets 33 and 27 are in orange, and subsets 4, 21, and 39 are in blue. The crystallographic orientations of the grains are plotted in a pole figure shown in Fig. 11(b). The

grain numbers are color coded: the ones associated with subsets 9 and 28 are in red, the ones associated with subsets 33 and 27 are in orange, and the ones associated with subsets 4, 21, and 39 are in blue. The "sunken" grains associated with the critical subset identified by D_{com}, i.e., grains 1-4, have crystallographic directions close to <001> or <111>. This is consistent with the conclusions of [128], i.e., when considering the loading direction, grains with a crystallographic direction close to <001> or <111> are more prone to sinking while grains leaning toward <101> direction usually have no preference over sinking or rising [128]. The rest of the grains shown in Fig. 11(b) are associated with the three second-tier subsets identified by D_{Ra}, i.e., subsets 4, 21, and 39. Their crystal orientations are clustered in the middle or toward the <101> direction. Notice that the "sunken" grains in subsets 27 and 33 are closer to the "sunken" grain in subset 28 while away from the grains in the subsets 4, 21, and 39. This suggests that subsets 27 and 33 are more likely to be a damage accumulation site, indirectly validating that D_{com} is correct in detecting these two subsets as the critical subsets.

The subset number, their associated grains and the misorientation between these grains are presented in Table 1. The four critical subsets identified by D_{com} have a " ∗ " superscript while the second-tier subsets identified by D_{Ra} have a "Δ" superscript. Grain #1, associated with subset 9, has a 38° misorientation with grain #5 while grain #2, associate with subset 28, has a misorientation of 41º with grain #8. Grain #4, associated with subset 33, has a misorientation of 30º and 26º with grain #10 and #9, respectively. The "sunken" grain # 3, associated with subset 27, have a misorientation of 36°, 21°, 26° and 12° with grain #6, #7, #8 and #11, respectively. Grain #11, the grain having clearly visible slip bands, also has a large misorientation with its neighbor grains. These grains create a shielding boundary effect that confines the slip bands within grain #11. Interestingly, the grains associated with the other three second-tier subsets all have

29

relatively small misorientations with their immediate neighbors. Qualitatively speaking, the four critical subsets identified by D_{com} have relatively larger misorientations than those in the three second-tier subsets only identified by D_{Ra}. These results suggest that D_{com} performs better than D_{Ra} in capturing damage accumulations associated with large microstructure misorientations.

The region presented above covers almost 20% of the ROI. It was selected for in-depth analysis and discussions because it has notable slip band formations and large out of plane deformations. Analyzing a few other regions yielded similar results and thus they are not discussed here to avoid redundancy. Since damage localization is the precursor of fatigue cracking, the combined damage index will be investigated for predicting fatigue micro-crack propagation path in the next chapter.

Theoretically, the out-of-plane strain components can be calculated if all three displacement components are known, i.e., $\varepsilon_z = \frac{\partial w}{\partial z}, \varepsilon_{xz} = \frac{\partial u}{\partial z} + \frac{\partial w}{\partial x}, \varepsilon_{yz} = \frac{\partial v}{\partial z} + \frac{\partial w}{\partial y}$, in which u, v, and w are the displacements along the x-, y-, and z- directions. ∂x, ∂y, and ∂z are the differences between the coordinates of two locations. In this study, the displacements were measured on the surface. Due to the highly polished surface, ∂z, i.e., the height differences between two locations, is very small. As such, small errors in the displacement calculation could lead to large errors in the out-of-plane strain calculation. In chapter 3 we will discuss FEM simulation to investigate a threshold value for minimum surface height difference to reduce error in calculating the out-od-plane strain components. The capability to measure the out-of-plane strains accurately will enable comparing the combined damage index with other fatigue damage indices such as the resolved shear stress.
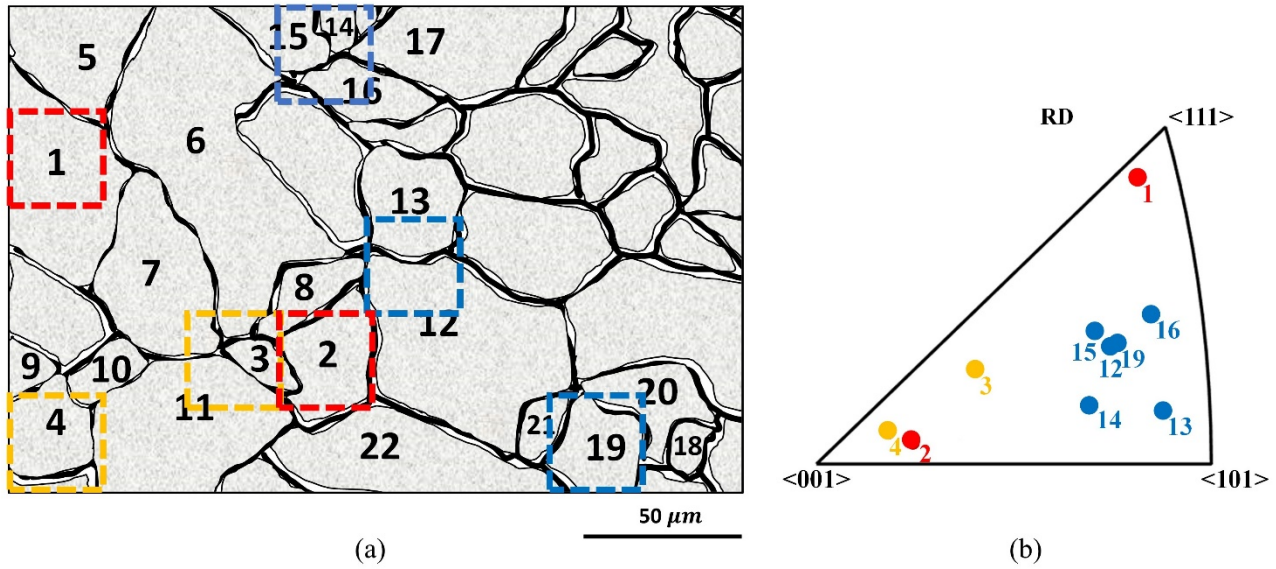
Fig. 11 (a) Grain map with the grains associated with the critical and second-tier subsets indicated by a unique number. (b) Pole figure of the candidate grains obtained from EBSD analysis

Table. 1 Critical and second-tier subsets and their associated grains and misorientation angles

Subset	Associated grains #	Misorientation between grains	
		Grain pair	Misorientation angle
9*	1	1, 5	38°
28*	2	2, 8	41°
		2, 12	25°
33*Δ	4	4, 10	30°
		4, 9	26°
27*Δ	3, 6, 7, 8, 11	3, 6	36°
		3, 7	21°
		3, 8	26°
		3, 11	12°
		11, 7	33°
		11, 10	27°
		11, 22	31°
4Δ	14, 15, 16	14, 15	12°
		15, 16	7°
21Δ	12, 13	12, 13	16°
39Δ	19	19, 20	14°
		19, 21	12°

* Critical subsets identified by D_ε

Δ Second-tier subsets identified by D_{Ra}

2.6 Chapter summary

A combined effective strain-surface roughness damage index is reported for damage localization identification in a tensile sample. The proposed damage index yielded a significant enhancement in damage localization and localization consistency compared to the damage indices based on either the effective strain or the surface roughness alone. The damage accumulation sites identified were analyzed with respect to the crystallographic direction and grain structure. They were found to cover a "sunken" grain that has significant misorientations with its neighboring grains. In addition, a simple technique to apply a fine speckle pattern on the sample surface is introduced. The random, micro-sized, reflective speckles produced enable sub-grain digital image correlation analysis of the surface topography images. The proposed technique and damage index will be extended for investigating fatigue damage development in the next chapter.

Chapter 3. Combining Effective Plastic Strain and Surface Roughness for Predicting Future Propagation Path of Small Crack in Polycrystalline Nickel

3.1 Introduction

Fatigue is the precursor of numerous structure failures leading to calamitous tragedies. Despite intensive research conducted by the fatigue community, the driving mechanism of fatigue damage is not fully apprehended [53, 54, 129–132]. While phenomenological models such as Paris' law are well applicable to the second stage of crack growth i.e., where the crack path is macroscopical and more affected by far field stress, it is inadequate to describe the erratic behavior of microstructurally small crack (MSC), i.e., when the crack propagation is primarily dependent on local microstructure [56, 133]. Although immense studies have been devoted to further elucidate the mechanism of fatigue crack growth [134–143], predicting the propagation path of MSCs is still an unresolved problem [54]. The challenge lies in defining and experimentally verifying fatigue indicator parameters (FIPs) that considers different factors contributing to the complex micro-crack growth behavior.

Various FIPs have been proposed to investigate crack nucleation and MSC propagation, e.g., resolved shear stress [12–14], effective plastic strain [12, 24, 27, 99–101, 144], maximum cyclic plastic shear strain, a.k.a., Fatemi-Socie parameter [15–18], stored energy density [19–22], energy dissipation during crystallographic slip [6, 23, 102], etc. Most of these FIPs require the knowledge of all six stress/strain components. Since the out-of-plane stress/strain components are difficult to measure experimentally, studies on these FIPs relied on simulations, such as Crystal Plasticity Finite Element (CPFEM), to calculate all six stress/strain components. However, due to imperfect

constitutive laws, insufficient knowledge of microstructure feature underneath the surface, and inadequate computational capacity, simulations cannot represent the entire microstructure faithfully and therefore, are seldom verified by experiment and inaccurate in practice [103, 145]. Despite the developments in 3D characterization of material microstructure, e.g., X-ray Computer Tomography (XCT) and High Energy Diffraction Microscopy (HEDM) [104–109], the correlation between experiment and simulation has not been successfully achieved and remains under active investigations [9, 145].

Experimental works on driving mechanisms of crack nucleation and MSC growth in ductile fatigue have been focusing on plastic deformation and strain localization [11, 34, 53–55, 146, 147]. The plastic deformation is perceived to cause surface topography changes in ductile materials under fatigue [53, 54, 147]. These surface topography changes are observed in the form of out-of-plane grain movement and formation/accumulation of intrusion and extrusion bands, i.e., persistent slip bands [55, 86]. Surface roughening, in turn, prompt stress concentration and strain localization, facilitating the onset of stage I crack initiation and growth [53, 54, 90, 102, 124]. Various surface morphology characterization tools have been used to measure surface topography change associated with fatigue in ductile materials. Atomic Force Microscopy (AFM) has been utilized to quantitively extract 3D surface features in materials under static and cyclic load [123, 148–151]. These studies, however, observed a small area focusing on slip band formation and intrusion/extrusion height measurement [122, 150–153]. Scanning White Light Interferometry (SWLI) [48, 51, 52, 112, 147, 154], Scanning Light Confocal Microscopy (SLCM) [124, 155–157], stereological imaging [110] and phase shifting interferometry [49] have also been used to study the surface topography changes induced by plastic deformation in fatigue samples. However, these studies either focused on surface morphology change over a large area and thus overlooked

the microstructure details [50, 52], or considered a few data sets over a small region, failing to achieve a damage map over a large region of interest (ROI) with detailed representation of local strain accumulation and localization [122, 151, 152]. Recently, a full-field surface roughness damage index (DI) was proposed using high resolution SWLI surface topography images to predict the MSCs initiation site and future propagation path at microstructure level [53, 54]. However, these works, similar to other surface morphology studies, were merely concerned with the out-of-plane displacement associated with plastic deformation without considering the in-plane strain components.

Recently, grain scale strain accumulation and localization have been intensively studied using High Resolution Digital Image Correlation (HR-DIC) [5, 41, 110, 158, 43, 56, 58–63]. Using high magnification optical microscope, HR-DIC has been implemented in many studies to investigate grain scale strain distribution and its correlation with microstructure. Since the spatial resolution of an optical microscope is limited to half of the wavelength of the illumination light, the grain sizes for these studies are relatively large. To achieve sub-grain strain resolution in small grains, DIC technique based on Scanning Electron Microscopy (SEM) has been implemented [16, 64, 66–71, 159]. Using these techniques, researchers were able to study the correlation between fatigue crack initiation/growth and strain localization [72–74], Schmid factor [70, 112] , grain orientation [65, 71, 76], slip transfer [16, 66, 77, 158] and presence of voids [78]. However, some of these correlations were either qualitative in suggesting fatigue damage development sites [36, 66, 79] or offered quantitative evaluations only after crack has initiated/propagated [22, 69, 80, 81]. Additionally, in both cases, the temporal resolution of the analysis was relatively low, i.e., only a few fatigue intervals were studied. More importantly, these studies were performed in 2D which can only measure in-plane strains omitting the out-of-plane plastic deformation.

3D volumetric DIC or stereovision DIC can measure both in-plane and out-of-plane deformations at the surface. These techniques require two cameras being synchronized and calibrated at a certain angle with respect to specimen surface. Researchers were able to apply stereovision DIC techniques to study the strain heterogeneity/accumulation at grain level under monotonic and cyclic loading [5, 68, 82, 83, 110]. However, for high magnification measurements that have very small field of view, the camera lenses need to be very close to the sample surface, as dictated by the focal plane. In many cases, placing two lenses in a very tight space may not be practical and thus restricts the use of high magnification lenses. As such, sub-grain studies were focused on large single/oglio crystals so that strain variations within grains can be measured using low magnification lenses. Additionally, these techniques might not provide sufficient vertical resolution to capture plasticity induced surface roughness change which can be in the order of tens of nanometers [53, 54, 145].

In this chapter, extending our previous work [145], discussed in previous chapter, a fatigue damage index combining effective plastic strain and surface roughness change is studied for predicting future microcrack propagation path. A DIC technique based on high resolution SWLI surface topography image is used to measure both in-plane and out-of-plane surface deformation at sub-grain scale. The accumulated plastic strain and surface roughness change are calculated over fatigue intervals during the crack arresting period. The damage index map is constructed over a large region of interest (ROI) ahead of the crack tip. Two approaches, based on highest intensity subsets and statistic confidence threshold, are developed and evaluated for predicting the future crack path. The performances of three damage indices, i.e., the effective plastic strain, the surface roughness change, and the combined damage index, are assessed in terms of prediction accuracy, confidence, and certainty.

3.2 Methods

3.2.1 Sample preparation

The fatigue study was carried out on a middle tension (MT) sample made of pure nickel, aimed at gaining understandings on how effective plastic strain and surface roughness affect fatigue development in face-centred cubic (FCC) crystalline materials. Thin oxide layer on the surface of nickel enables investigating surface topography changes during fatigue experiment. Annealed nickel with 99.52% purity was selected for this study. The EBSD analysis of the as-received nickel sheet revealed an average grain size of 89 μm and a random distribution of grain orientation, confirming the material is isotropic. A static tensile test was conducted on a dog-bone sample according to American Society for Testing and Materials (ASTM) E8, standard test methods for tension testing of metallic materials. The 0.2% yield stress of the material was measured to be 211 MPa.

The middle tension (MT) sample was designed according to ASTM E-647, standard test method for measurement of fatigue crack growth rates. The schematic of the sample is shown in Fig. 12(a). Using Electrical Discharge Machining (EDM) with a 0.254 mm wire, a 4.83 mm center notch was machined. The surface of the sample was manually polished using sandpapers starting at P300 down to P1500 in FPEA standard, followed by two steps of ultrafine micro polishing using alumina powder of sizes 1 μm and 0.3 μm, respectively. The surface roughness in front of the notch tip reached 12 nm at the end of micro polishing. After slightly etching the vicinity of the notch to reveal grain boundaries, the average surface roughness was increased to 110 nm.
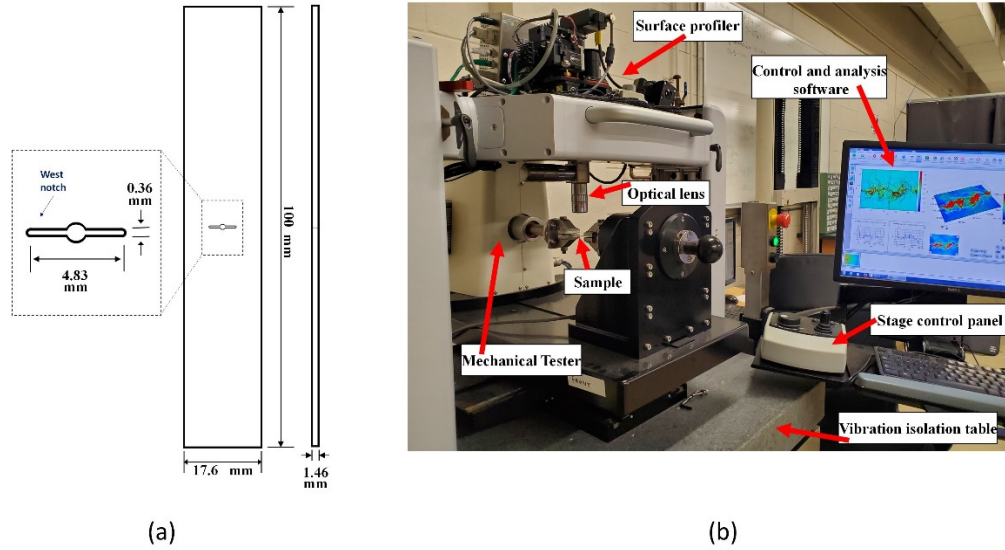
Fig. 12 (a) Schematic of the fatigue sample with a center notch, (b) experiment setup showing the integrated testing machine with the scanning whitelight interferometry (SWLI) surface profiler and control software.

For DIC analysis, a speckle pattern was coated on the surface following the same practice in [145]. Briefly, alumina powder in two sizes of 0.3 and 0.05 μm, with respective weights of 0.5 and 0.1 g was mixed with 6 g of water in a stirrer for about 1 hour at 40℃. To increase the adhesion of the speckles to the sample surface, 1 g of Polyvinyl Epoxy, a clear substance that dissolves in water without leaving any artifacts, was added to the mixture, and stirred for additional 45 minutes in 100℃. The mixture was applied to the surface using a micro-polishing pad. Afterwards, it was thoroughly washed to remove the excessive layers and then dried in air. This technique produced a thin and reflective layer of randomly distributed speckles on the surface, with an average size of roughly 1.1 μm. More details on the quality of the speckles produced by this technique can be found in [145].

3.2.2 Fatigue test

A Bose LM2 ElectroForce test bench with a maximum capacity of $\pm3000\ N$ at $100\ Hz$, was integrated with a Bruker NPFLEX SWLI surface profiler as shown in Fig. 12(b). A 50X magnification lens with a lateral resolution of $0.366\ \mu m/pix$ was used to capture the surface topography images. Each single SWLI image contains 640×480 pixels and thus the area it covers is $234 \times 175\ \mu m^2$. An area of $1 \times 1\ mm^2$ ($0.1\ mm$ behind and $0.9\ mm$ in front of the notch tip) was considered as the primary region of interest (PROI). To cover the entire PROI, a set of 89 single SWLI images were taken with a 50% overlap in both horizontal and vertical directions. This was accomplished using Bruker Vision64 software which controls the traverse motion of the lens. The 50% overlap ensures that each quarter of the imaged region is captured by four images and thus providing redundant data for analysis. The single SWLI images were stitched in Vision64 software to construct the surface topography of the entire PROI. The PROI for the west notch is indicated by dash yellow line in Fig. 13.

The first surface topography image was taken from the pristine sample, i.e., after etching but before the test. Based on previous experiments on a similar sample [53, 54], the fatigue load started at $2800\ N$ to ensure crack initiation while the sample remains primarily elastic. Given the applied load and sample configuration, the stress intensity factor (SIF) was $9.95\ MPa.\sqrt{m}$ at the beginning of the experiment. Throughout the entire fatigue test, the load frequency and ratio were set at $10\ Hz$ and zero, respectively. The surface topography image of the loaded sample was taken immediately after the first cycle and then every 500 cycles afterwards, up to 5,000 cycles. The surface topography images were taken when the sample was unloaded. Therefore, the deformations measured are mostly plastic but could contain elastic components due to strain inhomogeneity. At 5,000 cycles, the fatigue intervals increased to 1,000 cycles for up to 20,000

cycles and further increased to 2,000 cycles thereafter. The maximum load was maintained at 2800 N until crack initiation was observed at the notch tip at around 60,000 cycles. The crack was grown 100 μm over an additional 30,000 cycles, until it turned into a dominant crack in front of the notch tip. During this period, i.e., from 60,000 to 90,000 cycles, the SIF was allowed to gradually increase to 10.12 $MPa.\sqrt{m}$. For this purpose, the test was stopped every 1,000 cycles to capture the surface profile image and measure the crack length. The load level was then adjusted accordingly to ensure the plastic zone was not grown more than 5% of the previous interval [54, 147]. After 90,000 cycles, the fatigue interval was reduced to 500 cycles and the SIF was maintained at 10.12 $MPa.\sqrt{m}$. To maintain a SIF of $K = 10.12$ $MPa.\sqrt{m}$, a load shedding scheme was adopted by measuring the crack length at each interval and adjusting the load accordingly. During the crack length inspection, multiple arresting/pinning locations, i.e., locations where the crack tip stops propagating for a certain period of time, was observed. The pinning period provides the opportunity to study morphological events in front of the crack tip before the crack is released. When the crack propagation was arrested, the fatigue interval was further reduced to 250 cycles after 114,000 cycles, leading to a finer temporal resolution. At 125,000 cycles, the crack tip reached 215 μm in front of the notch and was arrested at this location for 4,500 cycles. This location is marked by 'A' in Fig. 13. An area of 0.45×0.42 mm^2 in front of point 'A' was analyzed in depth for predicting the crack propagation path. This sub-region is termed Region of Interest (ROI) and is illustrated by red dash square in Fig. 13. Considering the 50% overlap, this ROI covers 30 single SWLI images which were analyzed by the image processing technique described below. Crack path prediction was carried out when the crack was pinned at A and at a second pinning location D.
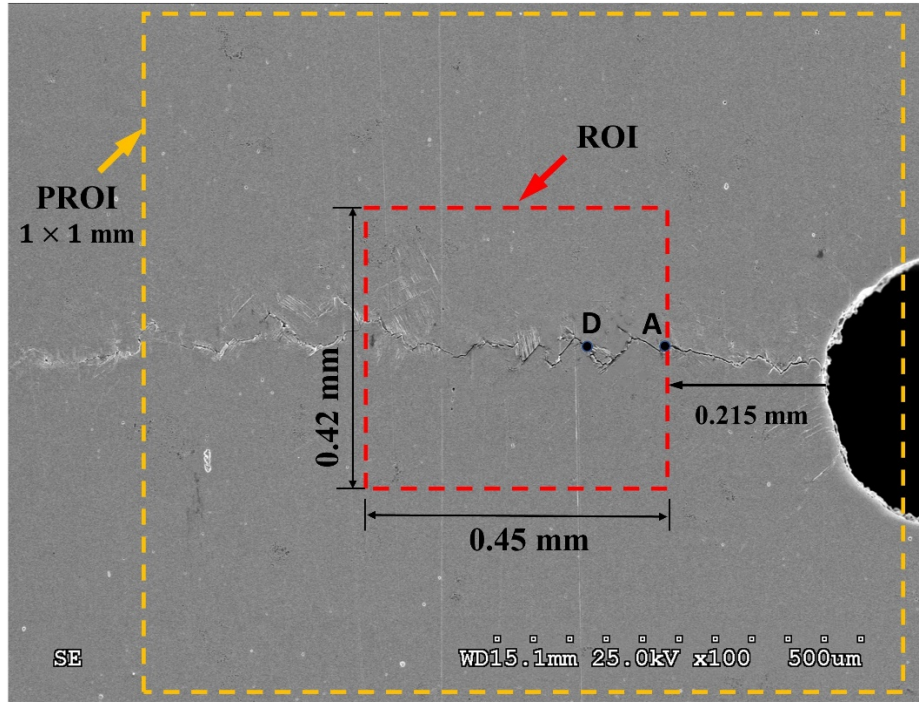
Fig. 13 The primary region of interest (PROI) surrounding the notch tip and the region of interest (ROI) for crack path prediction. Crack path prediction was carried out when the crack tip was arrested at 'A' and 'D'.

3.2.3 Image Processing and DIC

The acquired SWLI surface topography images were processed to obtain surface height change and 2D strain field using DIC, similar to what was described in our previous study [145]. Since stitching the single images generates artifacts in the form of vertical and horizontal bands in overlapped areas [41, 54], the image processing was performed on single SWLI images. After obtaining the surface height difference and 2D strain components, i.e., $\varepsilon_{xx}, \varepsilon_{yy}$, and ε_{xy}, in each single SWLI image, a consolidation scheme was followed to integrate the results into a global frame that encompasses the entire ROI. For this purpose, a global coordinate was defined where the bottom left corner of the ROI was considered as the global origin. In addition, a local coordinate was defined within each single image and the bottom left corner of the image was designated as the local origin. The global coordinate of the identified correlation points in each single image was

then determined by $X_g = x_l + x_{rel}$, and $Y_g = y_l + y_{rel}$ where x_l and y_l indicate the local coordinates within the image while x_{rel} and y_{rel} accounts for the relative coordinate of the local origin with respect to the global origin. Since the identified correlation points in different fatigue intervals might not be the same, it is essential to have a unanimous map of points to compare strain distribution/variation in different cycles. For this purpose, based on the density and distribution of the identified correlation points, a grid network was constructed across the ROI. The average density of the identified correlation points was approximately $6.35 \times 10^5 \ mm^{-2}$, i.e., 130,000 points within the $0.45 \times 0.42 \ mm^2$ ROI. Thus, the increment spacing, i.e., the distance between grid points, was established to be roughly $1.2 \ \mu m$, i.e., $3 \ pixels$, in both x and y directions. The global coordinate of the correlation points and their corresponding strain values at each fatigue interval are then mapped over the grid network to obtain the strain distribution across the entire ROI. Similarly, the surface height difference in each single image has been calculated by subtracting the topography image in the deformed state from its corresponding reference image, i.e., the image taken after the 1st cycle. The height difference across the ROI is then obtained by mapping over the defined global frame.

3.3 Results

The SEM image and surface topography around the crack path within the ROI at the end of the experiment are depicted in Fig. 14(a) and (b), respectively. A few characteristic locations are marked along the cack path. The capital letters show the major pinning locations at where the crack propagation was arrested, and the lowercase letters show sharp turns along the path. After the crack was released from 'A', crack branching is observed at the location marked by letter 'b'. The lower branch is where the crack eventually continues to propagate to arrive at the location marked by

'c'. At this location, the crack was pinned for a short period of 750 cycles. The crack then branches and subsequently merges to arrive at the location marked by 'D' at 163,500 cycles. As the test continued to higher fatigue cycles, the lower branch is observed to be the main crack path as evident by the SEM image in Fig. 14(a). The crack was arrested at 'D' for 6,000 cycles. Given this extended pinning time, the area from 'D' to the end of original ROI, i.e., $0.39 \times 0.42 \ mm^2$, was considered for the second-round of data analysis. The crack was released from 'D' at 169,500 cycles and then took a sharp turn at 'e'. While a short branch was observed near this point, the crack continued to propagate toward 'f'. The crack then changed its direction to move upward followed by another sharp turn at 'g'. Although significant slip band formation was observed in front of this point, the crack propagated toward 'h' along a straight line making a roughly 45° angle with the slip bands. The crack took another upward sharp turn at 'h' and propagated along the slip bands toward 'i'. After a sharp turn and a short propagation after 'i', the crack followed a relatively straight line that is perpendicular to the loading direction, indicating that the crack is less sensitive to local microstructures. The surface topography in Fig. 14(b), shows a significant surface roughening and height variation around the crack path. In addition, multiple "hills", i.e., localized areas with substantially higher surface height than their surroundings, is observed. These hills are formed due to the accumulation of plastic deformation around the crack tip during the crack arresting period, e.g., at 'A', 'c', 'D', 'g', 'h', 'i'. The strain localization and surface topography change during the crack tip arresting period at 'A' and 'D' is investigated to predict the crack tortuous path.
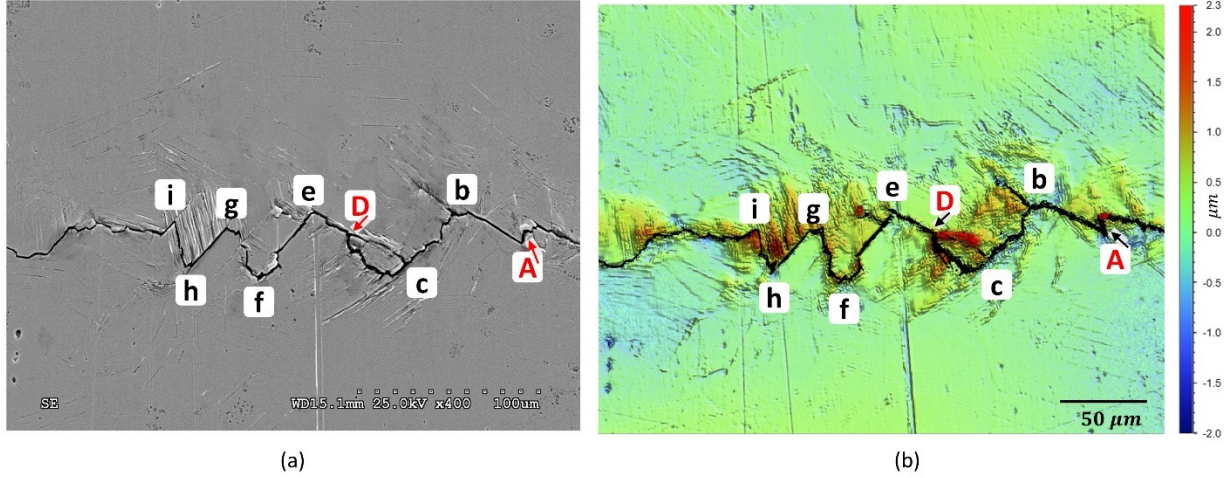
Fig. 14 (a) SEM image and (b) surface topography around the crack path within the ROI at the end of the experiment. Capital letters show the investigated pinning locations and lowercase letters show the sharp turns

Using the obtained global strain fields from DIC, the effective plastic strain, which has been considered as a damage index in ductile materials [43, 56, 58, 63, 145], is calculated as:

$$\varepsilon_{eff} = \sqrt{\frac{2}{3}(\varepsilon_{m,n} \times \varepsilon_{m,n})}, \qquad\qquad m, n = 1,2,3 \qquad\qquad 3.1$$

where the in-plane strain components, $\varepsilon_{xx}, \varepsilon_{yy}$, and ε_{xy} are directly obtained from DIC. The out-of-plane normal strain, ε_{zz}, was determined assuming plane stress condition and plastic incompressibility, i.e., $\varepsilon_{zz} = -(\varepsilon_{xx} + \varepsilon_{yy})$, while the out-of-plane shear strains, ε_{xz} and ε_{yz} were assumed to be zero following the same practice in [43, 56, 58, 63, 145].

The effective plastic strain and the height difference across the ROI when the crack was first observed arrested at 'A' is depicted in Fig. 15(a) and (b), respectively. The high strain regions at the top and bottom right corner, separated by white dash line, are commonly known as heterogenous strain lobes in the crack wake. These plastic strain accumulation lobes extend well beyond the crack tip, i.e., the front of the upper lob is roughly 200 μm ahead of the crack tip. Since these strain lobes do not represent the plastic strain accumulation directly ahead of the crack tip,

44

they cannot be used to predict the crack propagation path. Thus, the effective plastic strain and surface height difference right in front of the crack tip is used to predict the future crack path, which is marked by the black dash line. At first glance, the future crack path does not seem to correspond to the highest strain or height difference regions in front of the crack tip. Thus, for an in-depth quantitative evaluation, a damage index map is constructed to investigate the intensity of the effective plastic strain and surface roughness change.
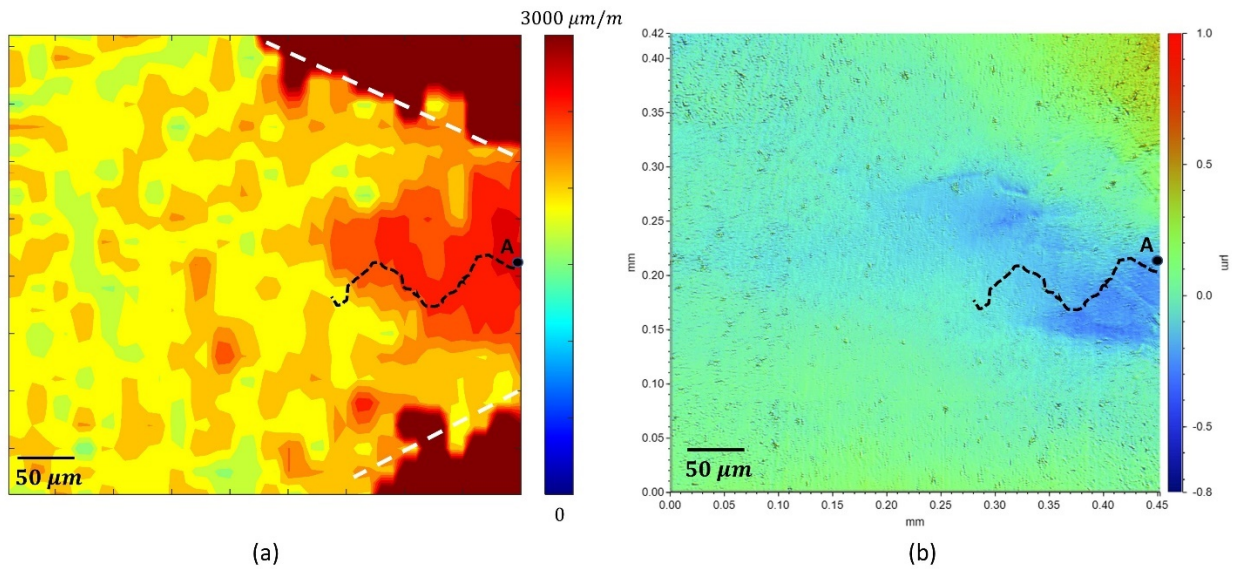
Fig. 15 (a) Effective plastic strain and (b) surface height difference across the ROI when the crack tip was arrested at 'A'. The overlaid dash line shows the future crack path.

3.3.1 Damage index map construction

The damage index map is first constructed over the ROI for effective plastic strain and surface roughness change separately, by segmenting the ROI into 50×50 pixel, i.e., $18.3 \times 18.3 \, \mu m^2$, subsets. This results in a total of 483 susbets, i.e., 23×21 subset in horizontal and vertical direction, respectively. The mean value of the effective plastic strain and surface height difference is then calculated in each subset to construct the damage index map. A single damage index map, constructed at a particular fatigue interval, may not yield a reliable prediction as it does not count

45

for the accumulative effect of the surface topography change over the entire arresting period [5]. Thus, a compound damage index (CDI) is calculated as

$$CDI = D_{in} + \sum_{j=1}^{N} W_j D_j \qquad\qquad 3.2$$

where D denotes the damage indicator, e.g., averaged effective plastic strain or surface roughness change. D_{in} is the initial damage index, obtained by comparing the first surface topography image when the crack was pinned to the reference image, i.e., the image taken after the 1st cycle. The summation term accounts for the accumulation of the damage index during the crack tip arresting period. Assuming a total of N fatigue intervals during the crack pinning period, D_j is the damage index at each fatigue interval j. W_j is the weight coefficient calculated by dividing the average of the damage index at each interval, i.e., $\bar{D}_j$, to the sum of the averaged damage indices over all fatigue intervals as

$$W_j = \left.\bar{D}_j\middle/\sum_j \bar{D}_j\right. \qquad\qquad 3.3$$

The CDI, in each subset is then normalized with respect to the maximum value of the compound index, i.e., $max(CDI)$, as

$$\widehat{CDI} = \left.CDI\middle/max(CDI)\right. \qquad\qquad 3.4$$

Thus, $\widehat{CDI}_\varepsilon$ and $\widehat{CDI}_{Ra}$ represent the compound damage indices calculated from the effective plastic strain and surface roughness change, respectively. Finally, the combined effective plastic strain-surface roughness damage index is defined as the multiplication of these two normalized damage indices, i.e.,

$$\widehat{CDI}_{com} = \widehat{CDI}_{\varepsilon} \times \widehat{CDI}_{Ra} \qquad\qquad\qquad 3.5$$

The three damage index maps are illustrated in Fig. 16(a)-(f). The top and bottom rows show the damage index maps when the crack was pinned at 'A' and 'D', respectively. The highest intensity subsets of the $\widehat{CDI}_{\varepsilon}$ map belong to the crack wake that do not correspond to future crack path. Thus, only the high intensity area directly ahead of the crack tip is considered for crack path prediction. Note that the CDI_{ε} damage index in eq. 3.4 is normalized with respect to the maximum index in front of the crack tip, i.e., subset with maximum intensity outside the strain lobe boundary. Both $\widehat{CDI}_{\varepsilon}$ maps show a high strain accumulation area right in front of the crack tip. This high strain accumulation area narrows down as it moves away from the crack tip at 'A' while ends up with three branches of strain accumulation as it moves away from the crack tip at 'D'. The $\widehat{CDI}_{Ra}$ maps show a few subsets with significantly higher intensity in the fatigue process zone, i.e., the region close to the crack tip, which broadens to lower intensity subsets as it moves away from the crack tip. In comparison, the intensity distribution in $\widehat{CDI}_{com}$ map is similar to the $\widehat{CDI}_{Ra}$ in areas close to the crack tip. In farther regions, the surface roughness index does not provide a localized pattern and gradually levels off. The effective plastic strain, in addition to low degree of localization pattern close to the crack tip, might display multiple accumulation sites in far regions, e.g., branching in Fig. 16(d). Although this branching may result in uncertain prediction by $\widehat{CDI}_{\varepsilon}$ map, when combining with the $\widehat{CDI}_{Ra}$, it contributes to a balanced $\widehat{CDI}_{com}$ map that enhances localization in farther regions from the crack tip. Note that the $\widehat{CDI}_{com}$ map is much less noisy than the other two DI maps. At far region beyond column 11, the relative intensity of $\widehat{CDI}_{com}$ for most subsets are near zero. The other two DI maps, on the other hand, have relatively high intensity subsets, especially for $\widehat{CDI}_{\varepsilon}$, even at regions far away from the crack tip.
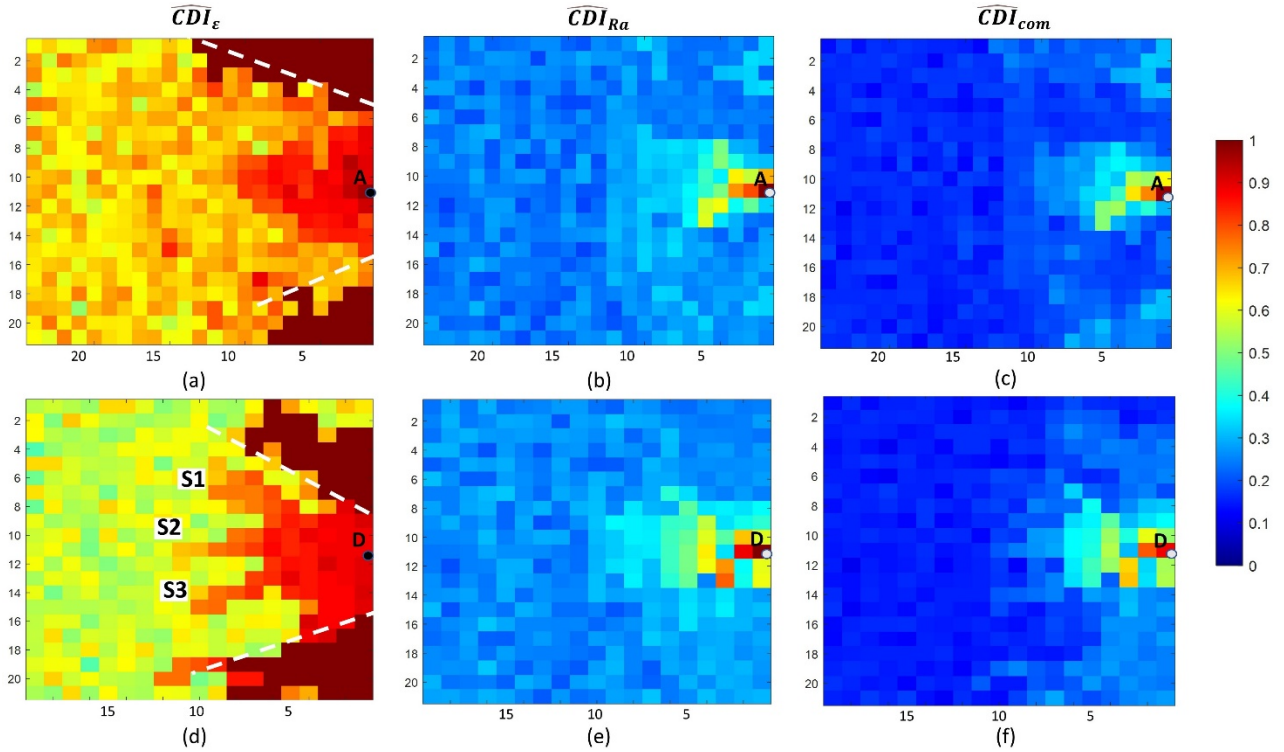
Fig. 16 (a) $\widehat{CDI}_\varepsilon$ (b) $\widehat{CDI}_{Ra}$ and (c) $\widehat{CDI}_{com}$ damage index maps when the crack was arrested at 'A', and (d) $\widehat{CDI}_\varepsilon$, (e) $\widehat{CDI}_{Ra}$ and (f) $\widehat{CDI}_{com}$ damage index map when the crack was arrested at 'D'. The x- and y- labels represent the number of subset columns and rows, respectively.

3.3.2 Crack path prediction algorithms

The future crack propagation paths were predicted using two approaches, i.e., the "highest intensity" and "confidence threshold" approach. The highest intensity approach predicts the future crack path by connecting the center of the subset having the highest intensity in each column of the damage index map while the "confidence threshold" approach assumes the crack most likely passes though the subsets whose damage index is above a confidence threshold.

The highest intensity approach is demonstrated in Fig. 17(a) using the $\widehat{CDI}_{com}$ map as an example. Nine columns of subsets in front of the crack pinning location 'A' are marked using a number and an arrow. The center of the subset having the highest intensity within each column is indicated by a black circle. The crack path is then predicted by connecting the marked center with a white solid

or dash line. Notice that the predicted crack path near the crack tip, as marked by the white solid line, only swings by a few subsets vertically. In contrast, the predicted crack path further away from the crack tip, as marked by the white dash line, swings widely. The vertical swing of the predicted crack path may indicate high prediction uncertainty, as discussed in the next paragraph. The "confidence threshold" approach is based on the statistic distribution of the damage index intensity in each column [54]. Assuming lognormal distribution, the subsets whose damage index is above a confidence threshold are assumed to contain the future crack path. As an example, the histogram of the $\widehat{CDI}_{com}$ distribution in columns #4 and #5 are plotted and fitted to a lognormal distribution, as shown in Fig. 17(b). The 90-percentile confidence threshold is marked on the plot and the number of subsets with intensities higher than the threshold are identified. The same procedure was applied to all columns and the $\widehat{CDI}_{com}$ map with 90-percentiele confidence is depicted in Fig. 17(c). The subsets with intensities below 90-percentile are filtered which appears as dark blue with zero intensity. Using the remaining subsets above the threshold, a prediction envelope can be defined, as marked by the white dash lines in Figure 17(c). For this purpose, the upper boundary of the envelope is generated by connecting the center of the upper edge of the top subsets. Similarly, the lower edge of the envelope is generated by connecting the center of the lower edge of the bottom subsets. Unlike the highest intensity approach, the crack path is expected to propagate within the prediction envelope instead of the center of the highest intensity subset. The prediction envelope might be discontinuous or have different branches, as in the case of column #4, #7 and #8 in Fig. 17(c). The implication of a discontinuous envelope is discussed in the next paragraph.
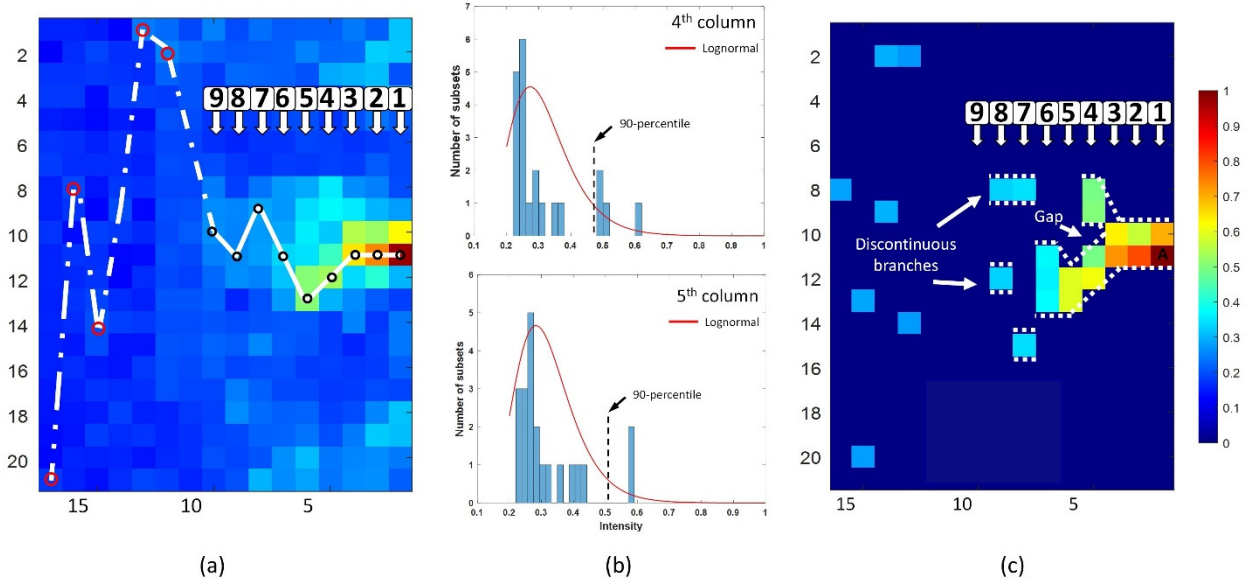
Fig. 17 (a) Predicted crack path based on the highest intensity approach using $\widehat{CDI}_{com}$, (b) histogram of subset intensity distribution in column 4 and 5 and their fittings to lognormal distribution and (c) subsets whose $\widehat{CDI}_{com}$ intensity is within the 90-percentile confidence threshold.

Using the highest intensity approach, the predicted propagation path by the three damage indices when the crack was pinned at 'A' are compared with the actual crack path in Fig. 18(a). The predicted paths based on $\widehat{CDI}_{\varepsilon}$, $\widehat{CDI}_{Ra}$ and $\widehat{CDI}_{com}$ are illustrated by dark blue, orange, and red dash lines, respectively. As discussed previously, the crack path predicted by $\widehat{CDI}_{com}$ has a small vertical swing before the 9th column but swings widely after. In comparison, the actual crack path, while meandering, does not deviate significantly from its path. Therefore, a wide swing of the predicted crack path further away from the crack tip indicates high prediction uncertainty. As such, only the prediction path constructed from the first 9 columns, i.e., 165 mm in front of the crack tip, are shown in Figure 18. The prediction by $\widehat{CDI}_{\varepsilon}$, represented by the blue dash line, barely matches with the actual crack path and swings around it. The prediction by $\widehat{CDI}_{Ra}$, represented by the orange line, matches with the actual crack path in the first four columns and then starts to deviate from the crack path and misses the crack turns thereafter. The prediction by $\widehat{CDI}_{com}$ map, represented by the red dash line, however, is closely matched with the actual crack path throughout

50

the first eight columns, but slightly deviates at the ninth columns. The prediction error may be contributed by the small branching at 'e'. To quantitatively evaluate the prediction accuracy, the distance from the center of the highest intensity subset to the actual crack path, measured in subset, are shown in Fig. 18(b). Since the damage index is calculated over a subset, the resolution of the prediction is therefore one subset, i.e., 18.3 μm. As shown in Figure 18(b), the prediction error by $\widehat{CDI}_\varepsilon$ could be as small as one subset, e.g., at Col. #1 or up to two subsets, e.g., at Col. #2. After the 4th column, the $\widehat{CDI}_\varepsilon$ prediction shows a close match with the actual crack path and the error reduces to less than one subset on average. The prediction error by $\widehat{CDI}_{Ra}$ in the first four columns are less than one subset. After the 4th column, i.e., 74 μm ahead of the crack tip, the prediction error may increase up to three subsets, e.g., at column #7 and #8. The crack path predicted by the $\widehat{CDI}_{com}$ deviates from the actual crack path by 1 subset or less with an average prediction error of 0.34 subsets for the first eight columns. At the ninth column, the prediction error is close to 2 subsets.

A similar analysis was performed when the crack was arrested at 'D', as shown in Figure 18(c) and 7(d). Since a small deviation was observed at the 10th column followed by a wide swing in the predicted path, the prediction is investigated up to 9 columns. The $\widehat{CDI}_\varepsilon$ prediction error can be as small as one subset but can reach a maximum of three subsets. The $\widehat{CDI}_{Ra}$ error is smaller than 0.5 subset in the first four columns, but the prediction error increases up to 2.2 subsets afterwards. Finally, the prediction by $\widehat{CDI}_{com}$ map shows a perfect match with the actual crack path throughout the nine columns. The average prediction error is as small as 0.12 subset, i.e., 2.1 μm. For both cases, $\widehat{CDI}_\varepsilon$ produces relatively large prediction errors. Furthermore, the prediction errors are not strongly correlated to the distance between the prediction location and the crack tip. $\widehat{CDI}_{Ra}$ has relatively small prediction errors at locations near the crack tip but the error increases at locations

that are further away from the crack tip. $\widehat{CDI}_{com}$, which combines $\widehat{CDI}_{\varepsilon}$ and $\widehat{CDI}_{Ra}$, produces the errors that are mostly within 1 subset. It also accurately predict the future crack path the furthest.
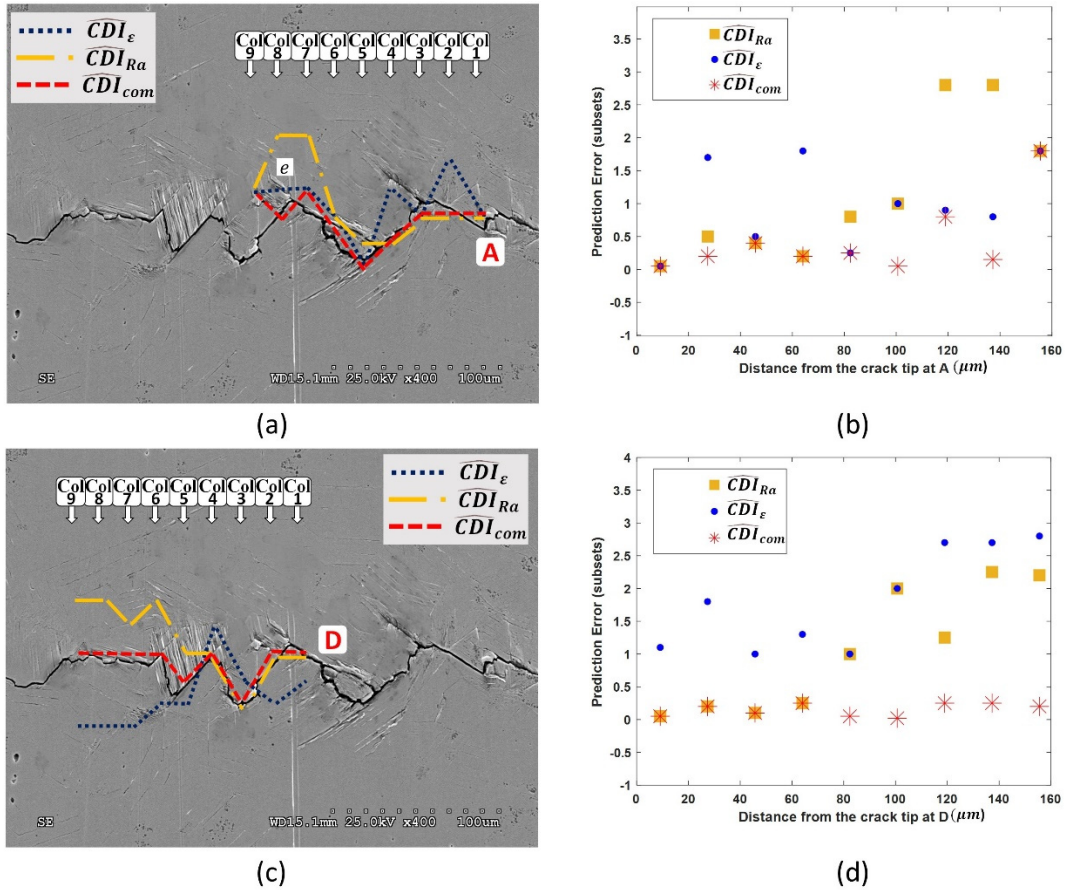
Fig. 18 Crack path prediction based on the highest intensity approach when the crack tip (a) arrested at 'A' and (b) the prediction error and when the crack tip was (c) arrested at 'D' and (d) the prediction error.

Using the confidence threshold approach, the crack path prediction envelopes by the three damage indices with 80, 90 and 95-percentile thresholds is illustrated in Fig. 19. The top row illustrates the prediction envelopes when the crack was arrested in 'A' and the bottom row is when the crack was arrested at 'D'.
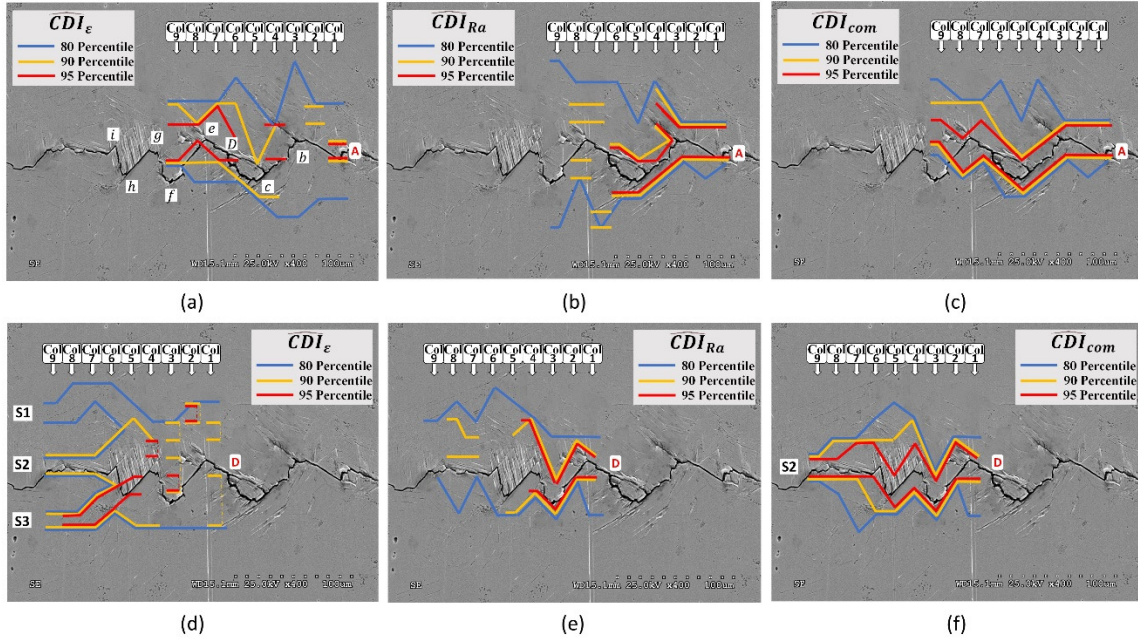
Fig. 19 (a) $\widehat{CDI}_\varepsilon$ (b) $\widehat{CDI}_{Ra}$ and (c) $\widehat{CDI}_{com}$ prediction envelopes with 80, 90 and 95-percentile confidence thresholds when the crack was arrested at 'A', and (d) $\widehat{CDI}_\varepsilon$, (e) $\widehat{CDI}_{Ra}$ and (f) $\widehat{CDI}_{com}$ prediction envelopes with 80, 90 and 95-percentile confidence thresholds when the crack was arrested at 'D'.

As expected, the 80-percentile threshold, represented by the blue lines, produces the largest envelope and thus the largest uncertainty in prediction. Although the 80-percentil envelope contains the actual crack path for all cases, it does not accurately predict the turns along the tortuous crack path. Increasing the confidence threshold to 90 or 95 percentile narrows down the prediction envelope but could lead to discontinuous envelope. For example, when the crack tip was arrested at 'A', the 90-percentile prediction envelope of $\widehat{CDI}_\varepsilon$ is discontinuous in the first three columns with inaccurate prediction in the 2nd column and no prediction in the 3rd column. From the 4th column, the 90-percentile $\widehat{CDI}_\varepsilon$ envelope enclosed the crack path and was able to predict the bend at 'c'. When the threshold is increased to 95-percentile, the $\widehat{CDI}_\varepsilon$ envelope fails to predict the crack path in the first five columns but accurately predicts the crack path, especially the bend, after the 5th column. On the other hand, the 90 and 95-percentile $\widehat{CDI}_{Ra}$ envelopes, shown in Fig. 19(b), provide an accurate prediction in the first five columns, i.e., near the crack tip, and captured

the crack branching at 'b' and subsequent bending at 'b' and 'c'. However, after the 5th column,

the 90-percentile $\widehat{CDI}_{Ra}$ envelope shows multiple prediction branches that deviate far from the

actual crack path. The 95-percentile $\widehat{CDI}_{Ra}$ envelope has no prediction at all. Compared to $\widehat{CDI}_{\varepsilon}$

and $\widehat{CDI}_{Ra}$, the 90 and 95-percentile thresholds of the $\widehat{CDI}_{com}$ produce remarkably enhanced

prediction in Fig. 19(c). The prediction envelopes narrow toward the actual crack path while

remain continuous throughout the entire eight columns, i.e., 148 μm. The crack path lies within

the prediction envelopes and the crack turns at 'b', 'c', and 'e' was perfectly predicted by the 95-

percentile confidence threshold. Similarly, when the crack was pinned at 'D', the 80-percentile

$\widehat{CDI}_{\varepsilon}$ map gives a wide envelope at the beginning, as shown in Figure 19(d). However, unlike Fig.

19(a), the prediction envelope branches into three directions, indicated by $S1$, $S2$ and $S3$, with

only S2 closely matching the actual crack path. The 90 and 95-percenitle $\widehat{CDI}_{\varepsilon}$ envelope show

multiple branches in the first four columns with significant inaccuracy and uncertainty. The 90-

percentile $\widehat{CDI}_{\varepsilon}$ envelope ends up with two branches at S2 and S3 with no further insight into the

most critical region between these spots. The 95-percentile $\widehat{CDI}_{\varepsilon}$ envelope converges to S3 which

is not the actual crack propagation path. Figure 19(d) indicates that $\widehat{CDI}_{\varepsilon}$ is not a suitable damage

index for crack path prediction. The $\widehat{CDI}_{Ra}$ prediction shown in Figure 19(e) demonstrate a similar

trend to that of Fig. 19(b), where the 90 and 95-percentile envelopes produce an accurate

estimation of the crack path up to the fifth column but show either inaccurate or lack of prediction

afterwards. Again, the $\widehat{CDI}_{com}$ map produces a remarkably improved prediction for all three

confidence thresholds, as shown in Figure 19(f). There is no discontinuity in the prediction

envelopes and even the 80-percentile envelope was able to predict the crack turn at 'e' and 'f'. The

90 and 95-percentile $\widehat{CDI}_{com}$ present a perfect prediction where the actual crack path does not fall

out of the envelope boundaries, i.e., no prediction uncertainty or inaccuracy is observed.

54

Interestingly, the 95-pecentile envelope was able to predict all the crack turns throughout the nine columns, i.e., 165 μm, at 'e', 'f', 'g', 'h', and 'i'. In addition, the prediction by all three confidence thresholds converged to the actual crack path at $S2$, providing a more reliable identification of the damage accumulation regions that the crack will likely propagate through. At both crack pinning locations, the combined damaged index, $\widehat{CDI}_{com}$, accurately predicted the tortuous crack path with sharp turns for an average of approximately 150 μm ahead of the crack tip. This is at least 60 μm longer than the best prediction provided by the surface roughness damage index in current study and that of reported in [54] for the same material. Even though the results for only two crack pinning locations are discussed, other pinning locations were analyzed and produced similar results and thus are not reported to avoid redundancy.

A few additional aspects worth discussing are:

Correlation with microstructure: despite numerous efforts by the fatigue community, the correlation between the microstructure and fatigue damage development remains to be unconclusive and under active research. In our recent study on a tensile polycrystalline sample [145], we observed a correlation between damage accumulation spots identified by the combined damage index and local microstructure, such as grain orientations that favor "sunken" deformation and large misorientation with neighbor grains. Since the microcrack front is affected by the local microstructure in the immediate vicinity [54], a comprehensive microstructure study in the future may shed lights on the correlation between the proposed combined damage index and microstructure.

Temporal resolution: fatigue crack growth is an intermittent phenomenon; the crack may be pinned at a location for an extended period and experience rapid growth upon releasing from the

pinning until it reaches the next pinning location. In this study, we studied crack path prediction at two pinning locations, i.e., 'A' and 'D'. The crack tip was pinned for 4,000 cycles a 'A' and the crack path was predicted 148 μm ahead of the crack tip. The crack tip was pinned for 6,000 cycles at 'D' and the prediction length was slightly improved to 165 μm. In general, the crack path near the crack tip can be predicted immediately when the crack is pinned. The crack path further away from the crack tip, however, may take some time for the surface topography change and plastic strain accumulation to intensify. The predictable crack length, therefore, depends on the pinning duration and the microstructures in front of the crack tip. For both cases, the crack lengths predicted are longer than the distances between the current and next pinning locations. Prediction error, such as that at the 9th column when crack tip is pinned at 'A', can be corrected at the next pinning location, i.e., at 'A'. As such, the entire crack path can be reliably predicted by tracking the combined DI at the pinning locations along the crack path. On the other hand, surface morphology changes also take place when the crack propagates between the pinning locations. The divergence behavior of the combined DI, as discussed in our previous research [40], may be able to account for damage development and accumulation during this transient state and thus may be used for crack path prediction without relying on crack pinning.

Out-of-plane shear strain: The surface roughness change which accounts for out-of-plane plastic deformation, is contributed by both normal and shear strains, i.e., ε_{zz}, ε_{xz} and ε_{yz}. However, it is not clear how these components contribute to the surface topography change individually. Calculating out-of-plane shear strain components ensures a more sophisticated damage index as well as providing insight into the mechanism of out-of-plane plastic deformation leading to crack initiation and propagation. Theoretically, the out-of-plane strain components may be calculated using the three displacement components as $\varepsilon_{zz} = \frac{\partial w}{\partial z}$, $\varepsilon_{xz} = (\frac{\partial w}{\partial x} + \frac{\partial u}{\partial z})$ and $\varepsilon_{yz} =$

$(\partial w/\partial y + \partial v/\partial z)$ where u, v and w are displacements along x, y and z direction, respectively, and ∂u, ∂v and ∂w represent the respective coordinate differences between two locations. However, since the displacement is measured on a highly polished surface, the ∂z value, i.e., the height difference between two points, is extremely small, leading to large error in out-of-plane strain calculation. The surface height difference required for a more accurate out-of-plane strain measurement and approaches to reduce error should be investigated in future studies.

3.4 Chapter summary

A combined effective plastic strain-surface roughness damage index is investigated for predicting the future propagation path of a microstructurally small crack in a nickel fatigue sample. A compound damage index map that accounts for the damage accumulation prior to and during the crack tip pinning period was constructed in front of the crack tip. Two prediction algorithms, based on the 'highest intensity subset' and the 'statistical confidence threshold', were developed. The combined damage index resulted in a significant enhancement in prediction accuracy, reliability and confidence compared to damage indices based on either the effective plastic strain or the surface roughness alone. The combined damage index predicted all the sharp turns in the tortuous crack path with highest accuracy and confidence, i.e., 95-percentile, for around 150 μm ahead of the crack pinning location, 60 μm longer than the best prediction by the surface roughness damage index. This study also concluded that the effective plastic strain is not a suitable damage index for predicting future crack path. The methodology presented in this chapter could enable future study on understanding different factors contributing to microcrack propagation, such as in-plane and out-of-plane deformations, strains, local microstructures, etc.

Chapter 4. Preliminary study of calculating out-of-plane shear strain components from surface height variation

4.1 Introduction

Various fatigue indicator parameters (FIPs) have been reported for fatigue damage identification in ductile materials. Most FIPs require all six stress/strain components. Some FIPs are particularly calculated using shear strain, e.g., Fatemi-Soci parameter, which accounts for maximum cyclic plastic shear strain. Since the out-of-plane strain components are difficult to measure experimentally, studies relied on simulation based on Crystal Plasticity Finite Element Method, CPFEM. However, due to imperfection in constitutive laws, lack of computation capacity, lack of knowledge of the microstructure underneath the surface and simplifications, the FE models cannot capture the material behavior faithfully and thus rarely have been verified experimentally.

The experiments have been focusing on plastic strain accumulation and surface morphology change to identify damage initiation and crack propagation in ductile materials. The grain scale strain accumulation has been investigated using Digital Image correlation based on high magnification optical interferometry or SEM. Using these techniques, the gain scale strain accumulation has been correlated with crack initiation sites [41, 72, 73, 160, 161], presence of voids [78], slip band formation [41, 42, 128, 158], and microstructure features such as grain misorientation [22, 76, 99] and Schmid factor [64, 66, 162]. However, these studies either focused on in-plane strain components and thus overlooked the out-of-plane plastic deformation or were merely concerned with out-of-plane features such as extrusion/intrusion height measurement and surface roughness change. Other optical techniques, such as 3D DIC using X-ray tomography and

stereovision DIC can measure both in-plane and out-of-plane deformation. Although these techniques have been successfully implemented to measure 3D strain components at the surface, there are limitations associated with high magnification measurements. These 3D techniques require at least two cameras to be calibrated and synchronized spatially at a certain angle with respect to the sample surface. For high magnification measurements, camera lenses need to be very close to the sample surface, imposed by the focal length. However, placing multiple cameras in a tight space may not be feasible. As such, these studies were performed in low resolution on materials with large single/oglio crystals or polycrystalline materials with relatively large grains. Additionally, the low magnification of these 3D techniques, may not be sufficient to capture plasticity induced surface roughness change which could be in order of tens of nanometers.

The proposed surface topography based Digital Image Correlation in previous chapters enables both in-plane and out of plane displacement measurement at the surface using one single optical lens. The 3D displacement values at the surface and their 3D coordinate can be used in theoretical strain-displacement relationship to calculate all six strain components. However, due to highly polished samples, the height difference between points is extremely small leading to large errors in out-of-plane shear strain calculation. In this chapter, we suggest a methodology that can be used in future studies to calculate a threshold value of height difference for error reduction associated with out-of-plane shear strain estimation. First, 2D strain/displacement calculation approach based on discrete differentiation, i.e., theoretical strain-displacement relationship, is compared with 2D FEM simulation. The verified 2D strain/displacement components can be later used in 3D strain-displacement relationship to calculate out-of-plane shear strain. However, the problematic height difference threshold value must be identified through 3D FEM simulation. A methodology for the 3D FEM approach will be suggested at the end of this chapter that can be used in future studies.

4.2 Methodology

Theoretically, if displacement and spatial coordinate of points are known, the 3D strain components can be calculated using the following set of equations:

Normal components
$$\varepsilon_x = \frac{\partial u}{\partial x}$$
$$\varepsilon_y = \frac{\partial v}{\partial y}$$
$$\varepsilon_z = \frac{\partial w}{\partial z}$$

Shear components
$$\gamma_{xy} = \left(\frac{\partial v}{\partial x} + \frac{\partial u}{\partial y}\right)$$
$$\gamma_{xz} = \left(\frac{\partial u}{\partial z} + \frac{\partial w}{\partial x}\right)$$
$$\gamma_{yz} = \left(\frac{\partial v}{\partial z} + \frac{\partial w}{\partial y}\right)$$

4.1

Where u, v and w are displacement in x, y and z direction, respectively and $\partial x, \partial y$ and ∂z are distance between the coordinates of wo locations. In the previous section, the proposed surface topography based DIC technique provided spatial coordinate of the correlation points at the surface along with its corresponding in-plane and out-of-plane displacement, i.e., height change. Thus, the in-plane normal and shear strain components, i.e., $\varepsilon_x, \varepsilon_y$ and γ_{xy}, have been readily calculated using the in-plane displacement and xy coordinate of the identified correlation points. The out-of-plane normal strain component, i.e., ε_z, has bee calculated based on plane stress assumption and plastic incompressibility, i.e., $\varepsilon_z = -(\varepsilon_x + \varepsilon_y)$. For calculating the out-of-plane shear strain components i.e., γ_{xz} and γ_{yz} using eq. 4.1, the in-plane displacement components, i.e., u, v and out-of-plane height variation, w, are already obtained by DIC. Additionally, the distance between two coordinates in xy plane has been already established using the grid network in previous chapters. The only problematic component is the height difference between two points, i.e., ∂z.

For highly polished samples, the height difference between adjacent points is extremely small leading to small denominator and thus large errors in strain calculation. As such, it is important to find a threshold value in height difference to achieve a more accurate estimation of out-of-plane shear strain. For this purpose, one approach is to employ Finite Element Method to study and verify this threshold value of height difference through simulation. A 3D FE model can provide all three displacement vectors and six strain components at each node. Then, using displacement components and their coordinate, the out-of-plane strain components can be calculated by eq. 4.1 and compared to the surface strain components directly obtained from FEM. By adjusting the height variation, i.e., surface roughness, a threshold value of height difference between two points that reduces error associated with out-of-plane shear strain calculation can be estimated. However, first the 2D strain calculated from discrete differentiation using strain-displacement relationships should be verified with FEM in the following section.

4.3 Finite Element Simulation

4.3.1 2D verification approach

A 2D FE simulation is performed to compare and validate the results directly obtained from FEM with those calculated by using eq. 4.1. Note that FEM calculates the nodal displacement which is subsequently used to calculate the strain distribution within elements through shape function interpolation. Since a node can be shared by different adjacent elements, the final strain value is the average of the nodal strains obtained from connected/neighbor elements. On the other hand, the displacement-strain relationship, i.e., eq. 4.1, calculates strain using the displacement derivative with respect to coordinates. When eq. 4.1 is applied to discrete points, two respective points must be aligned in the same direction that the partial derivative is performed, e.g., when

61

calculating $\partial u / \partial x$, the two points are aligned along the x direction. If the two points are not aligned in the same direction, a new point should be defined along the same direction and the displacement value at the defined point should be evaluated through interpolation. For this purpose, a grid network of points is defined over the region of interest, and the displacement values are mapped over the network to interpolate the displacement at grid points. Finally, the derivatives, i.e., eq. 4.1, are used to calculate the strain using the displacement at grid points. Since interpolation technique is an approximation in nature and depends on various factors such as number of data points, interpolation function, etc., it might add up to calculation error. Thus, it is imperative to validate the results in 2D and study the discrepancies between these two approaches, i.e., FEM and eq. 4.1, before extending to 3D analysis. In this chapter, we validate 2D analysis for two shapes of quad element, i.e., Perfect shape and skewed shape. A four-node linear quadrilateral element with perfect and skewed shape is illustrated in Fig. 21(a) and (b), respectively.

(a)   (b)
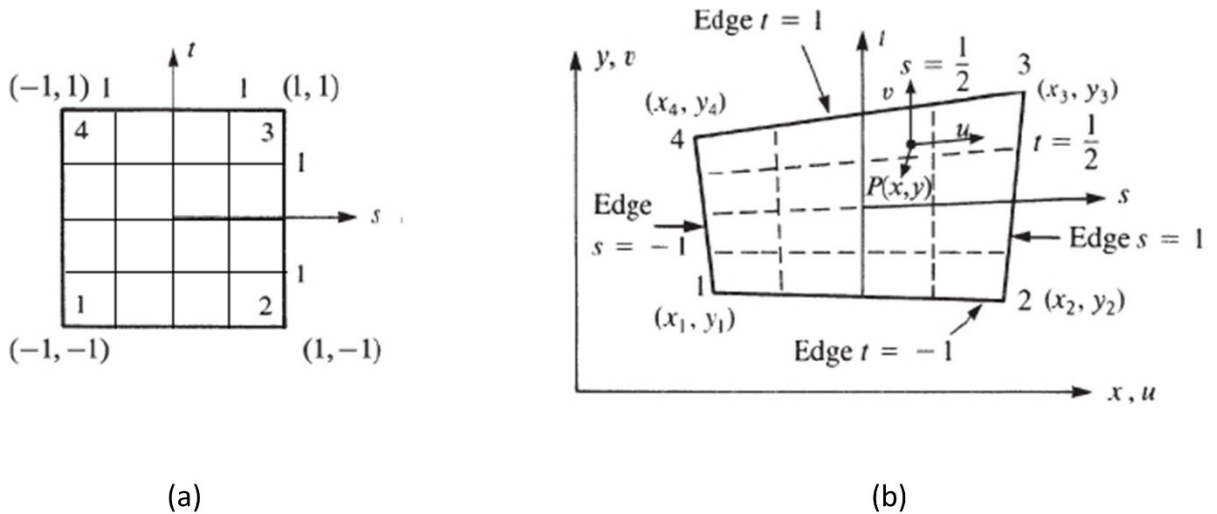
Fig. 20 A four-node linear quadrilateral element in isoparametric coordinate with (a) perfect and (b) skewed shape

The isoparametric FE shape functions are defined as follows:

$$N_1 = \frac{(1-s)(1-t)}{4} \qquad\qquad 4.2$$

62

$$N_2 = \frac{(1+s)(1-t)}{4}$$

$$N_3 = \frac{(1+s)(1+t)}{4}$$

$$N_4 = \frac{(1-s)(1+t)}{4}$$

Where s and t are local isoparametric coordinates. The 2D stress-strain relations in tensor form is

$$\begin{Bmatrix} \varepsilon_x \\ \varepsilon_y \\ \gamma_{xy} \end{Bmatrix} = \begin{Bmatrix} \dfrac{\partial u}{\partial x} \\[2mm] \dfrac{\partial v}{\partial y} \\[2mm] \dfrac{\partial u}{\partial y} + \dfrac{\partial v}{\partial x} \end{Bmatrix} \qquad 4.3$$

The following chain rule is applied to relate derivatives in local coordinate to global coordinate.

$$\frac{\partial ()}{\partial s} = \frac{\partial ()}{\partial x}\frac{\partial x}{\partial s} + \frac{\partial ()}{\partial y}\frac{\partial y}{\partial s}$$

$$\frac{\partial ()}{\partial t} = \frac{\partial ()}{\partial x}\frac{\partial x}{\partial t} + \frac{\partial ()}{\partial y}\frac{\partial y}{\partial t}$$

$$4.4$$

Thus, the strain-displacement in global coordinate takes the following form:

$$\begin{Bmatrix} \varepsilon_x \\ \varepsilon_y \\ \gamma_{xy} \end{Bmatrix} = \frac{1}{|J|} \begin{bmatrix} \dfrac{\partial y}{\partial t}\dfrac{\partial ()}{\partial s} - \dfrac{\partial y}{\partial s}\dfrac{\partial ()}{\partial t} & 0 \\[3mm] 0 & \dfrac{\partial x}{\partial s}\dfrac{\partial ()}{\partial t} - \dfrac{\partial x}{\partial t}\dfrac{\partial ()}{\partial s} \\[3mm] \dfrac{\partial x}{\partial s}\dfrac{\partial ()}{\partial t} - \dfrac{\partial x}{\partial t}\dfrac{\partial ()}{\partial s} & \dfrac{\partial y}{\partial t}\dfrac{\partial ()}{\partial s} - \dfrac{\partial y}{\partial s}\dfrac{\partial ()}{\partial t} \end{bmatrix} \begin{Bmatrix} u \\ v \end{Bmatrix} \qquad 4.5$$

Where, J, is the Jacobian matrix that accounts for the transformation from local isoparametric coordinate to global coordinate and element size and shape distortion. Based on the isoparametric element description, the global ε_x strain is then calculated by

$$\varepsilon_x = \frac{1}{|J|} \left(\frac{\partial y}{\partial t}\frac{\partial u}{\partial s} - \frac{\partial y}{\partial s}\frac{\partial u}{\partial t} \right) \qquad 4.6$$

63

This equation is further investigated for perfect shape and skewed shape elements.

4.3.2.1 Perfect shape element

In a perfect shape quadrilateral element, i.e., Fig. 21(a), the second term is zero and the equation takes the final form as

$$\varepsilon_x = \frac{1}{|J|} \left(\frac{\partial y}{\partial t} \frac{\partial u}{\partial s} \right) \qquad\qquad 4.7$$

For a perfect shape quad element, the Jacobian determinant will be a scalar. Note that eq. 4.8 is the interpolation function used by FEM to calculate the nodal strain. The nodal displacement values are also used in eq. 4.1 to obtain the strain values which will be compared with FEM results.

4.3.2.2 Skewed shape element

In a skewed shape element, the determinant of the Jacobian matrix is not necessarily a scalar and may be a function of local coordinates, s and t. Additionally, the second term, i.e., $\frac{\partial y}{\partial s} \frac{\partial u}{\partial t}$, is nonzero and has a significant contribution to the strain calculation. Thus, ε_x remains as complete as:

$$\varepsilon_x = \frac{1}{|J|} \left(\frac{\partial y}{\partial t} \frac{\partial u}{\partial s} - \frac{\partial y}{\partial s} \frac{\partial u}{\partial t} \right) \qquad\qquad 4.8$$

Regardless of the element shape, in a 2D four-node quadrilateral element, each corner node could be shared by four elements and therefore its strain value will be an average of interpolations in those four elements. If a node is placed in the middle of one edge, then its strain value will be the average of the interpolations in two adjacent elements sharing that boundary/edge.

4.3.3 2D Result

A 2D rectangular model with perfectly shaped quadrilateral elements has been generated in ABAQUS as shown in Fig. 22(a). The enlarged view in Fig. 22(b) shows an element with its nodes being numbered counter-clockwise and the displacement vectors demonstrated at each node. The FEM calculates the strains at nodes through the shape function interpolation using eq. 4.7. The whole model was subjected to a tensile load along x direction and ε_x strain distribution is depicted in Fig. 23. The nodal x-displacement obtained by FEM, , i.e., u, is used in strain-displacement relationship in eq. 4.1, i.e., $\partial u/\partial x$. The discrete derivation is performed by dividing the displacement difference to the distance between two nodes, e.g., $(u_3 - u_4)/\Delta l$, where Δl_x is the length of the element in x direction.

(a)   (b)
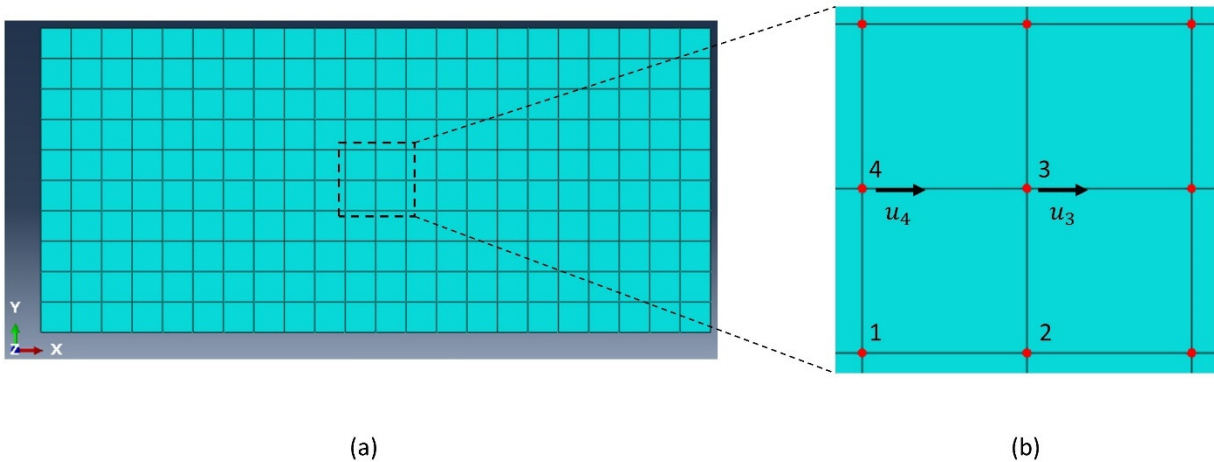
Fig. 21 (a) A 2D rectangular model with perfectly shaped quad elements, (b) magnified view of a few elements.

The nodal strain values obtained from these two approaches, i.e., FEM and direct derivative method, are compared and the difference is 1.2% on average with a maximum error of 1.56%.
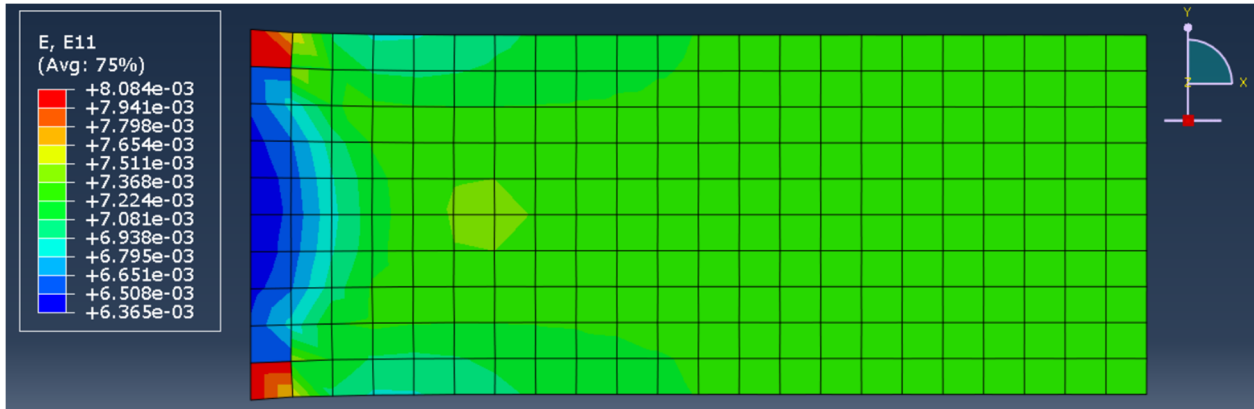
Fig. 22 ε_x strain distribution in the FE model of a rectangular with perfect shape quad elements

A second FEM model is generated with skewed quadrilateral elements as shown in Fig. 24(a) with a magnified view of a few elements in Fig. 24(b). The FEM nodal strains are obtained by shape function interpolation using eq. 4.8. However, since the nodal points are not aligned in x-direction, i.e., the element is skewed, eq. 4.1 cannot be directly applied to calculate the strain, e.g., $(u_3 - u_4)/\Delta l$ is not valid. As such, an interpolation procedure has been followed using which displacement values are mapped over a grid network and interpolated at grid points. The interpolated displacement values are then used in eq. 4.1 to calculate strain at each grid point.

(a)   (b)
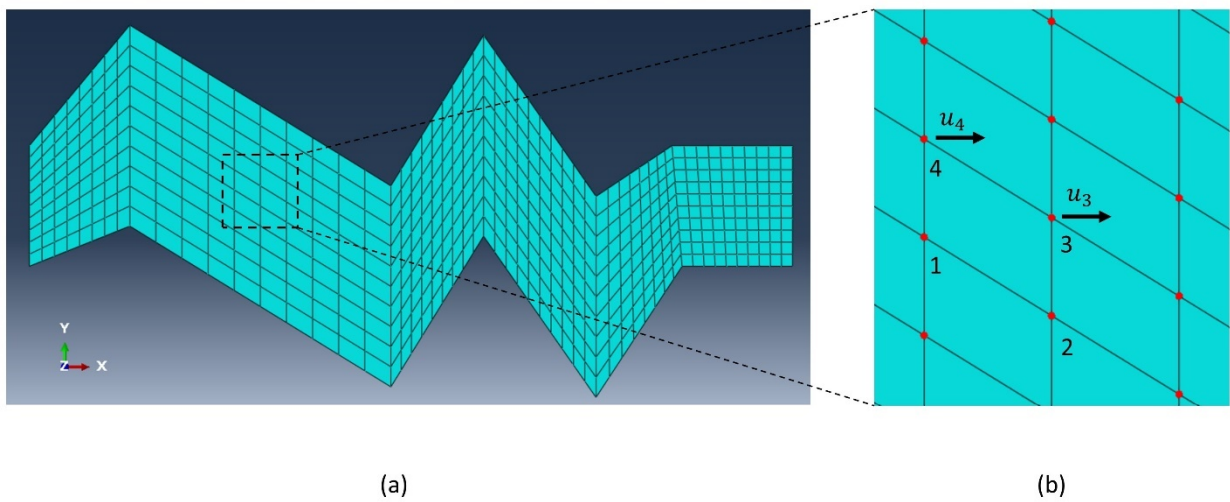
Fig. 23 (a) FEM model with skewed shape quad elements and (b) magnified view of a few elements.

66

The model has been subjected to tensile load and Fig. 25 shows an example of strain distribution along x-direction. Fig. 26(a) depicts a section of the FE model with a grid network mapped over the nodal points and Fig. 26(b) shows an enlarged view of four elements within the mapped region. The FEM nodes are marked by red points while the grid network is indicated by white points. Again, the corner nodes are shared with four elements, e.g., node #2, and each edge is shared between two elements. However, the grid points can be located anywhere within the elements depending on the size of the data set and increments. Using first approach, i.e., the FEM method, the strain values at the middle of the right edge in element #1, is calculated based on the local st-coordinate and then transferred into the global domain using Jacobian and isoparametric transformation. Since this location is shared with a neighbor element, the same calculation is performed for the second element and the two strain values are averaged. Using the second approach, i.e., derivatives in eq. 4.1, to estimate the stain at the middle of the edge, first a grid point must be defined at that exact location. Then, the displacement is interpolated at this and other grid points along the x-direction. The displacement and coordinate of two consecutive grid point is then used in eq. 4.1 to obtain ε_x. In Fig. 26(b) a gird point has been carefully defined at the middle of the edge. Using the interpolated value of displacement at this location, u_g3, and another proceeding/preceding location along the x-direction, e.g., u_g2, and having the distance between their coordinates, i.e., ΔL_g, the strain value is calculated using eq. 4.1, i.e., $(u_g3 - u_g2)/\Delta L_g$.
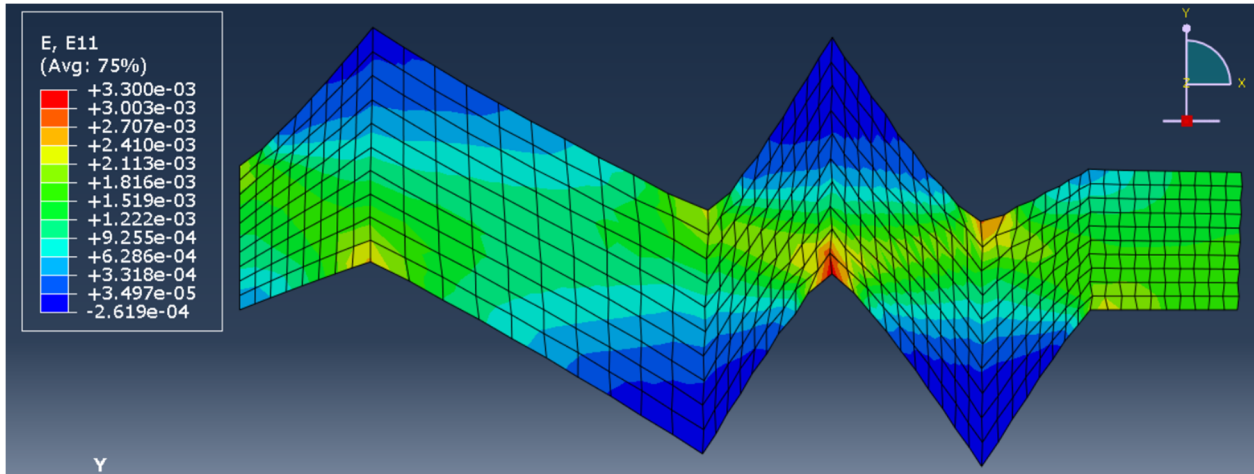
Fig. 24 ε_x strain distribution in a 2D model with skewed shape quadrilateral elements

| (a) | (b) |
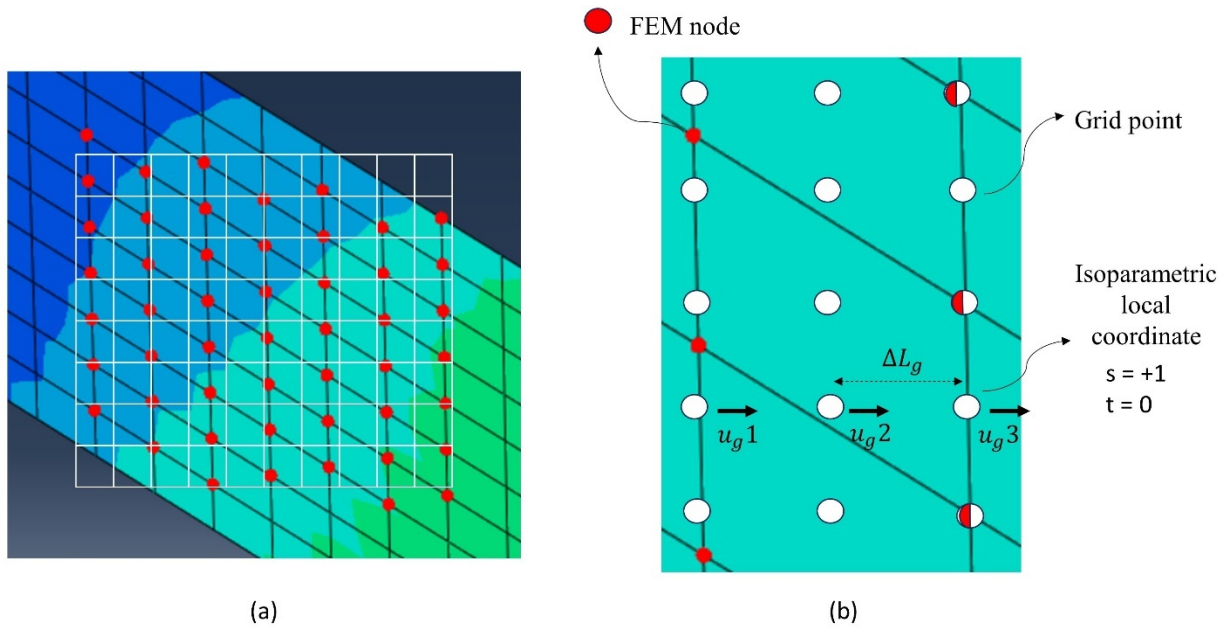
Fig. 25 (a) Grid network mapped over the nodal points for displacement interpolation (b) enlarged view of FEM nodes and grid points within the elements

Using FEM, the strain at all grid points has been evaluated through interpolation based on shape function and local st-coordinates of grid points. Similarly, the interpolated displacement values at all grid points have been directly used in eq. 4.1 for strain calculation. ε_x results have been compared and the difference between the two methods is reduced to 14.2% for the current model with a maximum error of 17.6%. Multiple factors might contribute to the observed discrepancy

between two approaches. First, the FEM uses shape functions and interpolation to calculate the strain distribution within each element including edge nodes. The same calculation is performed in each neighbor element that shares the same node/edge. The nodal strain values calculated by all elements are then averaged and presented as the final strain value at the target node. As the skewness of the elements increases, the strain calculated in an element might be significantly different to that of calculated in a neighbor element sharing the same node. Thus, the error in averaging increases significantly. There is also some error associated with the second approach, i.e., discrete differentiation. Since a grid point network is mapped over the nodal points, the number of nodes, grid point increment, and parameters of interpolation function affects the accuracy of the interpolation. One way to improve the results is generating an FEM model with finer mesh which results in a larger number of nodes. This allows increasing the number of points in the grid network, i.e., reducing the increments, for obtaining an enhanced displacement interpolation at grid points.

The verified 2D strain/displacement calculation approach using discrete points can be extended to 3D strain-displacement relationship in eq. 4.1. However, the last hurdle is the height difference, i.e., ∂z. To resolve the issue, we suggest using a 3D FE model which will be discussed in the following.

4.3.4 Proposed 3D FE approach

For estimating a threshold value for height difference to reduce the error associated with the out-of-plane shear strain calculation using eq. 4.1, a 3D FE model should be investigated. First, A 3D Finite Element model with predefined surface roughness is generated in ABAQUS. The surface

roughness was generated using the following MATLAB function based on Weibull distribution [163]:

function [**Nodes,Elements**]=**Rand_surf**(Lx,Ly,Lz,N,sn_x,sn_y,WB_a,WB_b)   4.2

Where Lx, Ly are the length in x and y direction, and Lz is the thickness in z direction. Sn_x and Sn_y are the sampling points in x and y direction, respectively. N is the number of divisions between sampling points which controls the mesh size. WB_a and WB_b are the Weibull distribution parameters which control the height variation frequency (Smoothness/roughness of the surface) and height values. Refer to Appendix. A for more details on the generated MATLAB function. Fig. 20(a) shows the sampling and nodal points mapped over the surface and Fig. 20(b) depicts a generated FE model in ABAQUS with rough surface.

(a)   (b)
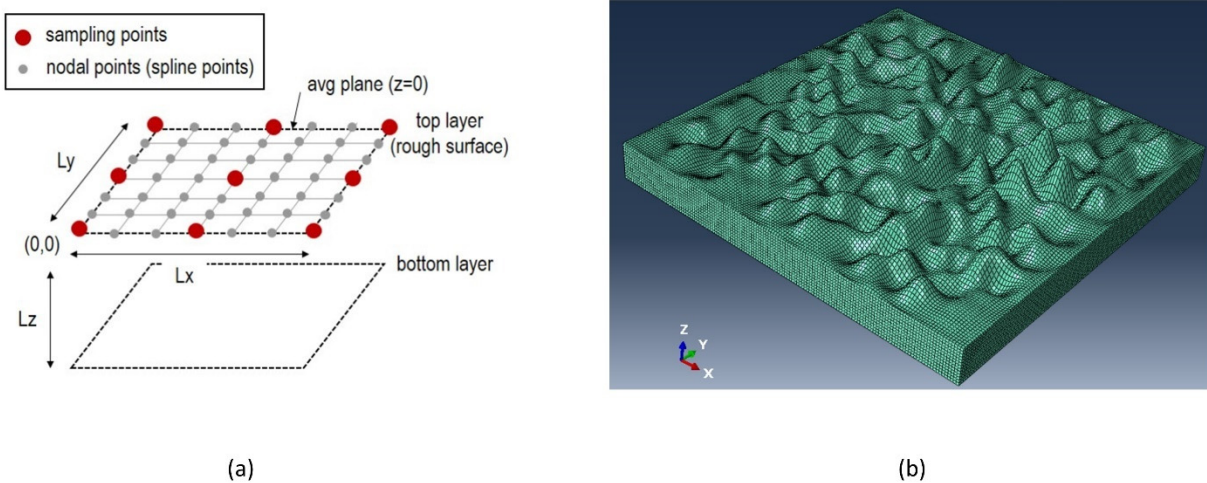
Fig. 26 Sampling point and rough layer generation (b) Rough surface generated in ABAQUS

The 3D displacement values at surface nodes can be calculated using the 3D model shown in Fig. 26(b). Using the surface nodal displacement values, the out-of-plane normal and shear strain components should be calculated using eq. 4.1. In this equation, u, v and w are the surface displacement values already obtained from FEM model. $\partial x, \partial y$ and ∂z are surface coordinate

differences measured using the coordinate of the surface nodes that will be available in FEM nodal

output. Thus, all the required components, including the height difference, i.e., ∂z, in eq. 4.1 is

available to estimate the out-of-plane shear strain component from the surface nodes only. This

estimated value should be compared with the actual shear strain value obtained directly from 3D

FEM simulation. To reduce the error in calculating out-of-plane shear strain, multiple FE models

with various surface roughness should be generated and various height difference, i.e., ∂z, values

should be tested. The out-of-plane shear strain values should be then compared with the actual

shear strains directly obtained from FEM and a threshold height difference value that minimizes

the error in out-of-plane shear strain estimation can be proposed. Fig. 27 shows the flowchart of

the procedure. This threshold of height difference, i.e., surface roughness, will be produced in an

experimental sample to calculate all six strain components at surface using surface displacement

and height variation.
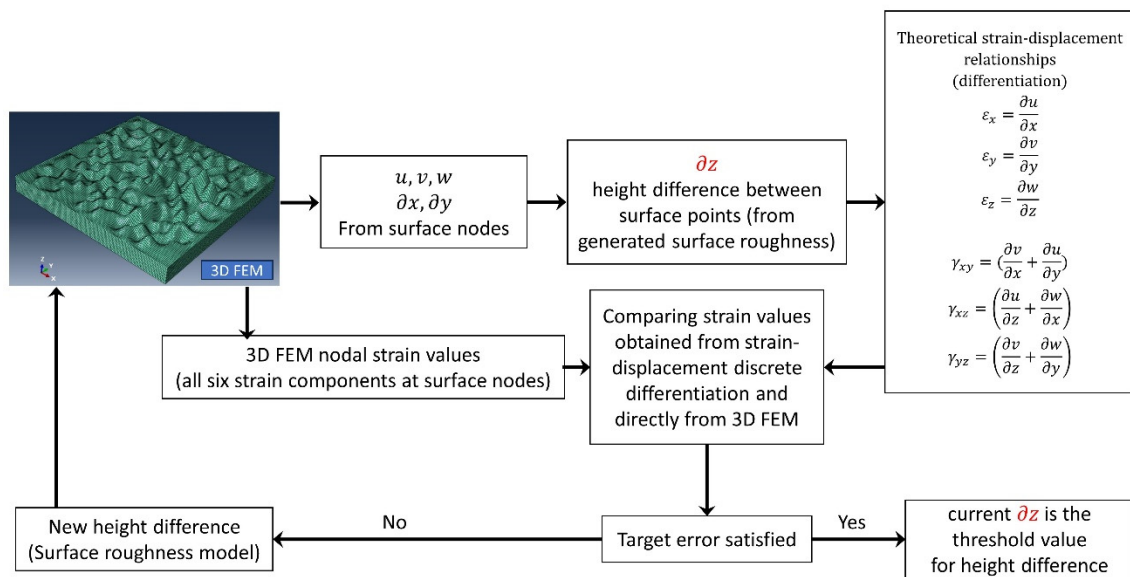
Fig. 27 Flowchart of the procedure to find the threshold value for minimum surface height difference for out-of-plane shear strain calculation

4.5 Summary

In this chapter, 2D strain values obtained from theoretical strain-displacement relationships are compared with the strain values directly obtained from FEM simulation for 2D perfect and skewed shape quadrilateral elements. The strain-displacement relationship allows for discrete partial differentiation based on displacement components and distance between the coordinate of points. Using FEM, the nodal strain was calculated through the isoparametric shape function interpolation. The strain values obtained by conventional strain-displacement relationships have been compared to FEM to verify the results in 2D. The verified strain calculation approach can be used in 3D strain calculation using theoretical equations. A the end of the chapter, a 3D FEM approach is suggested to calculate a threshold value for surface height difference to reduce errors associated with calculating out-of-plane shear strain using surface nodal displacement.

Chapter.5 Conclusion Remarks and future works

5.1 Conclusion remarks

In this study, a surface topography based Digital Image Correlation (DIC) technique is proposed using high resolution optical microscope interferometry. The proposed DIC technique enables calculating both in-plane and out-of-plane deformation at the surface. An optical microscope interferometer was integrated with mechanical tester to acquire surface topography images during the experiment. In order to measure the surface topography, the speckle layer that is used for DIC analysis must be reflective under the microscope. A cost-effective speckle pattern creation technique was proposed that produced high density, randomly distributed, reflective and micro-size speckles suitable for sub-grain strain analysis. Combining the effective plastic strain obtained from DIC and surface roughness change calculated from topography change, a damage index is proposed for identifying damage accumulation and crack growth in polycrystalline Nickel. The experiment is conducted for two samples, a standard tensile sample, and a standard middle tension fatigue sample.

Tensile Sample

The standard tensile sample was subjected to a tensile load starting below the yield point and incrementally increased beyond the yield point into the plastic region. A region of interest (ROI) was defined in the middle of the gage section. At each step, the sample was unloaded, and surface topography images of the ROI were captured. The Surface roughness, strain, and combined damage index maps were constructed within the ROI and were compared in terms of damage localization and localization consistency. It was found that:

- The combined index showed enhanced damage localization and localization consistency in identifying damage accumulation sites compared to damage indices based on either effective plastic strain or surface roughness change

- The identified damage accumulation sites were corelated to microstructure that favor sinking deformation of grains and large misorientation between neighbor grains

Fatigue sample

A middle tension fatigue sample was designed and subjected to tensile cyclic load to initiate a crack in front of the notch tip. The test was stopped at predefined fatigue intervals and the surface topography images were acquired using the optical microscope. The combined effective plastic strain and surface roughness damage index was investigated to predict the future propagation path of a micro-crack in front of the notch tip. Effective plastic strain, surface roughness and combined damage index maps were constructed during the crack pinning period. The three indices are compared in terms of prediction accuracy and confidence. It was found that:

- The effective plastic strain provided the least accuracy and showed a poor prediction of the crack path.

- The predicted path by the surface roughness index was significantly enhanced in areas close the crack tip and the predicted path matched the actual crack path for up to $90 \; \mu m$ in front of the crack pinning location.

- The combined index provided the most accurate prediction compared to the other two DIs and the predicted path perfectly matched the actual crack path for an average length of $150 \; \mu m$ ahead of the crack tip arresting location. This was at least $60 \; \mu m$ more than the best prediction by the surface roughness index.

- The combined index predicted the crack path with the highest confidence of 95-percentile without any uncertainty or discontinuity throughout the prediction length.

Finally, a preliminary study was conducted for calculating the out-of-plane shear strain based on theoretical strain-displacement relationships. To reduce the error in out-of-plane strain calculation due to small height difference in highly polished samples, FEM simulation was proposed to investigate a threshold for the minimum height difference. In this preliminary study, strain components calculated from strain-displacement relationship are first verified in 2D by analyzing a 2D finite element model with perfect and skewed shape quadrilateral elements. The verified 2D technique can be used in 3D strain-displacement relationships to calculate out-of-plane shear strain components. A 3D FEM approach is suggested to calculate the threshold value for height difference that is expected to reduce error in out-of-plane shear strain calculation.

5.2 Suggestion for future work

Using the proposed novel DIC technique based on surface topography images and the proposed combined effective plastic strain-surface roughness change damage index, some future works are suggested:

- Since the surface topography images were captured by a $50x$ magnification optical lens, it is suggested that higher magnification lenses can be used to study surface morphological change in a smaller region with higher resolution.
- Instead of analyzing a single image in tensile specimen that covers a small region, the damage index map can be constructed over the entire RIO in the gage section to study the evolution of damage accumulation sites and identify the most critical region that leads to actual crack initiation.

75

- The combined index can be investigated for identifying crack initiation in a fatigue sample.

- The correlation between the microstructure features and crack initiation/propagation regions identified by the combined damage index can be studied.

- In this study, the damage index map was constructed when the crack tip was pinned. In future studies, damage index maps can be constructed in transient state between two pinning locations to capture the strain accumulation and surface morphology change between two pinning locations.

- The FEM simulation should be extended to 3D to investigate the minimum surface height difference required to reduce the error in out-of-plane strain calculation.

- Using the calculated out-of-plane shear strain based on the proposed height difference threshold, the effective plastic strain can be calculated using all six strain components. The calculated effective plastic strain can then be compared to the combine damage index in terms of accuracy, efficiency and confidence in identifying damage accumulation sites.

Chapter.6 References

1. Suresh S (1998) Fatigue of materials. Cambridge university press

2. Zhu L, Wu ZR, Hu XT, Song YD (2016) Investigation of small fatigue crack initiation and growth behaviour of nickel base superalloy GH4169. Fatigue Fract Eng Mater Struct 39:1150–1160

3. Krupp U (2007) Fatigue crack propagation in metals and alloys: microstructural aspects and modelling concepts. Wiley Online Library

4. Boeff M, ul Hassan H, Hartmaier A (2017) Micromechanical modeling of fatigue crack initiation in polycrystals. J Mater Res 32:4375–4386

5. Raabe D, Sachtleber M, Zhao Z, et al (2001) Micromechanical and macromechanical effects in grain scale polycrystal plasticity experimentation and simulation. Acta Mater. https://doi.org/10.1016/S1359-6454(01)00242-7

6. Hochhalter JD, Littlewood DJ, Christ RJ, et al (2010) A geometric approach to modeling microstructurally small fatigue crack formation: II. Physically based modeling of microstructure-dependent slip localization and actuation of the crack nucleation mechanism in AA 7075-T651. Model Simul Mater Sci Eng 18:. https://doi.org/10.1088/0965-0393/18/4/045004

7. Wan VVC, MacLachlan DW, Dunne FPE (2016) Integrated experiment and modelling of microstructurally-sensitive crack growth. Int J Fatigue 91:110–123

8. Zurek AK, James MR, Morris WL (1983) The effect of grain size on fatigue growth of short cracks. Metall Trans A 14:1697–1705

9. Sangid MD (2013) The physics of fatigue crack initiation. Int J Fatigue 57:58–72. https://doi.org/10.1016/j.ijfatigue.2012.10.009

10. Mughrabi H (2009) Cyclic slip irreversibilities and the evolution of fatigue damage. Metall Mater Trans B 40:431–453

11. Mughbrabi H, Ackermann FU, Herz K, Fong JT (1979) Persistent slipbands in fatigued face-centered and body-centered cubic metals. ASTM International

12. Musinski WD, McDowell DL (2016) Simulating the effect of grain boundaries on microstructurally small fatigue crack growth from a focused ion beam notch through a three-dimensional array of grains. Acta Mater 112:20–39. https://doi.org/10.1016/j.actamat.2016.04.006

13. Proudhon H, Li J, Ludwig W, et al (2017) Simulation of Short Fatigue Crack Propagation in a 3D Experimental Microstructure. Adv Eng Mater 19:. https://doi.org/10.1002/adem.201600721

14. Manonukul A, Dunne FPE (2004) High- and low-cycle fatigue crack initiation using polycrystal plasticity. Proc R Soc A Math Phys Eng Sci 460:1881–1903. https://doi.org/10.1098/rspa.2003.1258

15. Briffod F, Shiraiwa T, Enoki M (2020) Nucleation and propagation modeling of short fatigue crack in rolled bi-modal Ti–6Al–4V alloy. Mater Sci Eng A 790:.

https://doi.org/10.1016/j.msea.2020.139710

16.   Sperry R, Harte A, Quinta da Fonseca J, et al (2020) Slip band characteristics in the presence of grain boundaries in nickel-based superalloy. Acta Mater 193:229–238. https://doi.org/10.1016/j.actamat.2020.04.037

17.   Karolczuk A, Skibicki D, Pejkowski Ł (2019) Evaluation of the Fatemi-Socie damage parameter for the fatigue life calculation with application of the Chaboche plasticity model. Fatigue Fract Eng Mater Struct 42:197–208. https://doi.org/10.1111/ffe.12895

18.   Zhang X, Stinville JC, Pollock TM, Dunne FPE (2021) Crystallography and elastic anisotropy in fatigue crack nucleation at nickel alloy twin boundaries. J Mech Phys Solids 155:104538. https://doi.org/10.1016/j.jmps.2021.104538

19.   Wan VVC, Maclachlan DW, Dunne FPE (2014) A stored energy criterion for fatigue crack nucleation in polycrystals. Int J Fatigue 68:90–102. https://doi.org/10.1016/j.ijfatigue.2014.06.001

20.   Zhang J, Johnston J, Chattopadhyay A (2014) Physics-based multiscale damage criterion for fatigue crack prediction in aluminium alloy. Fatigue Fract Eng Mater Struct 37:119–131. https://doi.org/10.1111/ffe.12090

21.   Bandyopadhyay R, Prithivirajan V, Peralta AD, Sangid MD (2020) Microstructure-sensitive critical plastic strain energy density criterion for fatigue life prediction across various loading regimes. Proc R Soc A Math Phys Eng Sci 476:. https://doi.org/10.1098/rspa.2019.0766

22.   Chen B, Jiang J, Dunne FPE (2017) Microstructurally-sensitive fatigue crack nucleation in Ni-based single and oligo crystals. J Mech Phys Solids 106:15–33. https://doi.org/10.1016/j.jmps.2017.05.012

23.   Korsunsky AM, Dini D, Dunne FPE, Walsh MJ (2007) Comparative assessment of dissipated energy and other fatigue criteria. Int J Fatigue 29:1990–1995. https://doi.org/10.1016/j.ijfatigue.2007.01.007

24.   Castelluccio GM, McDowell DL (2015) Microstructure-sensitive small fatigue crack growth assessment: Effect of strain ratio, multiaxial strain state, and geometric discontinuities. Int J Fatigue 82:521–529. https://doi.org/10.1016/j.ijfatigue.2015.09.007

25.   Düber O, Künkler B, Krupp U, et al (2006) Experimental characterization and two-dimensional simulation of short-crack propagation in an austenitic–ferritic duplex steel. Int J Fatigue 28:983–992

26.   Krupp U, Alvarez-Armas I (2014) Short fatigue crack propagation during low-cycle, high cycle and very-high-cycle fatigue of duplex steel–An unified approach. Int J Fatigue 65:78–85

27.   Owolabi GM, Whitworth HA (2014) Modeling and simulation of microstructurally small crack formation and growth in notched nickel-base superalloy component. J Mater Sci Technol 30:203–212. https://doi.org/10.1016/j.jmst.2013.09.011

28.   Kobayashi S, Inomata T, Kobayashi H, et al (2008) Effects of grain boundary-and triple junction-character on intergranular fatigue crack nucleation in polycrystalline aluminum. J Mater Sci 43:3792–3799

29.   Larrouy B, Villechaise P, Cormier J, Berteaux O (2015) Grain boundary–slip bands interactions: Impact on the fatigue crack initiation in a polycrystalline forged Ni-based superalloy. Acta Mater 99:325–336

30.   Vehoff H, Nykyforchyn A, Metz R (2004) Fatigue crack nucleation at interfaces. Mater Sci Eng A 387:546–551

31.   Schaef W, Marx M, Vehoff H, et al (2011) A 3-D view on the mechanisms of short fatigue cracks interacting with grain boundaries. Acta Mater 59:1849–1861

32.   Peralta P, Dickerson R, Dellan N, et al (2005) Effects of local grain orientation on fatigue crack growth in multicrystalline fcc metallic materials. J Eng Mater Technol 127:23–32

33.   Miao J, Pollock TM, Jones JW (2012) Microstructural extremes and the transition from fatigue crack initiation to small crack growth in a polycrystalline nickel-base superalloy. Acta Mater 60:2840–2854

34.   Sangid MD (2013) The physics of fatigue crack initiation. Int J Fatigue 57:58–72

35.   Ludwig W, Buffière J-Y, Savelli S, Cloetens P (2003) Study of the interaction of a short fatigue crack with grain boundaries in a cast Al alloy using X-ray microtomography. Acta Mater 51:585–598

36.   El Bartali A, Aubin V, Degallaix S (2008) Fatigue damage analysis in a duplex stainless steel by digital image correlation technique. Fatigue Fract Eng Mater Struct 31:137–151. https://doi.org/10.1111/j.1460-2695.2007.01207.x

37.   Rannou J, Limodin N, Réthoré J, et al (2010) Three dimensional experimental and numerical multiscale analysis of a fatigue crack. Comput Methods Appl Mech Eng 199:1307–1325

38.   Birosca S, Buffiere JY, Garcia-Pastor FA, et al (2009) Three-dimensional characterization of fatigue cracks in Ti-6246 using X-ray tomography and electron backscatter diffraction. Acta Mater 57:5834–5847

39.   Birosca S, Buffiere J-Y, Garcia-Pastor FA, et al (2010) Three-dimensional characterization of fatigue cracks in Ti-6246 using X-ray tomography and electron backscatter diffraction (vol 57, pg 5834, 2009). Acta Mater 58:1466

40.   Efthymiadis P, Pinna C, Yates JR (2019) Fatigue crack initiation in AA2024: A coupled micromechanical testing and crystal plasticity study. Fatigue Fract Eng Mater Struct 42:321–338

41.   Carroll J, Abuzaid W, Lambros J, Sehitoglu H (2010) An experimental methodology to relate local strain to microstructural texture. Rev Sci Instrum 81:. https://doi.org/10.1063/1.3474902

42.   Abuzaid WZ, Sangid MD, Carroll JD, et al (2012) Slip transfer and plastic strain accumulation across grain boundaries in Hastelloy X. J Mech Phys Solids 60:1201–1220. https://doi.org/10.1016/j.jmps.2012.02.001

43.   Abuzaid W, Sehitoglu H, Lambros J (2013) Plastic strain localization and fatigue micro-crack formation in Hastelloy X. Mater Sci Eng A 561:507–519. https://doi.org/10.1016/j.msea.2012.10.072

44.   Ho HS, Risbet M, Feaugas X, et al (2018) Surface roughness based characterization of slip band for damage initiation in a nickel base superalloy. Medziagotyra.

https://doi.org/10.5755/j01.ms.24.1.17684

45. Risbet M, Feaugas X, Guillemer-Neel C, Clavel M (2003) Use of atomic force microscopy to quantify slip irreversibility in a nickel-base superalloy. Scr Mater 49:533–538. https://doi.org/10.1016/S1359-6462(03)00357-9

46. Risbet M, Feaugas X (2008) Some comments about fatigue crack initiation in relation to cyclic slip irreversibility. Eng Fract Mech 75:3511–3519

47. Stoudt MR, Levine LE, Creuziger A, Hubbard JB (2011) The fundamental relationships between grain orientation, deformation-induced surface roughness and strain localization in an aluminum alloy. Mater Sci Eng A 530:107–116

48. Wang Y, Meletis EI, Huang H (2013) Quantitative study of surface roughness evolution during low-cycle fatigue of 316L stainless steel using Scanning Whitelight Interferometric (SWLI) Microscopy. Int J Fatigue 48:280–288

49. Muravsky LI, Picart P, Kmet' AB, et al (2016) Evaluation of fatigue process zone dimensions in notched specimens by two-step phase shifting interferometry technique. Opt Eng 55:104108

50. Vladimirov AP, Kamantsev IS, Veselova VE, et al (2016) Use of dynamic speckle interferometry for contactless diagnostics of fatigue crack initiation and determining its growth rate. Tech Phys 61:563–568. https://doi.org/10.1134/S106378421604023X

51. Jha DK, Singh DS, Gupta S, Ray A (2012) Fractal analysis of crack initiation in polycrystalline alloys using surface interferometry. Epl 98:. https://doi.org/10.1209/0295-5075/98/44006

52. Haghshenas A, Khonsari MM (2018) Damage accumulation and crack initiation detection based on the evolution of surface roughness parameters. Int J Fatigue 107:130–144. https://doi.org/10.1016/j.ijfatigue.2017.10.009

53. Fathi Sola J, Kelton R, Meletis EI, Huang H (2019) Predicting crack initiation site in polycrystalline nickel through surface topography changes. Int J Fatigue 124:70–81. https://doi.org/10.1016/j.ijfatigue.2019.02.027

54. Fathi Sola J, Kelton R, Meletis EI, Huang H (2019) A surface roughness based damage index for predicting future propagation path of microstructure-sensitive crack in pure nickel. Int J Fatigue 122:164–172. https://doi.org/10.1016/j.ijfatigue.2019.01.012

55. Ewing JA, Humfrey JCW (1903) VI. The fracture of metals under repeated alternations of stress. Philos Trans R Soc London Ser A, Contain Pap a Math or Phys Character 200:241–250

56. Carroll JD, Abuzaid W, Lambros J, Sehitoglu H (2013) High resolution digital image correlation measurements of strain accumulation in fatigue crack growth. Int J Fatigue. https://doi.org/10.1016/j.ijfatigue.2012.06.010

57. Sachtleber M, Zhao Z, Raabe D (2002) Experimental investigation of plastic grain interaction. Mater Sci Eng A 336:81–87

58. Abuzaid W, Oral A, Sehitoglu H, et al (2013) Fatigue crack initiation in Hastelloy X - The role of boundaries. Fatigue Fract Eng Mater Struct 36:809–826. https://doi.org/10.1111/ffe.12048

59. Malitckii E, Remes H, Lehto P, et al (2018) Strain accumulation during microstructurally small fatigue crack propagation in bcc Fe-Cr ferritic stainless steel. Acta Mater 144:51–59.

https://doi.org/10.1016/j.actamat.2017.10.038

60.   Mello AW, Nicolas A, Lebensohn RA, Sangid MD (2016) Effect of microstructure on strain localization in a 7050 aluminum alloy: Comparison of experiments and modeling for various textures. Mater Sci Eng A 661:187–197. https://doi.org/10.1016/j.msea.2016.03.012

61.   Zhao Z, Ramesh M, Raabe D, et al (2008) Investigation of three-dimensional aspects of grain-scale plastic surface deformation of an aluminum oligocrystal. Int J Plast. https://doi.org/10.1016/j.ijplas.2008.01.002

62.   Efstathiou C, Sehitoglu H, Lambros J (2010) Multiscale strain measurements of plastically deforming polycrystalline titanium: Role of deformation heterogeneities. Int J Plast. https://doi.org/10.1016/j.ijplas.2009.04.006

63.   Carroll JD, Abuzaid WZ, Lambros J, Sehitoglu H (2013) On the interactions between strain accumulation, microstructure, and fatigue crack behavior. Int J Fract 180:223–241. https://doi.org/10.1007/s10704-013-9813-8

64.   Stinville JC, Echlin MP, Texier D, et al (2016) Sub-Grain Scale Digital Image Correlation by Electron Microscopy for Polycrystalline Materials during Elastic and Plastic Deformation. Exp Mech 56:197–216. https://doi.org/10.1007/s11340-015-0083-4

65.   Zhang Z, Lunt D, Abdolvand H, et al (2018) Quantitative investigation of micro slip and localization in polycrystalline materials under uniaxial tension. Int J Plast 108:88–106. https://doi.org/10.1016/j.ijplas.2018.04.014

66.   Stinville JC, Callahan PG, Charpagne MA, et al (2020) Direct measurements of slip irreversibility in a nickel-based superalloy using high resolution digital image correlation. Acta Mater 186:172–189. https://doi.org/10.1016/j.actamat.2019.12.009

67.   Chen Z, Lenthe W, Stinville JC, et al (2018) High-Resolution Deformation Mapping Across Large Fields of View Using Scanning Electron Microscopy and Digital Image Correlation. Exp Mech 58:1407–1421. https://doi.org/10.1007/s11340-018-0419-y

68.   Tong J, Lin B, Lu YW, et al (2015) Near-tip strain evolution under cyclic loading: In situ experimental observation and numerical modelling. Int J Fatigue 71:45–52. https://doi.org/10.1016/j.ijfatigue.2014.02.013

69.   Jiang R, Pierron F, Octaviani S, Reed PAS (2017) Characterisation of strain localisation processes during fatigue crack initiation and early crack propagation by SEM-DIC in an advanced disc alloy. Mater Sci Eng A 699:128–144. https://doi.org/10.1016/j.msea.2017.05.091

70.   Stinville JC, Lenthe WC, Echlin MP, et al (2017) Microstructural statistics for fatigue crack initiation in polycrystalline nickel-base superalloys. Int J Fract. https://doi.org/10.1007/s10704-017-0241-z

71.   Jiang J, Zhang T, Dunne FPE, Britton T Ben (2016) Deformation compatibility in a single crystalline Ni superalloy. Proc R Soc A Math Phys Eng Sci. https://doi.org/10.1098/rspa.2015.0690

72.   Tschopp MA, Bartha BB, Porter WJ, et al (2009) Microstructure-Dependent local strain behavior in polycrystals through In-Situ scanning electron microscope tensile experiments. Metall Mater Trans A Phys Metall Mater Sci. https://doi.org/10.1007/s11661-009-9938-6

73. Clair A, Foucault M, Calonne O, et al (2011) Strain mapping near a triple junction in strained Ni-based alloy using EBSD and biaxial nanogauges. Acta Mater. https://doi.org/10.1016/j.actamat.2011.01.051

74. Jin H, Lu WY, Korellis J (2008) Micro-scale deformation measurement using the digital image correlation technique and scanning electron microscope imaging. J Strain Anal Eng Des. https://doi.org/10.1243/03093247JSA412

75. Stinville JC, Lenthe WC, Miao J, Pollock TM (2016) A combined grain scale elastic-plastic criterion for identification of fatigue crack initiation sites in a twin containing polycrystalline nickel-base superalloy. Acta Mater. https://doi.org/10.1016/j.actamat.2015.09.050

76. Di Gioacchino F, Quinta da Fonseca J (2013) Plastic Strain Mapping with Sub-micron Resolution Using Digital Image Correlation. Exp Mech. https://doi.org/10.1007/s11340-012-9685-2

77. Guery A, Hild F, Latourte F, Roux S (2016) Slip activities in polycrystals determined by coupling DIC measurements with crystal plasticity calculations. Int J Plast 81:249–266. https://doi.org/10.1016/j.ijplas.2016.01.008

78. Nemcko MJ, Qiao H, Wu P, Wilkinson DS (2016) Effects of void fraction on void growth and linkage in commercially pure magnesium. Acta Mater. https://doi.org/10.1016/j.actamat.2016.04.008

79. Zhao Y, Hu D, Zhang M, et al (2020) In situ measurements for plastic zone ahead of crack tip and continuous strain variation under cyclic loading using digital image correlation method. Metals (Basel) 10:. https://doi.org/10.3390/met10020273

80. Koga N, Sakamaki Y, Kaseya A, et al (2022) Visualization of strain distribution around fatigue crack developed by low cycle fatigue test in high-strength steels using digital image correlation method for replica films. Mater Charact 185:111731. https://doi.org/10.1016/j.matchar.2022.111731

81. Gallo P, Lehto P, Malitckii E, Remes H (2022) Influence of microstructural deformation mechanisms and shear strain localisations on small fatigue crack growth in ferritic stainless steel. Int J Fatigue 163:107024. https://doi.org/10.1016/j.ijfatigue.2022.107024

82. Bhavikatti S, Bhat M, Murthy C (2011) Fatigue Crack Growth Monitoring in Ti-6Al-4V Alloy using Acoustic Emission Technique and Digital Image Correlation. J Non-Destructive Eval 9:

83. Lu YW, Lupton C, Zhu ML, Tong J (2015) In Situ Experimental Study of Near-Tip Strain Evolution of Fatigue Cracks. Exp Mech. https://doi.org/10.1007/s11340-015-0014-4

84. Xue L (2007) Damage accumulation and fracture initiation in uncracked ductile solids subject to triaxial loading. Int J Solids Struct 44:5163–5181. https://doi.org/10.1016/j.ijsolstr.2006.12.026

85. Reseon E (1902) 7 - 9 .]. CC:

86. Forsyth PJE (1953) Exudation of Material from Slip Bands at the Surface of Fatigued Crystals of an Aluminium-Copper Alloy. Nature 171:172–173. https://doi.org/10.1038/171172a0

87. Kuhlmann-Wilsdorf D, Laird C (1980) Dislocation behavior in fatigue V: Breakdown of loop patches and formation of persistent slip bands and of dislocation cells. Mater Sci Eng 46:209–219. https://doi.org/10.1016/0025-5416(80)90176-7

88. Kuhlmann-Wilsdorf D (1989) Theory of plastic deformation: - properties of low energy dislocation

structures. Mater Sci Eng A 113:1–41. https://doi.org/10.1016/0921-5093(89)90290-6

89. Neumann P (1987) Dislocation dynamics in fatigue. Phys Scr 1987:537–543. https://doi.org/10.1088/0031-8949/1987/T19B/035

90. Mughrabi H (2009) Cyclic slip irreversibilities and the evolution of fatigue damage. Metall Mater Trans B Process Metall Mater Process Sci 40:431–453. https://doi.org/10.1007/s11663-009-9240-4

91. Benjamin Britton T, Wilkinson AJ (2012) Stress fields and geometrically necessary dislocation density distributions near the head of a blocked slip band. Acta Mater 60:5773–5782. https://doi.org/10.1016/j.actamat.2012.07.004

92. Bao-Tong MA, Laird C (1989) Overview of fatigue behavior in copper single crystals—I. Surface morphology and stage I crack initiation sites for tests at constant strain amplitude. Acta Metall 37:325–336

93. Sadananda* K, Glinka G (2005) Dislocation processes that affect kinetics of fatigue crack growth. Philos Mag 85:189–203

94. Bao-Tong M, Laird C (1989) Overview of fatigue behavior in copper single crystals—V. Short crack growth behavior and a new approach to summing cumulative damage and predicting fatigue life under variable amplitudes. Acta Metall 37:369–379

95. Bao-Tong M, Laird C (1989) Overview of fatigue behavior in copper single crystals—II. Population, size distribution and growth kinetics of Stage I cracks for tests at constant strain amplitude. Acta Metall 37:337–348

96. Essmann U, Mughrabi H (1979) Annihilation of dislocations during tensile and cyclic deformation and limits of dislocation densities. Philos Mag A 40:731–756

97. Differt K, Esmann U, Mughrabi H (1986) A model of extrusions and intrusions in fatigued metals II. Surface roughening by random irreversible slip. Philos Mag A 54:237–258

98. Essmann U, Gösele U, Mughrabi H (1981) A model of extrusions and intrusions in fatigued metals I. Point-defect production and the growth of extrusions. Philos Mag A 44:405–426

99. Shenoy M, Zhang J, McDowell DL (2007) Estimating fatigue sensitivity to polycrystalline Ni-base superalloy microstructures using a computational approach. Fatigue Fract Eng Mater Struct 30:889–904. https://doi.org/10.1111/j.1460-2695.2007.01159.x

100. Przybyla C, Prasannavenkatesan R, Salajegheh N, McDowell DL (2010) Microstructure-sensitive modeling of high cycle fatigue. Int J Fatigue 32:512–525. https://doi.org/10.1016/j.ijfatigue.2009.03.021

101. Prithivirajan V, Sangid MD (2020) Examining metrics for fatigue life predictions of additively manufactured IN718 via crystal plasticity modeling including the role of simulation volume and microstructural constraints. Mater Sci Eng A 783:139312. https://doi.org/10.1016/j.msea.2020.139312

102. Sangid MD, Maier HJ, Sehitoglu H (2011) A physically based fatigue model for prediction of crack initiation from persistent slip bands in polycrystals. Acta Mater 59:328–341. https://doi.org/10.1016/j.actamat.2010.09.036

103. Man J, Obrtlík K, Polák J (2009) Extrusions and intrusions in fatigued metals. Part 1. State of the art and history. Philos Mag 89:1295–1336. https://doi.org/10.1080/14786430902917616

104. Kastner J, Harrer B, Degischer HP (2011) High resolution cone beam X-ray computed tomography of 3D-microstructures of cast Al-alloys. Mater Charact 62:99–107. https://doi.org/10.1016/j.matchar.2010.11.004

105. Salvo L, Suéry M, Marmottant A, et al (2010) 3D imaging in material science: Application of X-ray tomography. Comptes Rendus Phys 11:641–649. https://doi.org/10.1016/j.crhy.2010.12.003

106. Babout L, Maire E, Fougères R (2004) Damage initiation in model metallic materials: X-ray tomography and modelling. Acta Mater 52:2475–2487. https://doi.org/10.1016/j.actamat.2004.02.001

107. Sedigh Rahimabadi P, Khodaei M, Koswattage KR (2020) Review on applications of synchrotron-based X-ray techniques in materials characterization. X-Ray Spectrom 49:348–373. https://doi.org/10.1002/xrs.3141

108. Lienert U, Li SF, Hefferan CM, et al (2011) High-energy diffraction microscopy at the advanced photon source. Jom 63:70–77. https://doi.org/10.1007/s11837-011-0116-0

109. Poulsen HF, Nielsen SF, Lauridsen EM, et al (2001) Three-dimensional maps of grain boundaries and the stress state of individual grains in polycrystals and powders. J Appl Crystallogr 34:751–756

110. Sachtleber M, Zhao Z, Raabe D (2002) Experimental investigation of plastic grain interaction. Mater Sci Eng A. https://doi.org/10.1016/S0921-5093(01)01974-8

111. Wang Z, Guo W, Li L, et al (2011) Optical virtual imaging at 50 nm lateral resolution with a white-light nanoscope. Nat Commun. https://doi.org/10.1038/ncomms1211

112. Stinville JC, Lenthe WC, Miao J, Pollock TM (2016) A combined grain scale elastic-plastic criterion for identification of fatigue crack initiation sites in a twin containing polycrystalline nickel-base superalloy. Acta Mater 103:461–473. https://doi.org/10.1016/j.actamat.2015.09.050

113. Kahn-Jetter ZL, Chu TC (1990) Three-dimensional displacement measurements using digital image correlation and photogrammic analysis. Exp Mech. https://doi.org/10.1007/BF02322695

114. Winiarski B, Schajer GS, Withers PJ (2012) Surface Decoration for Improving the Accuracy of Displacement Measurements by Digital Image Correlation in SEM. Exp Mech. https://doi.org/10.1007/s11340-011-9568-y

115. Scrivens WA, Luo Y, Sutton MA, et al (2007) Development of patterns for digital image correlation measurements at reduced length scales. Exp Mech. https://doi.org/10.1007/s11340-006-5869-y

116. Kammers AD, Daly S (2013) Self-Assembled Nanoparticle Surface Patterning for Improved Digital Image Correlation in a Scanning Electron Microscope. Exp Mech. https://doi.org/10.1007/s11340-013-9734-5

117. Walley JL, Wheeler R, Uchic MD, Mills MJ (2012) In-Situ Mechanical Testing for Characterizing Strain Localization During Deformation at Elevated Temperatures. Exp Mech. https://doi.org/10.1007/s11340-011-9499-7

118. Schreier H, Orteu J-J, Sutton MA (2009) Image correlation for shape, motion and deformation

measurements: Basic concepts, theory and applications. Springer

119.   Lava P, Cooreman S, Coppieters S, et al (2009) Assessment of measuring errors in DIC using deformation fields generated by plastic FEA. Opt Lasers Eng 47:747–753. https://doi.org/10.1016/j.optlaseng.2009.03.007

120.   Lava P, Cooreman S, Debruyne D (2010) Study of systematic errors in strain fields obtained via DIC using heterogeneous deformation generated by plastic FEA. Opt Lasers Eng 48:457–468. https://doi.org/10.1016/j.optlaseng.2009.08.013

121.   Pan B (2011) Recent Progress in Digital Image Correlation. Exp Mech 51:1223–1235. https://doi.org/10.1007/s11340-010-9418-3

122.   Ho HS, Risbet M, Feaugas X (2015) On the unified view of the contribution of plastic strain to cyclic crack initiation: Impact of the progressive transformation of shear bands to persistent slip bands. Acta Mater 85:155–167. https://doi.org/10.1016/j.actamat.2014.11.020

123.   Cretegny L, Saxena A (2001) AFM characterization of the evolution of surface deformation during fatigue in polycrystalline copper. Acta Mater 49:3755–3765. https://doi.org/10.1016/S1359-6454(01)00271-3

124.   Stoudt MR, Levine LE, Creuziger A, Hubbard JB (2011) The fundamental relationships between grain orientation, deformation-induced surface roughness and strain localization in an aluminum alloy. Mater Sci Eng A 530:107–116. https://doi.org/10.1016/j.msea.2011.09.050

125.   James, D, Dally, and Riley William F (2005) Experimental Stress Analysis. College House Enterprises.

126.   Carter JLW, Uchic MD, Mills MJ (2015) Impact of Speckle Pattern Parameters on DIC Strain Resolution Calculated from In-situ SEM Experiments. In: Conference Proceedings of the Society for Experimental Mechanics Series

127.   Reis M, Diebels S, Jung A (2019) Noise reduction for DIC measurements. Pamm 19:4–5. https://doi.org/10.1002/pamm.201900077

128.   Balusu K, Kelton R, Meletis EI, Huang H (2019) Investigating the relationship between grain orientation and surface height changes in nickel polycrystals under tensile plastic deformation. Mech Mater 134:165–175. https://doi.org/10.1016/j.mechmat.2019.04.011

129.   Castelluccio GM, Musinski WD, McDowell DL (2014) Recent developments in assessing microstructure-sensitive early stage fatigue of polycrystals. Curr Opin Solid State Mater Sci 18:180–187

130.   Chowdhury P, Sehitoglu H (2016) Mechanisms of fatigue crack growth–a critical digest of theoretical developments. Fatigue Fract Eng Mater Struct 39:652–674

131.   Pineau A, McDowell DL, Busso EP, Antolovich SD (2016) Failure of metals II: Fatigue. Acta Mater 107:484–507. https://doi.org/10.1016/j.actamat.2015.05.050

132.   Zimmermann M (2012) Diversity of damage evolution during cyclic loading at very high numbers of cycles. Int Mater Rev 57:73–91

133.   Forsyth PJE (1963) Fatigue damage and crack growth in aluminium alloys. Acta Metall 11:703–715

134. Peralta P, Choi SH, Gee J (2007) Experimental quantification of the plastic blunting process for stage II fatigue crack growth in one-phase metallic materials. Int J Plast. https://doi.org/10.1016/j.ijplas.2007.03.009

135. Laird C (1967) The influence of metallurgical structure on the mechanisms of fatigue crack propagation. ASTM STP 415 131–168

136. Neumann P (1974) The geometry of slip processes at a propagating fatigue crack—II. Acta Metall 22:1167–1178

137. Vehoff H, Neumann P (1979) In situ SEM experiments concerning the mechanism of ductile crack growth. Acta Metall 27:915–920

138. Laird C, Smith GC (1963) Initial stages of damage in high stress fatigue in some pure metals. Philos Mag 8:1945–1963

139. Tanaka K, Hoshide T, Sakai N (1984) Mechanics of fatigue crack propagation by crack-tip plastic blunting. Eng Fract Mech 19:805–825

140. Tomkins B, Biggs WD (1969) Low endurance fatigue in metals and polymers: Part 3 The mechanisms of failure. J Mater Sci 4:544–553

141. Bowles CQ, Broek D (1972) On the formation of fatigue striations. Int J Fract Mech 8:75–85

142. Tvergaard V (2004) On fatigue crack growth in ductile materials by crack–tip blunting. J Mech Phys Solids 52:2149–2166

143. Gerberich WW, Davidson DL, Kaczorowski M (1990) Experimental and theoretical strain distributions for stationary and growing cracks. J Mech Phys Solids 38:87–113

144. Jiang R, Zhang W, Zhang L, et al (2022) Strain localization and crack initiation behavior of a PM Ni-based superalloy: SEM-DIC characterization and crystal plasticity simulation. Fatigue Fract Eng Mater Struct 45:1635–1651. https://doi.org/10.1111/ffe.13685

145. Valiollahi A, Sola JF, Huang H (2023) Combining Effective Plastic Strain and Surface Roughness Change for Identifying Damage Accumulation Sites in a Tensile Sample. Exp Mech. https://doi.org/10.1007/s11340-023-00947-w

146. Yeratapally SR, Glavicic MG, Hardy M, Sangid MD (2016) Microstructure based fatigue life prediction framework for polycrystalline nickel-base superalloys with emphasis on the role played by twin boundaries in crack initiation. Acta Mater 107:152–167

147. Kelton R, Sola JF, Meletis EIEI, et al (2018) Visualization and Quantitative Analysis of Crack-Tip Plastic Zone in Pure Nickel. Jom 70:1175–1181. https://doi.org/10.1007/s11837-018-2865-5

148. Harvey SE, Marsh PG, Gerberich WW (1994) Atomic force microscopy and modeling of fatigue crack initiation in metals. Acta Metall Mater 42:3493–3502

149. Nakai Y (2001) Evaluation of fatigue damage and fatigue crack initiation process by means of atomic-force microscopy. J Soc Mater Sci Japan 50:73–81

150. Polák J, Man J, Obrtlík K (2003) AFM evidence of surface relief formation and models of fatigue crack nucleation. Int J Fatigue 25:1027–1036

151. Risbet M, Feaugas X, Guillemer-Neel C, Clavel M (2003) Use of atomic force microscopy to quantify slip irreversibility in a nickel-base superalloy. Scr Mater 49:533–538

152. Cretegny L, Saxena A (2001) AFM characterization of the evolution of surface deformation during fatigue in polycrystalline copper. Acta Mater 49:3755–3765

153. Risbet M, Feaugas X (2008) Some comments about fatigue crack initiation in relation to cyclic slip irreversibility. Eng Fract Mech 75:3511–3519. https://doi.org/10.1016/j.engfracmech.2007.04.014

154. Wang Y (2012) Study of the surface roughness evolution in fatigued 316L stainless steel

155. Stoudt MR, Hubbard JB (2005) Analysis of deformation-induced surface morphologies in steel sheet. Acta Mater 53:4293–4304

156. Cai M, Stoudt MR, Levine LE, Dickinson JT (2007) A combined study of surface roughness in polycrystalline aluminium during uniaxial deformation using laser-induced photoemission and confocal microscopy. Philos Mag. https://doi.org/10.1080/14786430601003882

157. Hoffmann S, Bleck W (2011) Experimental investigations on topological surface changes during tensile deformation of steels. steel Res Int 82:32–38

158. Abuzaid WZ, Sangid MD, Carroll JD, et al (2012) Slip transfer and plastic strain accumulation across grain boundaries in Hastelloy X. J Mech Phys Solids. https://doi.org/10.1016/j.jmps.2012.02.001

159. Lunt D, Xu X, Busolo T, et al (2018) Quantification of strain localisation in a bimodal two-phase titanium alloy. Scr Mater 145:45–49. https://doi.org/10.1016/j.scriptamat.2017.10.012

160. Abuzaid WZ, Sehitoglu H, Lambros J (2016) Localisation of plastic strain at the microstructurlal level in Hastelloy X subjected to monotonic, fatigue, and creep loading: the role of grain boundaries and slip transmission. Mater High Temp 33:384–400. https://doi.org/10.1080/09603409.2016.1152421

161. Jin H, Lu WY, Haldar S, Bruck HA (2011) Microscale characterization of granular deformation near a crack tip. J Mater Sci. https://doi.org/10.1007/s10853-011-5608-3

162. Stinville JC, Francis T, Polonsky AT, et al (2020) Time-Resolved Digital Image Correlation in the Scanning Electron Microscope for Analysis of Time-Dependent Mechanisms. Exp Mech. https://doi.org/10.1007/s11340-020-00632-2

163. Lim Young bin (2023). Generating Rough surface for Abaqus using MATLAB (https://www.mathworks.com/matlabcentral/fileexchange/111635-generating-rough-surface-for-abaqus-using-matlab), MATLAB Central File Exchange. Retrieved August 7 2023. No Title

Appendix. A

MATLAB code for generating a 3D model with surface roughness

```matlab
function [Nodes,Elements]=Rand_surf(Lx,Ly,Lz,N,sn_x,sn_y,WB_a,WB_b)
% m code by Youngbin LIM
% To inquire any queries, Contact: lyb0684@naver.com
%**********************%
%Description on the input%
%**********************%
% Choose the Length of x and y direction (Lx, Ly)
% Lz is the thickness of deformable solid. It is the distance between
% the bottom surface and the top (averaged) surface
% Input Lz=0 corresponds to 3D surface
% N is the number of division for distance between sampling points
% It will decide the mesh size
% The element length in z-direction is approximately the legnth in x,y
% Choose the number of sampling points for x (sn_x) and y (sn_y) direction
% WB_a and WB_b is parameters for Weibull distribution
% where, Cummulative Distribution Function: F=1-exp[-(x/a)^b]
%********************************************%
% Random sampling of Points on Rough surface %
%********************************************%
% Inverse transformation sampling with Weibull distribution is used %
% Rough surface is assumed to be periodic in x & y direction %
% Side walls (4 faces) are generated in rectangular shape %
% It is for periodcity and successful geometry conversion in Abaqus/CAE %
R_sample=-WB_a*gamma(1+1/WB_b)+WB_a*(-log(1-rand(sn_y,sn_x))).^(1/WB_b);
R_sample=[R_sample(:,1)/2 R_sample]; R_sample=[R_sample(1,:)/2; R_sample];
R_sample=[R_sample R_sample(:,size(R_sample,2))/2]; R_sample=[R_sample;
R_sample(size(R_sample,1),:)/2];
R_sample=[R_sample R_sample(:,1)-R_sample(:,1)]; R_sample=[R_sample; R_sample(1,:)-
R_sample(1,:)];
R_sample=[R_sample(:,1)-R_sample(:,1) R_sample ]; R_sample=[R_sample(1,:)-
R_sample(1,:); R_sample];
maxTh=max(R_sample,[],'all')+Lz;
minTh=min(R_sample,[],'all')+Lz;
%********************************%
%Rigid shell generation for Lz=0 case%
%********************************%
if Lz==0
dx=Lx/(sn_x+3); dy=Ly/(sn_y+3);
x=0:dx:Lx; y=0:dy:Ly;
x_s=0:dx/N:Lx; y_s=0:dy/N:Ly; x_s=x_s'; y_s=y_s';
%********************%
%Spline in y-direction%
%********************%
Ry=[];
for i=1:size(R_sample,2)
    Ry(:,i)=spline(y,R_sample(:,i),y_s);
    Ry=[Ry Ry(:,i)];
end
Ry(:,size(R_sample,2)+1)=[];
```

```matlab
%**********************%
%Spline for whole points%
%**********************%
R=[];
for i=1:size(Ry,1)
    R(i,:)=spline(x,Ry(i,:),x_s);
    R=[R; R(i,:)];
end
R(size(R,2),:)=[];
%****************%
%Rearrange R, x, y%
%****************%
R=R'; z=[]; x=[]; y=[];
for i=1:size(R,2)
    z=[z; R(:,i)];
end
for j=1:size(R,2)
    x=[x;x_s];
end
for j=1:size(R,2)
for i=1:size(x_s)
    y=[y; y_s(j)];
end
end
%*****************************%
%Nodes list for 3D rough surface%
%*****************************%
N_num=1:1:size(z); N_num=N_num';
Nodes=[N_num x y z];
%**************%
%Define Elements%
%**************%
y_elnum=size(y_s,1)-1;x_elnum=size(x_s,1)-1;
El_num=1:1:x_elnum*y_elnum; El_num=El_num';
El_N=zeros(size(El_num,1),4);
%*******************%
%Roughness calculation%
%*******************%
z_avg=mean(Nodes(:,4),'All');
Ra=(1/(Ly*size(y_s,1)))*sum(abs(Nodes(:,4)-z_avg)*(dx/N),'All');
Rq=sqrt((1/(Ly*size(y_s,1)))*sum(((Nodes(:,4)-z_avg).^2)*(dx/N),'All'));
Sa=(1/Lx/Ly)*sum(abs(Nodes(:,4)-z_avg)*(dx/N)*(dy/N),'All');
Sq=sqrt((1/Lx/Ly)*sum(((Nodes(:,4)-z_avg).^2)*(dx/N)*(dy/N),'All'));
fprintf('\nRoughness parameters:')
fprintf('\nRa=%f, Rq(RMS)=%f',Ra,Rq)
fprintf('\nSa=%f, Sq(RMS)=%f',Sa,Sq)
fprintf('\n\nNumber of nodes: %d',size(Nodes,1))
fprintf('\nNumber of elements (R3D4): %d\n\n',size(El_num,1))
if size(El_num,1)>1000000
    fprintf('*************************************************')
    fprintf('\n***WARNING: Number of elements are over 1 million***')
    fprintf('\n*************************************************')
    fprintf('\n\nPress "ENTER" to continue')
    fprintf('\nPress "CTRL+C" to abort\n\n')
    pause;
```

```matlab
end
%***************%
%Mesh generation%
%***************%
for k=1:y_elnum
    for j=1:x_elnum
    El_N(j+x_elnum*(k-1),:)=[j+(x_elnum+1)*(k-1) j+(x_elnum+1)*(k-1)+1
j+(x_elnum+1)*(k-1)+(x_elnum+2) j+(x_elnum+1)*(k-1)+(x_elnum+1)];
    end
end
Elements=[El_num El_N];
%Element sets for surface definition%
elset_S1=[1 x_elnum*y_elnum];
%***************%
%Write input file%
%***************%
fileID=fopen('Rough_Surf_Rigid_Shell.inp','w');
fprintf(fileID, '*Part, Name=Rough_surf');
fprintf(fileID, '\n*Node');
fprintf(fileID,'\n%d, %f, %f, %f',Nodes');
fprintf(fileID, '\n*Element, type=R3D4');
fprintf(fileID, '\n%d, %d, %d, %d, %d',Elements');
fprintf(fileID, '\n*Elset, elset=elset_S1, generate');
fprintf(fileID,'\n%d, %d, 1',elset_S1);
fprintf(fileID, '\n*Surface, type=element, name=S1\nelset_S1, S1');
fprintf(fileID, '\n*End Part');
fclose(fileID);

elseif Lx<0 || Ly<0 || Lz<0
    fprintf('\nThe length value (Lx,Ly,Lz) should be positive number\n\n')
    Nodes=[]; Elements=[];

%**********************************************%
%Check for intersection of top and bottom layer%
%**********************************************%

elseif minTh<0 && Lz>0
    fprintf('\n*******************************************')
    fprintf('\n*********** Mesh generation faild ***********')
    fprintf('\n*******************************************')
    fprintf('\nThe bottom layer intersects with the top layer')
    fprintf('\nPlease increase the thickness\n\n')
    Nodes=[];
    Elements=[];

elseif 0<minTh && maxTh/minTh>10 && Lz>0
    fprintf('\n*******************************************')
    fprintf('\n*********** Mesh quality warning ***********')
    fprintf('\n*******************************************')
    fprintf('\nThe maximum thickness is 10 times greater than the minimum thickness')
    fprintf('\nThere could be mesh quality issue')
    fprintf('\nPlease increase the thickness\n\n')
    Nodes=[];
    Elements=[];
```

```matlab
dx=Lx/(sn_x+3); dy=Ly/(sn_y+3);
x_s=0:dx/N:Lx; y_s=0:dy/N:Ly; x_s=x_s'; y_s=y_s';
avg_mesh_size=(dx/N+dy/N)/2;
Bot_layer_num=floor(Lz/avg_mesh_size);
y_elnum=size(y_s,1)-1;x_elnum=size(x_s,1)-1;
El_num=1:1:Bot_layer_num*x_elnum*y_elnum;
else
dx=Lx/(sn_x+3); dy=Ly/(sn_y+3);
x=0:dx:Lx; y=0:dy:Ly;
x_s=0:dx/N:Lx; y_s=0:dy/N:Ly; x_s=x_s'; y_s=y_s';
%*********************%
%Spline in y-direction%
%*********************%
Ry=[];
for i=1:size(R_sample,2)
    Ry(:,i)=spline(y,R_sample(:,i),y_s);
    Ry=[Ry Ry(:,i)];
end
Ry(:,size(R_sample,2)+1)=[];
%**********************%
%Spline for whole points%
%**********************%
R=[];
for i=1:size(Ry,1)
    R(i,:)=spline(x,Ry(i,:),x_s);
    R=[R; R(i,:)];
end
R(size(R,2),:)=[];
%****************%
%Rearrange R, x, y%
%****************%
R=R'; z=[]; x=[]; y=[];
for i=1:size(R,2)
    z=[z; R(:,i)];
end
for j=1:size(R,2)
    x=[x;x_s];
end
for j=1:size(R,2)
for i=1:size(x_s)
    y=[y; y_s(j)];
end
end
end
%***************************%
%Nodes list for top rough surface%
%***************************%
N_num_top=1:1:size(z); N_num_top=N_num_top';
Nodes_top=[N_num_top x y z];
%*********************%
%Nodes list for bottom layers%
%*********************%
avg_mesh_size=(dx/N+dy/N)/2;
Bot_layer_num=floor(Lz/avg_mesh_size); dz=(Lz+z)/Bot_layer_num;
x_bot=[]; y_bot=[]; z_bot=[];
for i=1:Bot_layer_num
```

```matlab
        z_bot=[z_bot;z-i*dz];
    end
    for i=1:Bot_layer_num
        x_bot=[x_bot;x];
        y_bot=[y_bot;y];
    end
    N_num_bot=(size(z)+1):1:(size(z,1)+size(z_bot,1)); N_num_bot=N_num_bot';
    Nodes_bot=[N_num_bot x_bot y_bot z_bot];
    %*****************%
    %Combine Nodes list%
    %*****************%
    Nodes=[Nodes_top;Nodes_bot];
    %***************%
    %Define Elements%
    %***************%
    y_elnum=size(y_s,1)-1;x_elnum=size(x_s,1)-1;
    El_num=1:1:Bot_layer_num*x_elnum*y_elnum; El_num=El_num';
    El_N=zeros(size(El_num,1),8);
    N_shift=size(y_s,1)*size(x_s,1);% Node number shifting for bottom layer
    %*******************%
    %Roughness calculation%
    %*******************%
    z_avg=mean(Nodes_top(:,4),'All');
    Ra=(1/(Ly*size(y_s,1)))*sum(abs(Nodes_top(:,4)-z_avg)*(dx/N),'All');
    Rq=sqrt((1/(Ly*size(y_s,1)))*sum(((Nodes_top(:,4)-z_avg).^2)*(dx/N),'All'));
    Sa=(1/Lx/Ly)*sum(abs(Nodes_top(:,4)-z_avg)*(dx/N)*(dy/N),'All');
    Sq=sqrt((1/Lx/Ly)*sum(((Nodes_top(:,4)-z_avg).^2)*(dx/N)*(dy/N),'All'));
    fprintf('\nRoughness parameters:')
    fprintf('\nRa=%f, Rq(RMS)=%f',Ra,Rq)
    fprintf('\nSa=%f, Sq(RMS)=%f',Sa,Sq)
    fprintf('\n\nNumber of nodes: %d',size(Nodes,1))
    fprintf('\nNumber of elements (C3D8R): %d\n\n',size(El_num,1))
    if size(El_num,1)>1000000
        fprintf('*************************************************')
        fprintf('\n***WARNING: Number of elements are over 1 million***')
        fprintf('\n*************************************************')
        fprintf('\n\nPress "ENTER" to continue')
        fprintf('\nPress "CTRL+C" to abort\n\n')
        pause;
    end
    %***************%
    %Mesh generationr%
    %***************%
    for i=1:Bot_layer_num
        for k=1:y_elnum
            for j=1:x_elnum
                El_N(j+x_elnum*(k-1)+(i-1)*x_elnum*y_elnum,:)=[j+(x_elnum+1)*(k-1)+i*N_shift
    j+(x_elnum+1)*(k-1)+1+i*N_shift j+(x_elnum+1)*(k-1)+(x_elnum+2)+i*N_shift
    j+(x_elnum+1)*(k-1)+(x_elnum+1)+i*N_shift j+(x_elnum+1)*(k-1)+(i-1)*N_shift
    j+(x_elnum+1)*(k-1)+1+(i-1)*N_shift j+(x_elnum+1)*(k-1)+(x_elnum+2)+(i-1)*N_shift
    j+(x_elnum+1)*(k-1)+(x_elnum+1)+(i-1)*N_shift];
            end
        end
    end
    Elements=[El_num El_N];
```
92

```matlab
%Element sets for surface definition%
elset_S1=[x_elnum*y_elnum*(Bot_layer_num-1)+1 size(El_num,1)];
elset_S2=[1 x_elnum*y_elnum];
elset_S3=zeros(Bot_layer_num,2);
for i=1:Bot_layer_num
    elset_S3(i,:)=[1+(x_elnum*y_elnum)*(i-1) x_elnum+(x_elnum*y_elnum)*(i-1)];
end
elset_S4=zeros(Bot_layer_num,3);
for i=1:Bot_layer_num
    elset_S4(i,:)=[x_elnum+(x_elnum*y_elnum)*(i-1)
x_elnum*y_elnum+(x_elnum*y_elnum)*(i-1) x_elnum];
end
elset_S5=zeros(Bot_layer_num,2);
for i=1:Bot_layer_num
    elset_S5(i,:)=[x_elnum*(y_elnum-1)+1+(x_elnum*y_elnum)*(i-1)
x_elnum*y_elnum+(x_elnum*y_elnum)*(i-1)];
end
elset_S6=zeros(Bot_layer_num,3);
for i=1:Bot_layer_num
    elset_S6(i,:)=[1+(x_elnum*y_elnum)*(i-1) x_elnum*(y_elnum-
1)+1+(x_elnum*y_elnum)*(i-1) x_elnum];
end
%***************%
%Write input file%
%***************%
fileID=fopen('Rough_Surf_3D_Solid.inp','w');
fprintf(fileID, '*Part, Name=Rough_surf');
fprintf(fileID, '\n*Node');
fprintf(fileID,'\n%d, %f, %f, %f',Nodes');
fprintf(fileID, '\n*Element, type=C3D8R');
fprintf(fileID, '\n%d, %d, %d, %d, %d, %d, %d, %d, %d',Elements');
fprintf(fileID, '\n*Elset, elset=elset_S1, generate');
fprintf(fileID,'\n%d, %d, 1',elset_S1);
fprintf(fileID, '\n*Elset, elset=elset_S2, generate');
fprintf(fileID,'\n%d, %d, 1',elset_S2);
fprintf(fileID, '\n*Elset, elset=elset_S3, generate');
fprintf(fileID,'\n%d, %d, 1',elset_S3');
fprintf(fileID, '\n*Elset, elset=elset_S4, generate');
fprintf(fileID,'\n%d, %d, %d',elset_S4');
fprintf(fileID, '\n*Elset, elset=elset_S5, generate');
fprintf(fileID,'\n%d, %d, 1',elset_S5');
fprintf(fileID, '\n*Elset, elset=elset_S6, generate');
fprintf(fileID,'\n%d, %d, %d',elset_S6');
fprintf(fileID, '\n*Surface, type=element, name=S1\nelset_S1, S1');
fprintf(fileID, '\n*Surface, type=element, name=S2\nelset_S2, S2');
fprintf(fileID, '\n*Surface, type=element, name=S3\nelset_S3, S3');
fprintf(fileID, '\n*Surface, type=element, name=S4\nelset_S4, S4');
fprintf(fileID, '\n*Surface, type=element, name=S5\nelset_S5, S5');
fprintf(fileID, '\n*Surface, type=element, name=S6\nelset_S6, S6');
fprintf(fileID, '\n*End Part');
fclose(fileID);
end
```